

ABSTRACT

Title of dissertation: Combinatorial Investigation of Magnetostrictive
Materials

Jason R. Hattrick-Simpers, Doctor of Philosophy, 2007

Dissertation directed by: Professor Ichiro Takeuchi
Department of Materials Science and Engineering

The combinatorial approach to materials science is a research methodology that allows one to study a large number of compositionally varying samples simultaneously. We apply this technique in the search for novel multifunctional materials. Combinatorial libraries with different designs, rapid heat treatments and various characterization techniques are implemented in order to quickly map composition-structure-property relationships in a variety of materials systems.

This thesis will discuss the combinatorial investigation of novel magnetostrictive materials. In particular, binary Fe-Ga and the ternary Fe-Ga-Al Fe-Ga-Pd systems are studied. Magnetron co-sputtered composition-spread samples of the alloys have been fabricated to study composition-dependent trends in magnetostriction. Magnetostriction measurements on all systems studied here have been carried out by optically measuring the deflection of micro-machined cantilever arrays.

Measurements of the magnetostriction on binary Fe-Ga thin-films show similar compositional trends as had been reported in bulk systems. A previously unreported local maximum in the magnetostriction as a function of composition has been found for Ga contents of about 4 at%. It is believed that the origin of this minor maximum is related to a peak in the magnetic moment of Fe atoms and magneto-crystalline anisotropy reported in bulk Fe-Ga alloys at this composition.

We have mapped the Fe-Ga-Pd and Fe-Ga-Al ternary systems. Large regions of the phase diagrams have been mapped out in a single experiment, and the observed magnetostrictive dependence on Ga content matches trends seen in bulk. It was found that the trend in magnetostriction was greatly altered with the inclusion of 1 at% Pd. The addition of up to 10 at % Al to Fe₇₀Ga₃₀ was possible without severe degradation in its magnetostriction.

In order to properly capture and characterize metastable high temperature phases in thin film combinatorial studies, an ultra high vacuum annealing/quenching furnace was developed. X-ray diffraction studies of Fe₇₀Pd₃₀ ferromagnetic shape memory alloy thin-films illustrate the successful capture of the metastable martensitic phase upon quenching, without the phase decomposition that accompanies non-quenching furnace cooling.

A prototype high sensitivity near-field scanning AC magnetometer has been developed utilizing a magnetoelectric laminate device as a magnetic-field sensor. The simple trilayer longitudinal-transverse (L-T) mode sensor, fabricated using Metglas as the magnetostrictive layer and polyvinylidene fluoride as the piezoelectric layer, shows an AC field sensitivity of $467 \pm 3 \mu\text{V}/\text{Oe}$. Scans across a 2 mm diameter current bearing ring demonstrate that the sensor has an AC field sensitivity of 10^{-10} T at room temperature, with a spatial resolution on the order of

millimeters's, which is determined by the size of the sensor device.

Combinatorial Investigation of Magnetostrictive
Materials

by

Jason R. Hattrick-Simpers

Dissertation submitted to the Faculty of the Graduate School of the
University of Maryland, College Park in partial fulfillment
of the requirements for the degree of
Doctor of Philosophy
2007

Advisory Committee:

Professor Ichiro Takeuchi, Chairman/Advisor
Professor Manfred Wuttig
Dr. Leonid Bendersky
Professor James. R. Cullen
Professor Alison Flatau
Professor Richard E. Greene
Professor Samuel E. Lofland

©Copyright by
Jason R. Hattrick-Simpers
2007

DEDICATION

To my wife, my world.

ACKNOWLEDGEMENTS

I firstly thank my advisor, Prof. Ichiro Takeuchi, for teaching, advising, and supporting me during my seven years in his group (2 undergraduate, and 5 graduate). Thank you for providing me with every opportunity you could find to help me develop as a scientist; I only wish I had taken better advantage of each of them. The years I have spent under you have taught me what it means to be a responsible scientist. I appreciate your tireless efforts to save my papers from poor grammar and my presentations from poor organization. If it were not for your intervention I would have never had the opportunity to study here at Maryland, and I am grateful.

I thank my thesis co-advisor Prof. Manfred Wuttig, for sharing his deep knowledge of everything materials with me. Your knowledge of phase transformations and magnetic properties has helped to guide my thesis and also my future work. Thank you for stepping up and helping me to write my thesis (and papers, and talks) while Dr. Takeuchi was on sabbatical.

I also thank Distinguished Prof. Samuel E. Lofland for a myriad of reasons. Sam, every time I have needed your help, your advice, or just your time, you have always come through for me. You were the best possible undergraduate mentor. You never turned your back on any question I asked of you, even when I was no longer your student. Any time I walked into your office with a question I felt was insoluble you answered it then or devoted more of your time to thinking it over carefully. Thank you for allowing me free use of your lab and equipment, although

I was a student at a different school. Without your help I would have never gotten the magnetostriction measurement to work properly.

Dr. Cullen, thank you for your help in modeling the effect of texturing on magnetostriction in thin-film samples and for your encouragement during the lean months before a successful measurement could be made.

Dr. Bendersky, thank you for agreeing to be a part of my committee. I look forward to working with you as your post-doc and hope that I can match your expectations.

I extend my sincerest thank you to the rest of my committee members, Prof. Richard Greene and Prof. Alison Flatau.

I would like to thank all of my group members, past and present, for putting up with me and helping to make the lab a pleasant environment. From the metals group I would like to thank Dr. Olugbenga O. Famodu, Dr. Peng Zhao, Dr. Jun Cui, and Dr. Minghui Yu for their various contributions to my work. In the oxides part of our group I would like to thank Dr. Kao-Shuo Chang, Dr. Maria Aronova, Shigehiro Fujino, and Sung Hwan Lim for the time they spent teaching me about oxide materials and chatting with me about nothing. I would like to thank Dr. Antonio Zambano and Hiroyuki Oguchi from the magnetics group for sharing the MOKE with me. I would particularly like to thank Dr. Makoto Murakami for always jumping out of his seat whenever I asked for help setting up an XRD run. Finally I would like to thank Christian Long for all of the modifications to XRDsuite he has done, and for being a sarcastic reminder of home.

Our group has also had a number of exceptional undergrads work for us over the years and I would like to acknowledge them. To Chris Ryan Ziegler, thank you for your help in the clean room. Kyu Sang Jung, it was a great pleasure working

with you this past year, and I hope we convinced you that a PhD is much better than a MBA.

I have made a few life time friends here at Maryland and I would like to thank them. I thank Jennifer Nguyen for being a great classmate and friend. To my officemates in the Kim building, Von, Linden and Dan “Mr. Fischell” Janiak, thank you for showing me the benefits of every so often having a little bit of fun. Nobuko Koda, thank you for making my first year of classes a better experience. Finally, I want to thank the friend that I imported from New Jersey to help me flood UMCP with angry sarcastic students, Christopher Metting. Thank you for being exactly what a friend should be, I look forward to attending your defense.

I would like to thank all the people working out of the NISP lab, who have helped me over the years. To Dr. Phil Piccoli, thank you for all of your help with calibrating and troubleshooting the microprobe over the past four years. I called you at all hours of the night and you were always happy to help me. I would also like to thank Tiejun Zhang for all of his help with the AFM and ESEM.

I have had the opportunity to do experiments in a number of different places. I would like to thank the following individuals for inviting me into their labs and allowing me to pursue truth. To the folks over at Neocera, in particular Lee Knauss and Antonio Orozco, thank you for helping me to run so many scanning SQUID scans. To Prof. R. B. van Dover at Cornell University, thank you for allowing me to come in and work with your student to perfect the magnetostriction measurement system. Thank you for devoting your time to sitting down and discussing our results with me. I would also like to thank his student, Noble Woo, for being a friend and a colleague. Hasegawa-sensei, thank you for inviting me to spend a few weeks in your lab at the University of Tokyo. Hitoshi Abe, thank you for taking

time away from your lab to guide myself and all the other foreign students around Tokyo.

The final, but perhaps most important, group of people I wish to thank is my family. Mom and Dad, thank you for supporting my decision to spend an additional 5 years in school even after I graduated from college. I don't exactly know how we did it, but somehow we made it through all those bad times together. To Grandma and Grandpa Hatrick, thank you for always being there for my family. Grandma your stoicism in the face of adversity is something I can only hope to copy. You are what holds our family together. Grandpa, we miss you. Thank you so much to Mama Liu and Baba Dai for coming to America and sharing the first 6 months of QiQi's life with us. I am so happy that I had the "chance" to meet you both and to see the joy you brought to Liyang's and QiQi's life.

I want to thank my Uncle Kenny, Aunt Diane, Uncle Gary, and Aunt Linda for all of their support through the years. I would also like to thank Uncle David for all of the interesting conversations on science he engaged me in, and for never getting angry when I would just walk into his house at all hours of the night. To my cousins: Evan "Oh the horror" Saltzberg, Eric "frying-pan-of-death" Saltzberg, Corey "Super Mario" Hatrick, and Adam "That's Mr. Surly to you" Hatrick, I didn't ever feel like an only child because I always had all of you.

To my wife Liyang Dai, I don't know how to thank you for everything that you gave. You gave up the life you had planned, to stay here with me. You gave me a happier life than I deserve. You gave our families a beautiful son, Chance Gary Hatrick, to enjoy for the rest of their lives. You gave everything for our love and our life together, thank you.

TABLE OF CONTENTS

List of Tables	ix
List of Figures	x
1 Introduction	1
1.1 Combinatorial Materials Science	4
1.2 Introduction to Magnetostriction	10
1.2.1 Joule Magnetostriction	12
1.3 Ferromagnetic Shape Memory Alloys	18
1.3.1 Shape Memory Alloys	19
1.3.2 Magnetic-Field-Induced-Strains (MFIS)	22
2 Experimental Methods	24
2.1 Combinatorial Magnetron Co-Sputtering Chamber	25
2.1.1 Spread Design	30
2.1.2 High-Vacuum Annealing Furnace	32
2.2 Rapid Screening Tools	34
2.2.1 Phase Identification	34
2.2.2 Magnetic Characterization	38
2.2.3 Scanning SQUID microscopy	38
2.2.4 MOKE	40
2.3 High-Throughput Magnetostriction Measurement	42
3 Magnetostriction in Fe-Ga Binary Alloy Thin Films	51
3.1 Introduction to Fe-Ga	51
3.2 Binary Fe-Ga Thin-Film Preparation	57
3.3 Microstructure of Fe-Ga Spreads	58
3.4 Magnetostriction in Fe-Ga Composition Spreads	63
3.5 Conclusion	73

4	The Effect of Ternary Additions to Fe-Ga on Magnetostriction	79
4.1	Introduction	79
4.2	Motivation	79
4.3	Sample Preparation and Structural Characterization	80
4.4	Magnetostriction of the Fe-Pd-Ga Ternary System	84
4.5	Fe-Ga-Al	91
4.6	Conclusion	95
5	Characterization of High-Temperature Phases in Fe-Pd-Ga	96
5.1	Introduction	96
5.2	Ferromagnetic Shape Memory Alloy Fe ₇₀ Pd ₃₀	97
5.3	Binary Fe-Pd	97
	5.3.1 Sample Preparation	99
	5.3.2 Structural Properties	100
5.4	Ternary Fe-Pd-Ga Composition-Spreads	101
	5.4.1 Sample Preparation	101
	5.4.2 Magnetic Properties of Fe-Pd-Ga	104
5.5	Conclusion	106
6	Magnetolectric Scanning Probe Microscope	109
6.1	Scanning Magnetic Probe Microscopes	109
6.2	Magnetolectric Laminates	112
	6.2.1 Metglas/PVDF Tri-layer Laminate	114
6.3	Magnetolectric Microscope	118
	6.3.1 Scans of B_x	118
	6.3.2 Scans of B_z	122
6.4	Conclusion	131
7	Conclusions and Future Work	132
7.1	Conclusions	132
7.2	Future Works	134
	7.2.1 Fe-Ga	134
	7.2.2 Exploration of Fe-Co and Ternary Systems	135
	7.2.3 Further Development of Measurement Techniques	135

LIST OF TABLES

- 1.1 List of crystalline metallic alloys and their magnetostriction λ_{100} . . . 11

LIST OF FIGURES

1.1	The correlation between material complexity (reflected by the number of elements) and the material's figure of merit for superconductors (T_c).	6
1.2	A flow diagram of combinatorial materials synthesis in thin-film experiments	7
1.3	Examples of common combinatorial sample designs.	9
1.4	The relationship between magnetization and magnetostriction. Magnetostriction is represented by the dashed line; magnetization by the solid line [1]	12
1.5	Here the relationship between a unit vector in a space formed by three equivalent cubic crystalline axes and θ and ϕ is shown.	14
1.6	A schematic of the crystalline orientation of a single cubic grain in a textured (110) bcc thin-film sample. The (110) direction is indicated by the blue arrow and sticks out of the plane of the sample. Both (100) and (111) type axes along which the magnetostriction exists are contained in the plane of the sample.	16
1.7	Austenitic cubic lattice and martensitic tetragonal lattice in 2D with two variants. The twin planes in the reference cubic lattice and in the deformed tetragonal lattice are shown by the dotted lines.	20
1.8	Microscopic diagram of the shape memory effect. Taken from [1]	21
1.9	Cartoon of the phase transition process and the twin structure in ferromagnetic shape memory alloys. Taken from [1].	23
2.1	A picture of the UHV combinatorial co-sputtering chamber with three magnetron sputtering guns.	25
2.2	A schematic profile of three non-confocal sputtering guns and illustrates the natural composition spread obtained with this system.	27

2.3	The effect of changing the substrate/gun distance on the mapped composition region on the composition-spread wafers. (a) shows a sample done at the normal deposition distance and displays coverage of the entire ternary. (b) shows the effect of moving the sample closer to the guns during deposition without changing the condition. Here, the region of the ternary covered is much lower, although the density of points has also been increased.	29
2.4	Pictures of two types of composition-spread samples used in this thesis. (a) shows a discretized composition-spread made with a physical mask. (b) shows a cantilever library composed of 101 individual MEMs cantilevers.	31
2.5	High-vacuum quenching furnace for capturing high-temperature phases in thin-film composition spread libraries. The furnace is broken into two parts: a “nose,” which contains the samples and is placed directly into the furnace during anneals, and a cooling block, through which cold water is continuously run to protect the cryo-pump and provide handles for quenches.	33
2.6	A schematic representation of the annealing/quenching furnace system.	35
2.7	Scanning X-ray microdiffractometer used for phase identification in composition spread samples. (D8 Discover with GADDS by Bruker-AXS)	36
2.8	A schematic of 2-D X-ray detector illustrating how partial information about χ is obtained.	37
2.9	A picture of the Neocera Magma C20 room temperature scanning SQUID microscope used in this thesis.	39
2.10	The MOKE system used in this thesis.	41
2.11	A schematic representation of the effect of the sign of magnetostriction on the deflection of a cantilever. For negative (positive) magnetostrictions the tip of the cantilever moves up (down).	43
2.12	A schematic of the measurement system for magnetostriction.	44
2.13	A schematic illustrating the effect of torque on the measurement of magnetostriction. The true magnetostriction is represented by the solid red curve. The dashed green and blue curves illustrate the effect of the torque on the magnetostriction curves at high fields for negative and positive cantilever/field angles, respectively.	46
2.14	Experimental data showing the minimization of the torque effect, curves have been offset for clarity.	47

2.15	A schematic representation of the cantilever unimorph and the constants that are required in Lacheisserie’s approximation for obtaining magnetostriction. Here L is the length of the cantilever, E_s and E_f are the Young’s moduli of the substrate and the film, ν_s and ν_f are their Poisson’s ratios, and t_s and t_f are their thicknesses.	49
3.1	Compositional dependence of magnetostriction in Fe-Ga. Taken from [2]. The black circles are furnace-cooled samples and the triangles are from quenched samples.	54
3.2	The binary phase diagram for Fe-Ga from. Taken from [3]	55
3.3	A comparison of the magnetostriction data (plotted in $3/2 \lambda_{100}$) and the binary phase diagram. Notice that the first peak in magnetostriction occurs before the actual onset of the appearance of the DO_3 phase.	56
3.4	Magnetization vs. applied magnetic field curve for a representative 500 nm $Fe_{90}Ga_{10}$ thin-film cantilever. The saturation field is found to be about 1.2 kOe, and the coercivity is less than 200 Oe. The saturation magnetization observed is 1400 emu/cc.	59
3.5	The XRD peak position of bcc-Fe peak ((110) reflection) as a function of Ga composition. The black line is a linear fit to the shift of the peak, and indicates the “solid-solution” region of the spread film. The quality of the fit (R^2) value for the line is 0.9314.	61
3.6	A representative raw 2θ vs. χ image from the 2-dimensional XRD detector showing evidence of the planar texturing of the thin-film samples. Here, the left most peak is the (110) reflection.	62
3.7	Selected area diffraction pattern of the $Fe_{65}Ga_{35}$ thin-film sample. The planar texturing(110) is evidenced by the obtained ring patterns. Courtesy of Leonid Bendersky.	64
3.8	A bright-field plan-view TEM image of an $Fe_{65}Ga_{35}$ thin-film sample taken normal to the film surface. The grain size is 20-30 nm. The contrast is due to different crystalline orientations. Courtesy of Leonid Bendersky.	65
3.9	Bright-field cross-section image of an $Fe_{65}Ga_{35}$ thin-film sample from a composition spread. A columnar structure is observed grown at angle with respect to the substrate. Image courtesy of Leonid Bendersky.	66

3.10	A schematic of how the compositional error across a single cantilever was measured. A point, taken to be the composition primarily responsible for deflection, was taken at the center of the base of the cantilever. Two points at either edge of the base of the cantilever were used to identify the compositional inhomogeneity of the cantilever. Measurements were also taken along the length of the cantilever.	70
3.11	The compositional dependence of $3/2 \lambda_{111}$. It is seen that λ_{111} is small and negative for low Ga contents and then abruptly changes sign at 19 at % Ga. Taken from [4].	71
3.12	The compositional dependence of the ratio of $4 \lambda_{100}/5 \lambda_{111}$. The red line marks where the ratio is 1. In the high Ga content region the contribution to λ_{eff} of λ_{100} is greater than or equal to that of λ_{111} . Data taken from [4].	72
3.13	Compositional dependence of magnetostriction from two rows of a Fe-Ga thin-film cantilever unimorph composition-spread sample. Here, the rows represent the top two rows from the cantilever library. The black squares are from the first row and the red circles are from the second row. Three maxima are noted at 4, 21, and 31 at% Ga. $\lambda_{eff} = \frac{1}{5}\lambda_{100} + \frac{4}{5}\lambda_{111}$	74
3.14	Comparison of the trend in magnetostriction as a function of composition between bulk studies (red triangles) and λ_{eff} measured from the present thin-film study (black squares). The bulk data were taken from [2]. $\lambda_{eff} = \frac{1}{5}\lambda_{100} + \frac{4}{5}\lambda_{111}$	75
3.15	A comparison of the magnetostriction observed in thin-film Fe-Ga samples with the known Fe-Ga binary phase diagram. There is strong correlation between the presence of the peaks in magnetostriction and the onset of new phases. $\lambda_{eff} = \frac{1}{5}\lambda_{100} + \frac{4}{5}\lambda_{111}$	76
4.1	Volumetric plot of the compositional dependence of XRD peaks in the Ni-Mn-Al system. Ternary composition is mapped in the xy plane, and the $2-\theta$ angles. All major diffraction peaks are plotted as dots in the three dimensional space.	83
4.2	A schematic of the volumetric plot of the plane used to fit solid solution is shown in (a), where the region of the planes intersection with the plot is marked in blue. (b) shows the actual data where the ternary phase diagram has been projected to lie in the plane going into the paper and the y axis is the peak position of the α -Fe peak. The color bar is the residual between the plane fit and the measured peak positions and is used to approximate the solid solution region.	85

4.3	The variation of the residual between the measured angle and the approximated angle as a function of composition. The region of dark blue is taken to be the region of solid solution.	86
4.4	Variation of magnetostriction across the Fe-Pd-Ga ternary measured from the Fe-Ga-Pd cantilever library. The approximate area of solid solution region has been marked with the lightly shaded triangle. Each strip of data corresponds to a row in the cantilever spread, with a maximum of 5 rows per spread. The region along the Fe-Ga binary edge is the only region showing appreciable striction and correlates well with what is seen in bulk studies. $\lambda_{eff} = \frac{1}{5}\lambda_{100} + \frac{4}{5}\lambda_{111}$	88
4.5	A comparison of the trend of magnetostriction as a function of Ga content of thin-film combinatorial samples of Fe-Pd-Ga with the trend of λ_{eff} observed in thin-film Fe-Ga. It is seen that the trend in magnetostriction is greatly changed by the addition of small amounts of Pd. $\lambda_{eff} = \frac{1}{5}\lambda_{100} + \frac{4}{5}\lambda_{111}$	89
4.6	A comparison of the trend of magnetostriction as a function of Ga content of thin-film combinatorial samples of Fe-Pd-Ga with binary bulk Fe-Ga data from [2]. $\lambda_{eff} = \frac{1}{5}\lambda_{100} + \frac{4}{5}\lambda_{111}$	90
4.7	The variation of magnetostriction λ_{eff} in the Fe-Ga-Al ternary system measured using the thin-film composition-spread Fe-Ga-Al cantilever library. The area of solid solution has been marked with a colored triangle. Here, there is significant magnetostriction over a large area of compositions spanning from Fe-Ga to Fe-Al. The trend in the data is identical to what is seen in bulk, indicating Al additions do not affect the compositional dependence of magnetostriction in Fe-Ga [2]. A large region near $\text{Fe}_{70}\text{Ga}_{30-x}\text{Al}_x$ for $x \leq 10$ was found to be insensitive to Al additions. $\lambda_{eff} = \frac{1}{5}\lambda_{100} + \frac{4}{5}\lambda_{111}$	92
4.8	The variation of magnetostriction λ_{eff} as a function of the sum of Ga and Al concentrations, shows the same general trend as in pure Fe-Ga. The broadness of the peak is likely due to composition gradients across the cantilever. $\lambda_{eff} = \frac{1}{5}\lambda_{100} + \frac{4}{5}\lambda_{111}$	93
4.9	Schematic representation of the large magnetostriction region in Fe-Ga-Al. The yellow region is the area of large magnetostriction in the system, the blue circles bulk data taken from [5, 6], the green boxes represent the maxima in magnetostriction found in bulk binary Fe-Ga and Fe-Al, and the orange oval indicates the new region with higher Al insensitivity found in this thesis.	94
5.1	Phase diagram of Fe-Pd. From [3]. The red line emphasizes the magnetic region in the high-temperature part of the phase diagram.	98

5.2	A comparison of θ - 2θ XRD scans from the quenched and slow-cooled Fe ₇₀ Pd ₃₀ samples. Here the presence of phase decomposition to α -Fe and FePd is clearly seen in the slow-cooled sample. The quenched samples retains the high-temperature fcc/bcc phase.	100
5.3	The coverage of composition in Fe-Pd-Ga composition spreads as a function of different heat treatments. (a) shows WDS data of an as-deposited sample. (b) and (c) show the effect of annealing at 900°C in vacuum and in 1 atm of He, respectively. By increasing the back-pressure more Ga is trapped.	103
5.4	A magnetic-flux-density mapping of the ternary phase diagram obtained through scanning SQUID microscopy. Here, the magnetic flux density is related to the remnant magnetization of each sample. The shaded bar beneath the graph indicates the magnetic region of the known high-temperature phase diagram of binary Fe-Pd. (Figure 5.1). There is good correlation between the areas that exhibit high magnetization in the ternary and the known magnetic region of binary Fe-Pd. This spread was annealed at 900° for 1 h. in 1 atm of He and then quenched.	105
5.5	A mapping of saturation field plotted on the ternary phase diagram obtained through MOKE measurements. The shaded bar beneath the graph indicates the region of the known high-temperature phase diagram of Fe-Pd that is magnetic. There is good correlation between the areas that exhibit high saturation field in the ternary and the magnetic region of binary Fe-Pd.	106
5.6	A comparison of the high temperature magnetic region from [3] and magnetic region shown by MOKE studies on the quenched Fe-Pd-Ga thin-film samples.	107
6.1	A summary of various scanning-probe magnetometers and their typical spatial resolution and sensitivities. The figure was taken from [7]. The characteristics of the prototype magnetoelectric scanning-probe magnetometer and those of a room temperature scanning SQUID microscope have been added to the figure for comparison [8, 9].	111
6.2	A schematic of an ME laminate device structure.	113
6.3	The ME signal(α_{ME}) versus applied DC field of a device at a frequency of 259 Hz and an AC field amplitude of 10 Oe. The maximum in ME coupling is found at 70 Oe. The ME coefficient is $8.6 \pm .1$ mV/(cmOe) at that bias.	116
6.4	The ME signal versus AC field at a frequency of 259 Hz. The AC sensitivity is taken as the slope of this line and is found to be 467 ± 3 μ V/Oe.	117

6.5	Schematics of the two scanning geometries considered here. (a) illustrates a geometry where the field-annealed direction of the Metglas is oriented parallel to the scanning direction. Here the sensor is only sensitive to B_x . (b) illustrates a geometry where the field-annealed direction is oriented perpendicular to the plan of the current-bearing ring and should only be sensitive to B_z	119
6.6	A B_x line scan of the in-plane field from a 1.8-mm diameter ring. The position of the wires are denoted by the black lines.	121
6.7	A B_z line scan performed over a current bearing ring with an ME sensor. The position of the wires are denoted by the black circles.	122
6.8	A schematic of the approximation used in the finite element calculation for the field distribution. The wire and device are assumed to extend infinitely in the y direction, but have finite dimensions in the x and z directions. The subsequent data will be plotted on the cross-section of the plane and wire illustrated by the plane.	124
6.9	Finite-element simulations of the effect of the permeability of a $125 \mu\text{m} \times 4 \text{ mm}$ device on the field distribution of current bearing wire, for the case of a device with a permeability of (a) 400,000 and (b) 40. The field distributions is only slightly changed by the high permeability material.	126
6.10	Finite-element simulations of the effect of the permeability of a $125 \mu\text{m} \times 100 \mu\text{m}$ device on the field distribution of current bearing wire for the case of a device with a permeability of (a) 400,000 and (b) 40. The field distributions are nearly identical in both cases.	127
6.11	The results of a 2-D scan of the current-bearing ring. The scan direction and orientation of the sensor during the scan are schematically illustrated in the lower right hand part of the graph. The ring is represented by the dotted circle, and the dashed line shows the scan path from the previous line scans. Here a clear elongation of the ring is observed in the direction of the sensor's largest dimension.	129
6.12	A series of scans taken at the following currents: 14.7 mA, 1.47 mA, 0.147 mA. Here the results from 0.147 mA are clearly evident, showing the maximum sensitivity to be 1.5×10^{-10} T. The black circles denote the position of the wires.	130

Chapter 1

Introduction

I have spent the past seven years (2 years as an undergraduate student and 5 years as a graduate student) working on developing various experiments to operate in the context of combinatorial studies. This thesis represents a culmination of this work with a particular emphasis on the work that I have done over the past two years. Because the combinatorial approach is a new methodology, development of rapid characterization techniques often goes hand-in-hand with the synthesis of materials. I have worked on developing combinatorial methods for a number of topics including: multiferroics, shape memory alloys, ferroelectric, and exchange coupled hard magnets. In this thesis, I will discuss the development of new measurement techniques for combinatorial studies, as well as their implementation in exploring magnetic metallic systems.

In the last two years I have focused on the development of high-throughput techniques for measuring magnetostriction in thin-film composition-spread samples. The measurement of thin-film magnetostriction in a rapid screening environment has been a particularly challenging problem in the combinatorial community. The establishment of this technique was greatly facilitated by our collaboration

with Prof. van Dover's group at Cornell University. As a result of the time I spent learning from them and working with them, I was able to independently develop an effective high-throughput magnetostriction measurement system. We consider this to be a major achievement in the field of combinatorial materials science, as well as in the field of magnetostrictive materials, and the measurement technique is detailed in Chapter 2.

In our group, we are always looking for new ways to screen the magnetic properties of combinatorial libraries. When we realized that magnetostrictive materials can be used as magnetic field sensors in multiferroic devices, it was natural to fabricate a magnetic-probe microscope that utilizes these materials. I will relate the results of this work in Chapter 6.

The general outline of my thesis will proceed in the following manner. In Chapter 1, I describe and motivate the combinatorial method to materials science as well as present the materials properties that will be the focus of this thesis. The first section briefly introduces the combinatorial approach to materials science, describe how it is implemented, and provide some examples of systems to which it has been successfully applied. The second section is devoted to a basic introduction to magnetostriction and the properties of magnetostrictive materials. The final section of this chapter is concerned with ferromagnetic shape memory alloys. The shape memory effect, super-elasticity, and magnetic- field-induced strain is discussed.

Chapter 2 will introduce the deposition and characterization techniques to be used throughout this thesis. Our ultra-high-vacuum combinatorial sputtering chamber will first be introduced. This will be followed by a discussion on efforts to develop an ultra-high vacuum quenching chamber to allow the realization of high

temperature phases in combinatorial libraries. Various high-throughput characterization techniques will then be introduced including: scanning X-ray microdiffraction, scanning SQUID microscopy, and a scanning magneto-optical Kerr effect (MOKE) measurement system. Finally our newly developed high-throughput thin-film magnetostriction measurement will be described in detail.

Chapter 3 will concentrate on the synthesis and characterization of Fe-Ge binary spread samples. The microstructure of the films will be investigated through X-ray diffraction as well as transmission electron microscopy. The rest of the chapter will be devoted to the measurement of magnetostriction, using the technique and models described in Chapters 1 and 2, and the comparison of trends and values of magnetostriction to those found in bulk.

The topic of Chapter 4 will be the effects of the addition of the ternary elements Pd and Al to binary Fe-Ga. Alterations of the trend and value of magnetostriction by each element will be discussed. Finally, new region of potential magnetostrictive materials will be introduced in the Fe-Ga-Al system.

Although ferromagnetic shape memory alloys (FSMA) such as Ni_2MnGa and $\text{Fe}_{70}\text{Pd}_{30}$ are not traditional magnetostrictive materials, they do exhibit large magnetic field induced strains which render them functionally analogous. Chapter 5 deals with the capture of high-temperature phases FSMA in the Fe-Pd and Fe-Ga-Pd systems. X-ray diffraction measurements and thermal cycling of cantilever unimorphs are used to confirm the capture of the high-temperature martensitic phase in $\text{Fe}_{70}\text{Pd}_{30}$. Magnetic characterization of the Fe-Ga-Pd system via SQUID microscopy and scanning MOKE will be used to confirm that high-temperature phases were successfully captured.

In Chapter 6, a new potential high-throughput magnetic characterization tech-

nique is demonstrated. The scanning probe magnetometer, which utilizes a multi-ferroic sensor, is shown to have a spatial resolution of millimeters and a high room temperature sensitivity to AC magnetic fields of 5×10^{-10} T.

Chapter 7 will summarize the findings of this thesis, and discuss the continuation of this research.

1.1 Combinatorial Materials Science

Traditionally materials scientists have relied on the single-sample-at-a-time technique to discover new materials. At the crux of this approach is the use of either predictions from theoretical calculations or inferences from literature searches as guiding lights to search for new materials. Once a choice for a new potential material had been made several single composition samples would be synthesized in a one-at-a-time manner, processed and then characterized. This approach is time consuming and can be marred by run-to-run errors that are endemic to synthesis techniques.

In 1995, materials scientists began to embrace the combinatorial approach to materials discovery in greater numbers[10]. This strategy allows one to synthesize hundreds of samples in a single experimental run and then to rapidly characterize them for their figure of merit. This approach had been used by the pharmaceutical industry to expedite the discovery of new drugs, and over the past 13 years has been successfully integrated in numerous inorganic solid-state materials systems. Fields such as dielectric/ferroelectric materials[11, 12, 13, 14] luminescent materials[13, 10], catalysts[15, 16], ferromagnetic materials[17, 18], and shape memory alloys[19] have all benefited from the use of combinatorial material science.

A survey of materials science history shows that most binary compounds have

been explored and their properties are well known. The same can not be said for multi-element compounds such as ternary and quaternary systems, in which there are large knowledge gaps. At the end of the 1980's J.C. Philips estimated that there were about 24,000 known inorganic compounds[20]. 16,000 are binary, and the remaining 8,000 are composed of ternary and other multi-element compounds. The periodic table contains 60 non-radioactive non-gas elements. If one were to pick 3 or 4 of them at random to form compounds, there are 30,000 possible ternaries and 500,000 quaternaries. Clearly there are many possible systems, potentially containing materials with exciting properties, that have not been thoroughly investigated. In addition, there exist many different phases and phase mixtures, accessible through different heat treatments, for materials with the same average composition. Any attempt to systematically investigate such a large phase space utilizing a traditional one-by-one technique is prohibitively time consuming. Combinatorial synthesis can hasten the process of discovering useful materials in this phase space.

The general trend in materials discoveries is that new materials tend to have increasingly complex structures, often consisting of a large number of elements. Another trend is that as the complexity of compounds is increased, the physical properties the compounds possess become more attractive. A clear example of this trend is in the field of superconductors: to date, the highest superconducting transition temperature observed is in $\text{HgBa}_2\text{Ca}_2\text{Cu}_3\text{O}_{8+d}$, which has a complicated layered structure. The trend of increasing transition temperatures in superconductor is schematically represented in Figure 1.1. The figure suggests that the transition temperature increases as the compounds become more complex.

The most efficient way to implement the combinatorial approach to materials

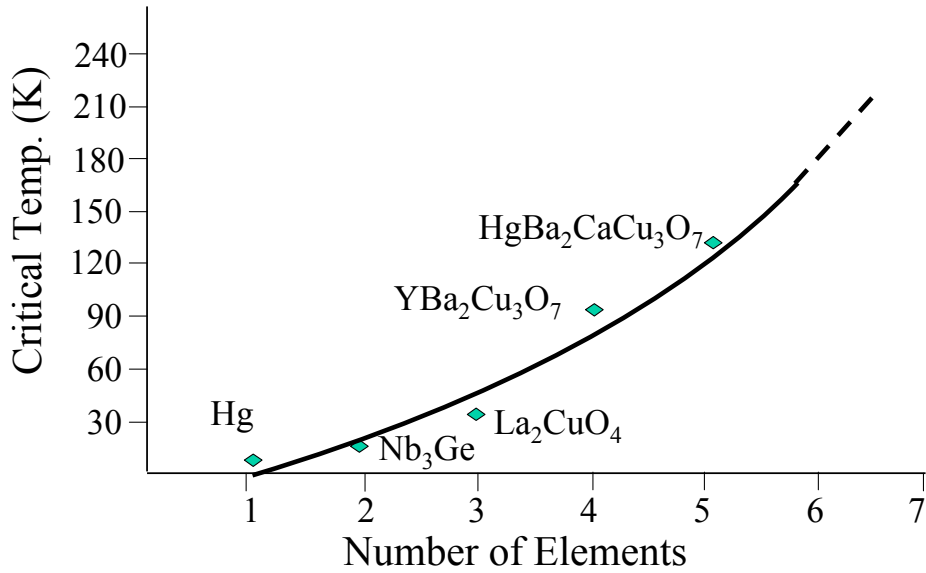


Figure 1.1: The correlation between material complexity (reflected by the number of elements) and the material's figure of merit for superconductors (T_c).

science is through thin-film techniques. Deposition of thin-film samples containing large compositional variation, called libraries, can be performed using a variety of thin-film deposition techniques. In Figure 1.2, the typical flow process for a combinatorial scheme is schematically represented. Here a large number of spatially addressable, compositionally varying samples are deposited in a single set of depositions, through the use of shadow masks. They are then subsequently processed and rapidly screened for regions of interest. The characterization technique employed depends upon the figure of merit for a particular materials system. Once compositions with enhanced physical properties are located, bulk studies are employed to scale up the samples and analyze the region in more detail. Depending on the results of the initial exploration, new libraries are sometimes designed for further studies.

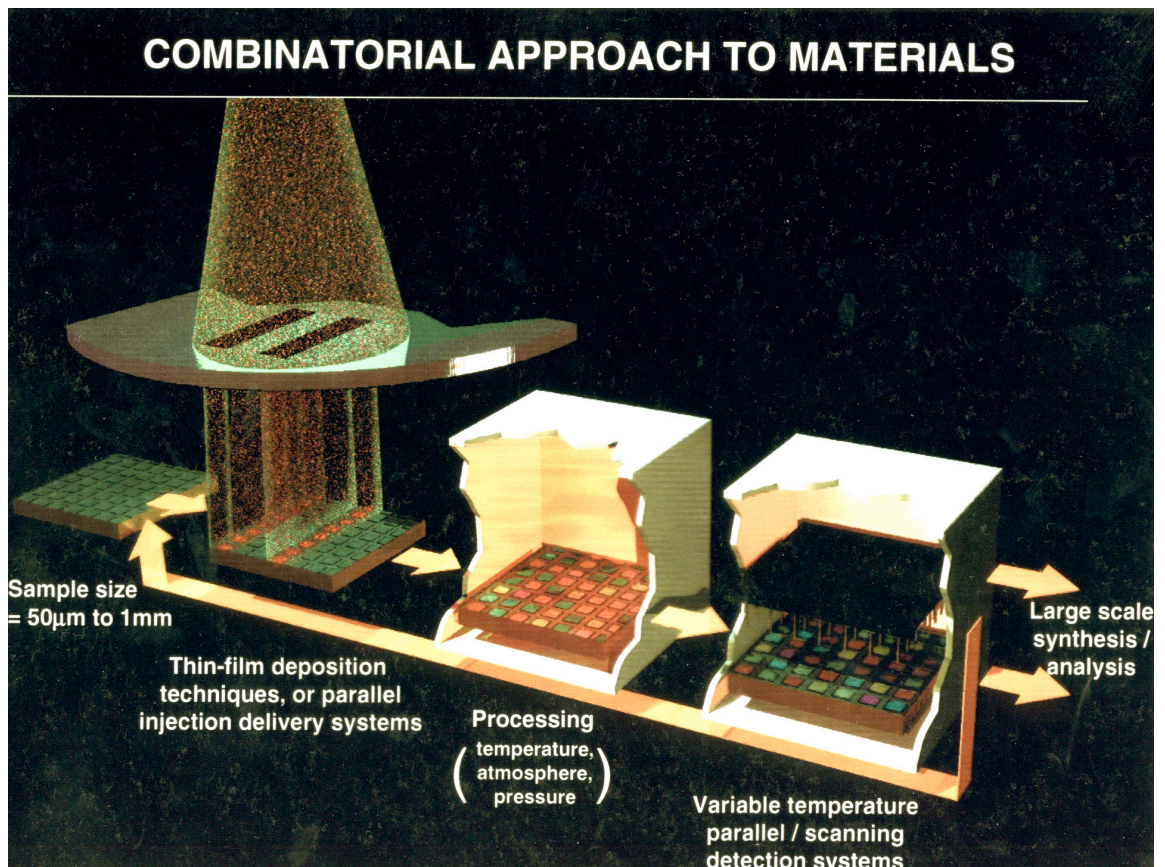


Figure 1.2: A flow diagram of combinatorial materials synthesis in thin-film experiments

In our group we utilize a number of new combinatorial thin-film deposition techniques. These techniques include: pulsed laser deposition with a modular combinatorial flange, laser molecular-beam epitaxy with *in-situ* RHEED to monitor the surface of the film, a 12-source dual-gun electron-beam evaporation system with a modular combinatorial flange, and a multi-target ultra high-vacuum magnetron co-sputtering system.

We primarily use three different library designs. In this thesis the natural composition spread technique, illustrated in Figure 1.3 (a), has been applied in the search for new magnetostrictive materials in Fe-Ga and related systems. Here three different elements (A,B,and C) are co-deposited. An advantage of this approach is that during deposition there is atomic intermixing of the elements. This can preclude the need for post-deposition annealing to acquire compositional homogeneity through the thickness of the film. The second type of library design we employ is the discrete library shown in Figure 1.3 (b). Each site, through shadow masking, is spatially separated from its neighbor and can be individually addressed as C_{xy} , where x and y are the cartesian coordinates of an individual composition. Such a library can consist of hundreds of samples, and these libraries are central to our efforts in investigating the physics of exchange-coupled magnets [21]. The final type of combinatorial sample we employ is the binary composition spread, Figure 1.3 (c). With the help of a continuously moving masking system the composition can be made to vary from pure A on one side to pure B on the other. The samples are deposited in a layer-by-layer wedge configuration which allows the mixing of constituents on the nanometer level. This approach has been use to map binary phase diagrams in systems such as $\text{PbTiO}_3\text{-CoFe}_2\text{O}_4$ and $\text{BiFeO}_3\text{-SmFeO}_3$ [22, 23].

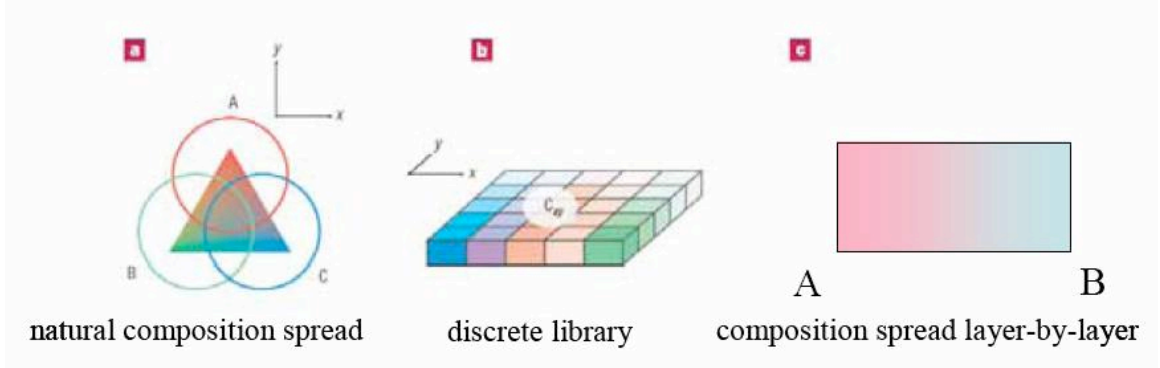


Figure 1.3: Examples of common combinatorial sample designs.

It is often the case that through mapping of the composition phase diagram a deeper understanding of the physics underlying phenomena can be obtained. For instance by mapping out the composition phase diagram of dopants on cuprate superconductors and perovskite manganites a deeper understanding of their physical properties was possible [10, 24]. The use of continuous composition spread techniques has been shown by our group to be a powerful method for exploring previously unknown regions of phase diagrams for materials with enhanced properties in ferromagnetic shape memory alloys[17], thermoelastic shape memory alloys[19], and ferroelectrics materials[25]. In this thesis, efforts to explore the functional phase diagram of Fe-Ga based ternary systems for magnetostrictive materials will be described. The emphasis will be on the trend in and magnitude of magnetostriction.

In combinatorial materials science, it is frequently characterization that provides the main obstruction to successful experimentation. To that end we will discuss our use of parallel detection schemes and non-destructive scanning probes as high-throughput characterization techniques. These include standard combinatorial tools, such as magneto-optical Kerr effect studies and scanning SQUID

microscopy, as well as a newly adapted technique for measuring magnetostriction in a high-throughput manner.

1.2 Introduction to Magnetostriction

Magnetostriction is the measure of how much a material strains when an external magnetic field is applied. The strain induced by a magnetic field is called the magnetostrictive strain, denoted λ and is defined as $\lambda = \frac{\Delta L}{L}$ where L is the unmagnetized length and ΔL is the change in length after magnetization. All inorganic materials exhibit some magnetostriction, and typical values observed vary over 6 orders of magnitude. There are considered to be two fundamental types of magnetostriction, volume and joule magnetostriction, and a third, more specialized type known as magnetic-field-induced strain (MFIS).

In volume magnetostriction, a material undergoes an isotropic expansion(contraction) of the lattice upon the application of magnetic field. Volume magnetostriction is a high-field phenomenon and shows insignificant strains compared to Joule magnetostriction in Fe-Ga. On the contrary, Joule magnetostriction is a volume conserving process in which one axis expands (contracts) while the other two axes contract (expand). Values of strain for joule magnetostriction can vary from practically zero (permalloy) to 0.1% in Terfenol-D. Magnetostrictive materials with large Joule magnetostrictions are currently an object of intense study. The third type of striction, MFIS, is restricted to materials that are ferromagnetic shape memory alloys (FSMAs). FSMAs can have extraordinary strains of 11%, if actuated properly, and will be treated in more detail in a following section. For comparison, the values of magnetostriction for several well known Joule magne-

Alloy	Magnetostrictive Strain λ_{100} [10^{-6}]	Explanation	Reference
Fe	21	Joule magnetostriction	[26]
Ni	-46	Joule magnetostriction	[26]
Fe ₈₄ Al ₁₆	86	Joule magnetostriction	[27]
Fe ₅₀ Co ₅₀	140	Joule magnetostriction	[28]
Fe ₈₃ Ga ₁₇	207	Joule magnetostriction	[27]
Co _{0.8} Fe _{2.2} O ₄	-590	Joule magnetostriction	[29]
Terfenol-D (FeTbDy)	1,600	Joule magnetostriction	[30]
Fe ₃ Pd	10,000	Reversible strain resulting from rearrangement of variants	[31]
Ni ₂ MnGa	100,000	Reversible strain resulting from rearrangement of variants	[32]

Table 1.1: List of crystalline metallic alloys and their magnetostriction λ_{100}

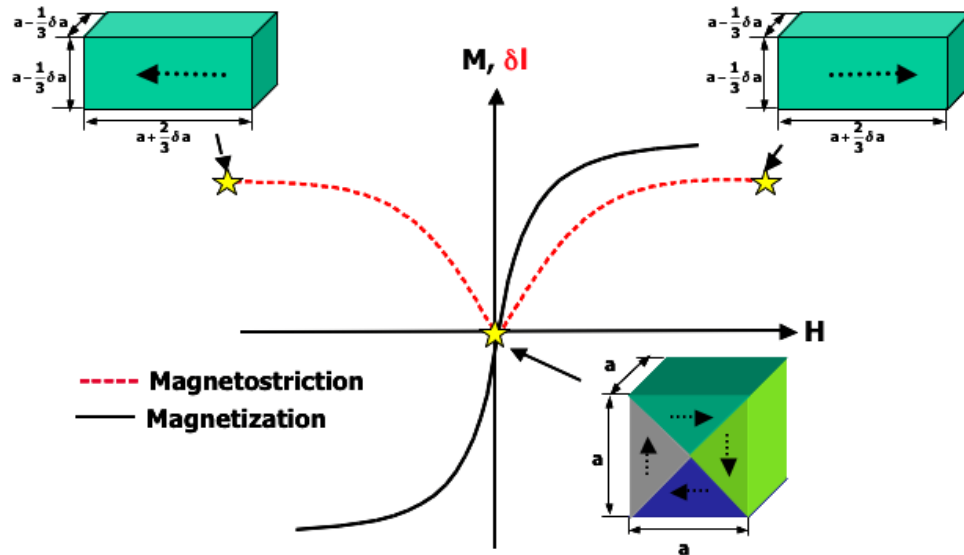


Figure 1.4: The relationship between magnetization and magnetostriction. Magnetostriction is represented by the dashed line; magnetization by the solid line [1]

tostriction materials and FSMA are listed in Table 1.1. Here, the large range of potential strains is clearly evidenced.

1.2.1 Joule Magnetostriction

Joule magnetostriction arises from spin-orbit coupling, which links the direction of the magnetic moment to the crystal lattice. The process of magnetostriction can then be viewed as the transition from a demagnetized multi-domain state to a single-domain state, which is aligned with the applied magnetic field. The relationship between magnetization and magnetostriction is illustrated in Figure 1.4.

Magnetostriction affects the material in two ways, through the δE effect and

the magnetostrictive strain. Here, E is the Young's modulus, which is a measure of the material's stiffness. The δE effect is the effective softening of the Young's modulus of a material as magnetic field is applied. The magnetostrictive strain is the deformation of a material as the magnetic micro-structure is altered due to a magnetic field [29]. It is an even function and is often approximated as being proportional to the square of magnetization at low fields. An inverse magnetostriction effect exists and implies stresses on a sample will affect its magnetic properties, such as the magnetic permeability and the size of the hysteresis loop. This effect has many practical consequences and has been researched extensively[29].

The magnetostrictive strains measured are convoluted functions of the respective magnetostrictive constants of the principle axes[26]. For a cubic symmetry, the measured strain is related to the saturation magnetostrictive constants λ_{100} and λ_{111} which are along the (100) and (111) directions, respectively, by the relationship

$$\lambda_{meas.} = \frac{3}{2}\lambda_{100}(\alpha_1^2\beta_1^2 + \alpha_2^2\beta_2^2 + \alpha_3^2\beta_3^2 - \frac{1}{3}) + 3\lambda_{111}(\alpha_1\alpha_2\beta_1\beta_2 + \alpha_2\alpha_3\beta_2\beta_3 + \alpha_3\alpha_1\beta_3\beta_1). \quad (1.1)$$

For a detailed description of the origin of this formula, please refer to [33]. Here α_i and β_i are the direction cosines of the magnetic field (or magnetization), and the direction cosine of the strain measurement relative to the crystalline axes, respectively. The direction cosines describe the projection of λ_{100} and λ_{111} in the direction of the magnetic field and strain measurement direction. One typically wants to know the magnetostriction in the direction of the magnetization. Therefore $\alpha_i = \beta_i$ and Equation (1.1) becomes

$$\lambda_{meas.} = \frac{3}{2}\lambda_{100}(\alpha_1^4 + \alpha_2^4 + \alpha_3^4 - \frac{1}{3}) + 3\lambda_{111}(\alpha_1^2\alpha_2^2 + \alpha_2^2\alpha_3^2 + \alpha_3^2\alpha_1^2). \quad (1.2)$$

In the case of a polycrystalline sample, there is a completely random orientation

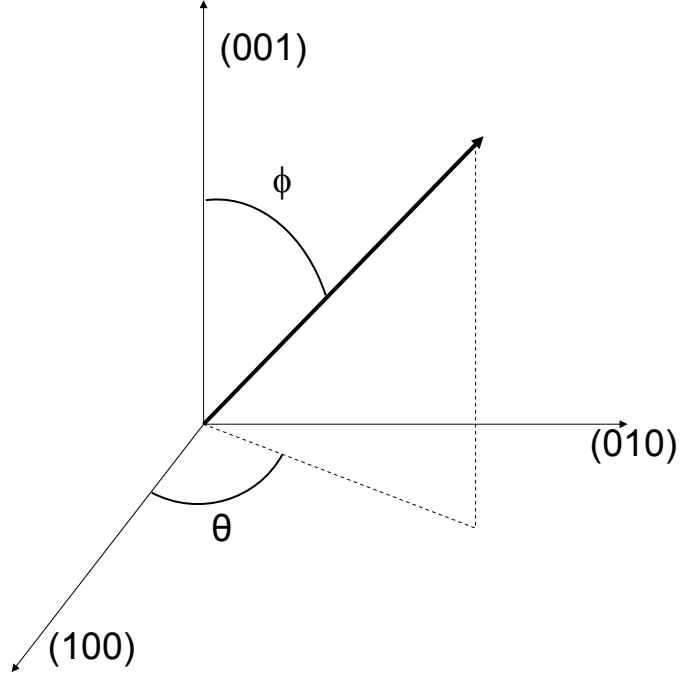


Figure 1.5: Here the relationship between a unit vector in a space formed by three equivalent cubic crystalline axes and θ and ϕ is shown.

of the crystal axis with respect to the measurement direction. To calculate the magnetostriction in this state, it is necessary to assume that the stress is uniform throughout the sample[26]. The calculation of the strain is then reduced to averaging Equation (1.2) over all possible orientations of the crystal. This means the following integral equation must be evaluated

$$\bar{\lambda}_{eff} = \frac{2}{\pi} \int_{\theta=0}^{\frac{\pi}{2}} \int_{\phi=0}^{\frac{\pi}{2}} \lambda_{meas.}(\theta, \phi) \sin \phi d\theta d\phi \quad (1.3)$$

Assuming the system is cubic an arbitrary direction in it can be defined by two angles (θ and ϕ) as shown in Figure 1.5. The relationship between the direction cosines and ϕ and θ are as follows:

$$\alpha_1 = \sin \phi \cos \theta, \alpha_2 = \sin \phi \sin \theta, \alpha_3 = \cos \phi \quad (1.4)$$

With this notation α_1 represents the projection of magnetization along the (100) direction, α_2 the projection of the magnetization along the (010) direction, and α_3 the projection of the magnetization along the (001) direction. The full integral will then take the form

$$\begin{aligned} \lambda_{eff} = & \frac{2}{\pi} \int_{\theta=0}^{\frac{\pi}{2}} \int_{\phi=0}^{\frac{\phi}{2}} \left(\left(\frac{3}{2} \lambda_{100} (\sin \phi \cos \theta)^4 + (\sin \phi \sin \theta)^4 + (\cos \phi)^4 - \frac{1}{3} \right) \right. \\ & + 3 \lambda_{111} \left((\sin \phi \cos \theta \sin \phi \sin \theta)^2 + (\sin \phi \sin \theta \cos \phi)^2 \right. \\ & \left. \left. + (\sin \phi \cos \theta \cos \phi)^2 \right) \right) \sin \phi d\theta d\phi. \end{aligned} \quad (1.5)$$

The resulting relationship for λ_{eff} becomes

$$\lambda_{eff} = \frac{2}{5} \lambda_{100} + \frac{3}{5} \lambda_{111}. \quad (1.6)$$

For the case of thin-film samples deposited on an amorphous substrate, such as Si/SiO₂, the film may not be polycrystalline, but rather be textured out of the plane along the close-packed direction. In body-centered cubic (bcc) materials this is the (110) direction, for face-centered cubic (fcc) materials it is the (111) direction. In this thesis, all the materials will have (110) texturing. It should be noted here that a (110) texturing indicates that the (110) is normal to the plane of the film, and in the plane of the film the lattice is evenly distributed in any in-plane direction. This means that both (100) and (111) type directions (along which magnetostriction is substantial) are contained in the plane of the sample, as seen in Figure 1.6, but randomly oriented. Later in this thesis I will consider such thin-films deposited onto cantilevers, the last statement implies that the magnetic moments will be randomly oriented with respect to the length of the cantilever. The case is similar to that of a polycrystalline sample but now

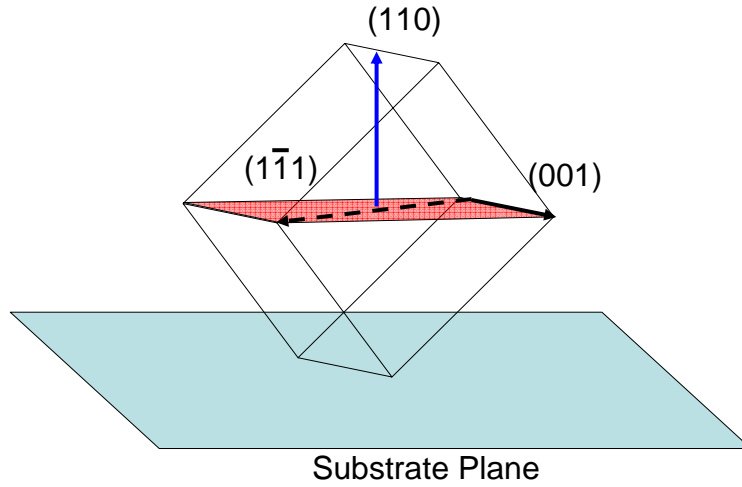


Figure 1.6: A schematic of the crystalline orientation of a single cubic grain in a textured (110) bcc thin-film sample. The (110) direction is indicated by the blue arrow and sticks out of the plane of the sample. Both (100) and (111) type axes along which the magnetostriction exists are contained in the plane of the sample.

the average magnetostriction along the length of the cantilever can be calculated by confining the averaging integral Equation (1.3) to a plane normal to the (110) direction.

Ordinarily, to obtain the saturation magnetostriction, it is necessary to magnetize the samples in two orthogonal orientations to ensure the domains have switched between two orthogonal single domain states. This serves two purposes, the first is to remove any contribution of volume magnetostriction from the measurement, which is not a concern in the systems explored in this thesis, as the Joule magnetostriction is quite large in comparison. The second is to remove the ambiguity that arises from determining the strain of the demagnetized state. This is because at zero magnetization there are an infinite number of possible domain configura-

tions. As an extreme example of this, consider that the zero magnetization state is composed solely of 180° domains running along the length of the sample. If a magnetic field is applied parallel to the domains, then magnetization will take place by domain growth and no net magnetostriction will be observed. The exact opposite is the case if the domains are perpendicular to the applied field. Here the magnetization process takes place through rotation of the magnetic moment and the full saturation magnetostriction would be observed.

In order to calculate the relative contributions of λ_{100} and λ_{111} that account for both the texturing of the sample, as well as the indeterminable domain state at zero magnetization a simple model has been devised. The model calculates the strain state of the material before and after saturation of the magnetic moment. The two values are then subtracted to give a conversion factor that approximates their contributions. Although there are an infinite number of possible domain states, there are a few simple assumptions that can be made for the systems studied here. In the systems considered in this thesis it is most likely that in the demagnetized state there is a random orientation of the domains, due to the low magnetocrystalline anisotropy and the textured nature of the films[34]. This last statement implies that $\alpha_i \neq \beta_i$. Here, again it is the case that the magnetic moment must lie in the plane of the sample. The resulting integration gives an initial strain state of $\lambda_{M=0} = 0$, meaning that the magnetic domains are oriented in such a way that at zero field there is no net strain due to magnetostriction in the material.

To calculate the saturation magnetostriction one must again start with the assumption that the thin-film geometry of the sample's shape anisotropy dictates that the magnetic moments must lie in the plane of the sample. In order to get a plane normal to the (110) direction one must set $\theta = \frac{-\pi}{4}$. For a (110) textured

sample the resulting strain at saturation is given by substituting the value for θ into Equation (1.3) which gives the equation

$$\begin{aligned} \lambda_{eff} = & \int_{\theta=0}^{\frac{\pi}{2}} \left(\left(\frac{3}{2} \lambda_{100} \left(\sin \phi \cos \frac{-\pi}{4} \right)^4 + \left(\sin \phi \sin \frac{-\pi}{4} \right)^4 + (\cos \phi)^4 - \frac{1}{3} \right) \right. \\ & + 3 \lambda_{111} \left(\left(\sin \phi \cos \frac{-\pi}{4} \sin \phi \sin \frac{-\pi}{4} \right)^2 + \left(\sin \phi \sin \frac{-\pi}{4} \cos \phi \right)^2 \right. \\ & \left. \left. + \left(\sin \phi \cos \frac{-\pi}{4} \cos \phi \right)^2 \right) \right) \sin \phi d\phi. \end{aligned} \quad (1.7)$$

After integration, λ_{eff} depends upon λ_{100} and λ_{111} as

$$\lambda_{eff} = \frac{1}{5} \lambda_{100} + \frac{4}{5} \lambda_{111}. \quad (1.8)$$

The results of the integration indicate that the effective joule magnetostriction in textured (110) oriented thin-films can not be deconvoluted into λ_{100} without *a priori* knowledge of λ_{111} . Therefore in this thesis mainly the trend in effective magnetostriction λ_{eff} will be discussed. But in the composition regions that are well known to show λ_{100} much larger than λ_{111} , it is reasonable to assume that we are seeing primarily the effect of λ_{100} . This will be discussed in the context of the measured magnetostriction of λ_{100} in the Fe-Ga system in Chapter 3.

1.3 Ferromagnetic Shape Memory Alloys

Ferromagnetic shape memory alloys are a type of multiferroic materials that exhibit both ferroelasticity and ferromagnetism. They are known to show very large magnetic field induced strains, due to the facile movement of their twin boundaries upon the application of a magnetic field. The following two sections describe ferroelasticity in shape memory alloys and the underlying physics behind the large magnetic-field-induced strains observed.

1.3.1 Shape Memory Alloys

Shape memory alloys (SMAs) exhibit two properties that are technologically interesting. The first property is the shape memory effect, in which a material after it has been deformed can recover its original shape by heating. The second property is superelasticity, here the stress-strain curve exhibits a plateau reminiscent of plastic deformations but is fully reversible. At the crux of these two phenomena is a reversible martensitic transformation.

In martensitic transformations, a high-symmetry parent phase, called austenite, transforms into a lower symmetry phase, called martensite, via a diffusionless shear deformation as the material is cooled below a critical temperature (M_f). The reverse transformation occurs during heating to a slightly higher temperature denoted (A_f). These temperatures are strongly dependent on the composition and the stress state of the material and can be changed several degrees either with a small change in composition or the application of a stress.

Because martensites have lower symmetry than austenites, they can form in several crystallographic orientations with respect to austenites, known as variants. In the absence of applied field, each variant is equally probable to form resulting in a twin related poly-variant configuration. The variants are twin related to one another across a boundary known as the twinning plane. This is schematically represented in Figure 1.7 for the special case of a 2-D cube to rectangle transformation. It is these twins and their mobile boundaries that give rise to the shape memory effect and superelasticity.

A cartoon of the shape memory effect is shown in Figure 1.8. As the sample is cooled below its M_f the two variants grow in such a way as the total macroscopic shape of the material remains unchanged. Upon the application of a load, the

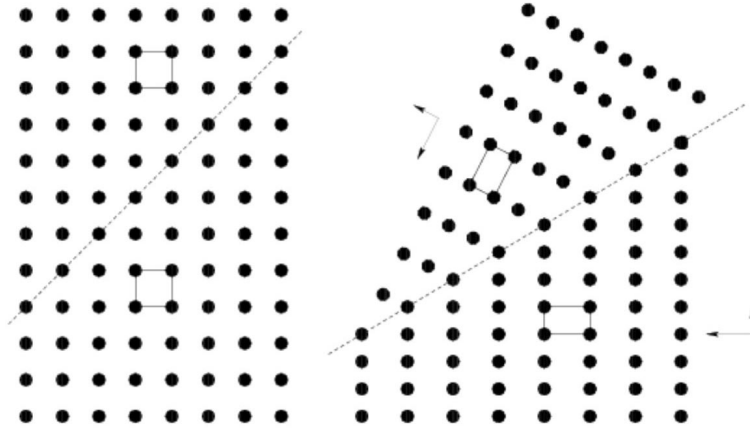


Figure 1.7: Austenitic cubic lattice and martensitic tetragonal lattice in 2D with two variants. The twin planes in the reference cubic lattice and in the deformed tetragonal lattice are shown by the dotted lines.

energetically favored twin grows at the expense of the other until a single variant remains. SMAs can accommodate large strains if they are stressed from one mono-variant state directly to another. This strain is calculated, in the case of a tetragonal martensite, as $\epsilon = 1 - \frac{a}{c}$, where a and c are the long- and short-axis lattice constants, respectively. If the sample is then heated through A_f , then the tetragonal phase will transform back to its cubic form, and the material will “remember” its initial shape.

Superelasticity occurs in SMAs that are still in their austenitic form. Since the critical temperatures are strongly dependent upon stress, if a large enough stress is applied to austenite the transition to martensite occurs. The martensite will then de-twin to accommodate the applied stress. It is this transformation/de-twinning that is responsible for the plastic-deformation-like plateau that is evidenced in the stress-strain curves. Once the stress is removed the specimen transforms back to

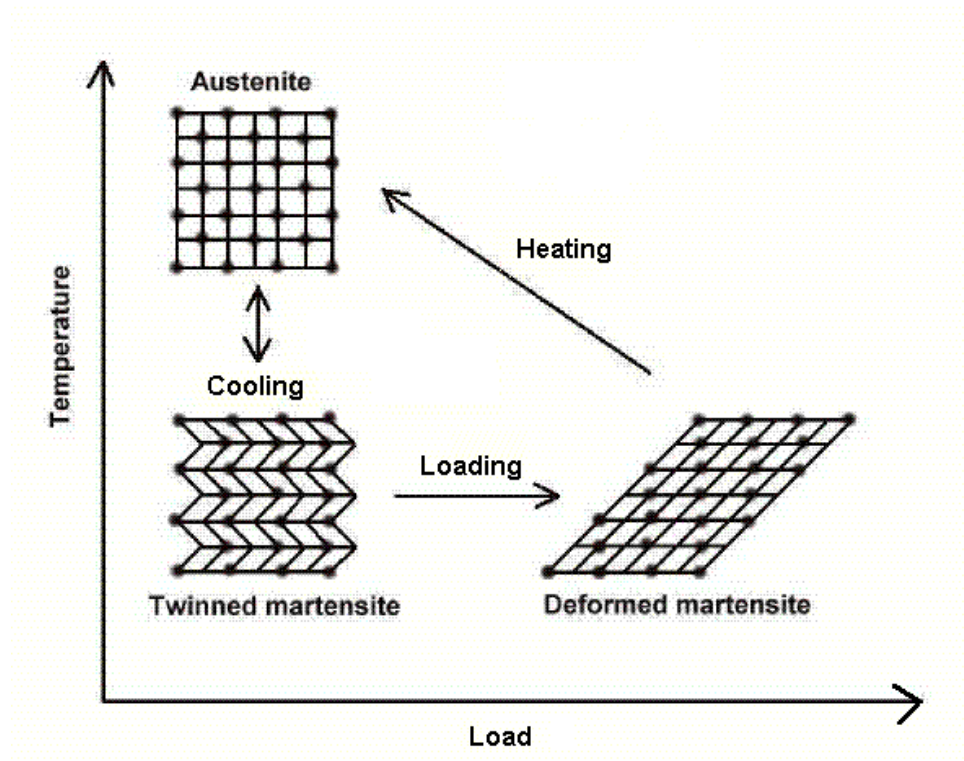


Figure 1.8: Microscopic diagram of the shape memory effect. Taken from [1]

the austenitic phase, completely recovering the strain produced during deformation.

Both of these properties have allowed shape memory alloys to find applications in a variety of fields. Superelasticity is useful in structures that need to deform under stress but then return to their former shape such as, stents and cell phone antennas. The shape memory effect, meanwhile, has found use in diverse fields such as deployment of solar shields and “valves” that self-regulate hot water to keep a constant temperature at the tap. The material primarily used in these applications is Nitinol (NiTi).

1.3.2 Magnetic-Field-Induced-Strains (MFIS)

As previously stated, a ferromagnetic shape memory alloy is simultaneously ferromagnetic and ferroelastic. They exhibit what is known as the “ferromagnetic shape memory effect,” meaning the reversible change in shape is brought about by inducing the austenite/martensite transformation or rearrangement of martensitic variants via an applied magnetic field. Variant rearrangement depends strongly upon several factors; twin-boundary mobility, the magnetic properties of martensite, proper biasing of the initial microstructure, and specimen shape.

Figure 1.9 is a cartoon that illustrates the process of MFIS in a martensite. An austenite in its demagnetized state is composed of several magnetic domains, which on average yield no net magnetization. After transforming to a martensite, the domains are variants, due to the large magnetic anisotropy present in martensites. The large anisotropy pins the magnetic moments to their easy axis and results in the magnetic moments and the variants being coupled. A magnetic field, applied to the multi-domain state minimizes energy through twin/domain boundary motion.

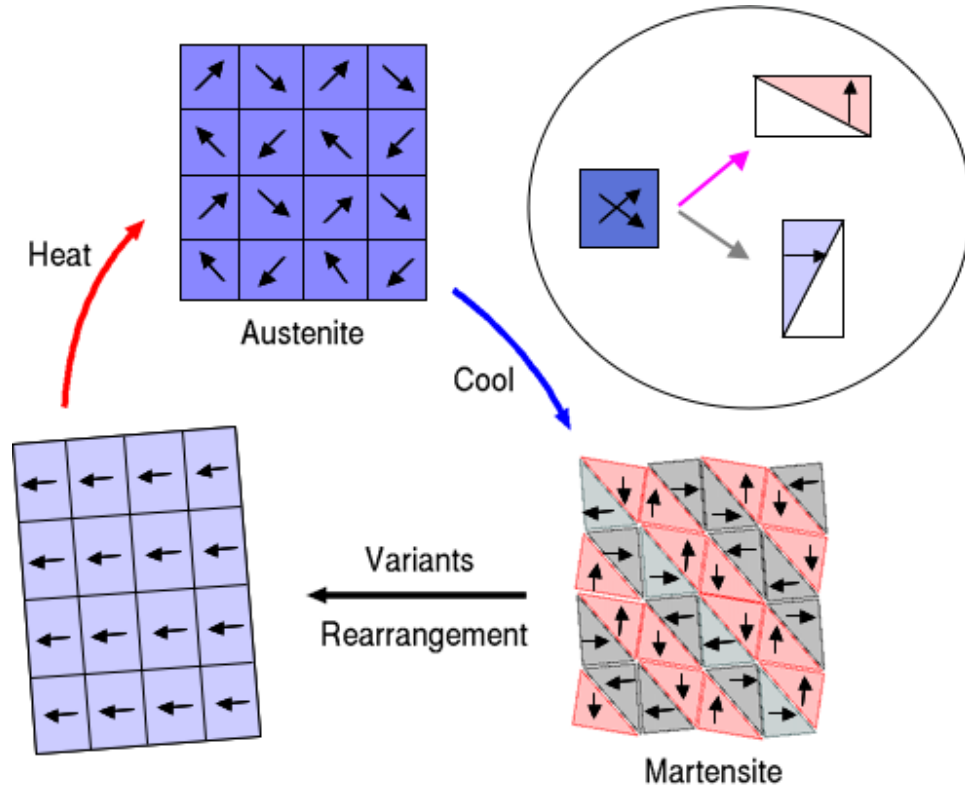


Figure 1.9: Cartoon of the phase transition process and the twin structure in ferromagnetic shape memory alloys. Taken from [1].

This change from a poly-variant state to a single-variant state relies strongly on the energy needed to overcome the magnetocrystalline anisotropy being larger than the energy needed to move the twin boundary.

To date there has been large excitement over the potential of FSMAs in applications due to their large MFIS. However, practical limitations of the materials have hindered their widespread use.

Chapter 2

Experimental Methods

In this chapter I outline the methods used to synthesize, process, and characterize composition-spread samples. To begin, there is a description of the specifications and abilities of the combinatorial sputtering chamber used in this study. Following that is a discussion of the capture of high-temperature phases in thin-film composition spreads with a newly developed high-vacuum annealing furnace. Next the rapid phase identification with X-ray diffraction studies is described. The following section is devoted to the use of scanning-SQUID microscopy and the scanning magneto-optical Kerr effect setup as tools to magnetically characterize the composition spreads. Finally, I discuss our newly developed optical method to quantitatively measure magnetostriction from arrays of thin-film samples deposited on micromachined Si cantilevers.

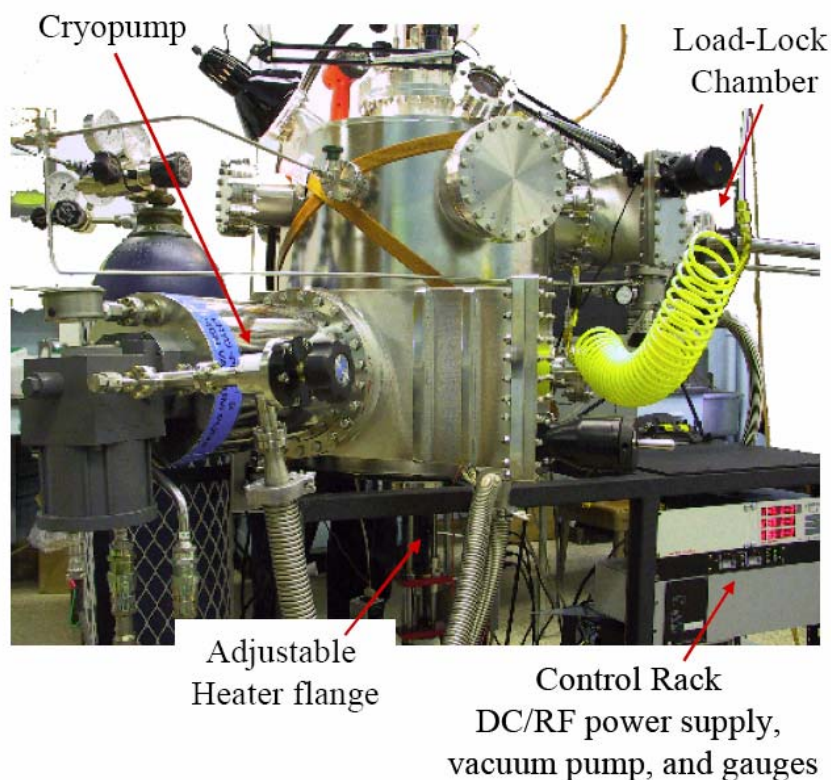


Figure 2.1: A picture of the UHV combinatorial co-sputtering chamber with three magnetron sputtering guns.

2.1 Combinatorial Magnetron Co-Sputtering Chamber

To prepare the composition spreads, an ultra-high-vacuum (UHV) magnetron co-sputtering chamber is used that creates natural ternary composition spreads of metallic alloys. The deposition system is pictured in Figure 2.1. Sputtering is a physical deposition technique in which a target material is bombarded with high-energy ions. The high-energy ions collide with the surface of the target and

impart their energy to the target materials, which are then scattered backwards towards the substrate. The target material hits the substrate with very high energy and cools to room temperature very rapidly. Thus, sputtering is considered a quenching process. This can have the effect of lowering the synthesis temperature of materials. Sputtering was actually one of the first deposition systems used to create composition-spread samples and was used in the 1960s by Hanak *et al.* [35, 36]. Many recent combinatorial studies have embraced sputtering due to its ability to deposit both metals and semiconductors without heating the source materials.

Our combinatorial UHV magnetron co-sputtering chamber can be used to create composition spreads across 3" silicon wafers by natural mixing of elements during deposition. The main chamber has a cryo pump, which creates a base pressure in the range of 10^{-9} Torr. Depositions are performed with ultra high purity (99.9995% purity) Ar at typical pressures of 10^{-3} Torr. The system has 3 magnetron sputtering guns, placed parallel and adjacent in a triangular geometry, as shown in Figure 2.2.

The guns can be used to sputter the target alloys using either DC or RF power supplies, and the powers can range from 5 to 150 Watts. The guns are each housed in a 2" chimney that helps to prevent contamination of the targets as well as to focus the plasma plume. Three 1.5"-diameter targets can be sputtered simultaneously in this system. The sample sits on an adjustable height substrate heater, making it possible to adjust the gun/sample distance during depositions. The normal distance used is between 12.5 to 18 cm. The adjustability of the gun/sample distance allows for precise control of the size of the composition region obtained during a deposition. The heater has a temperature range of 25-900 °C and

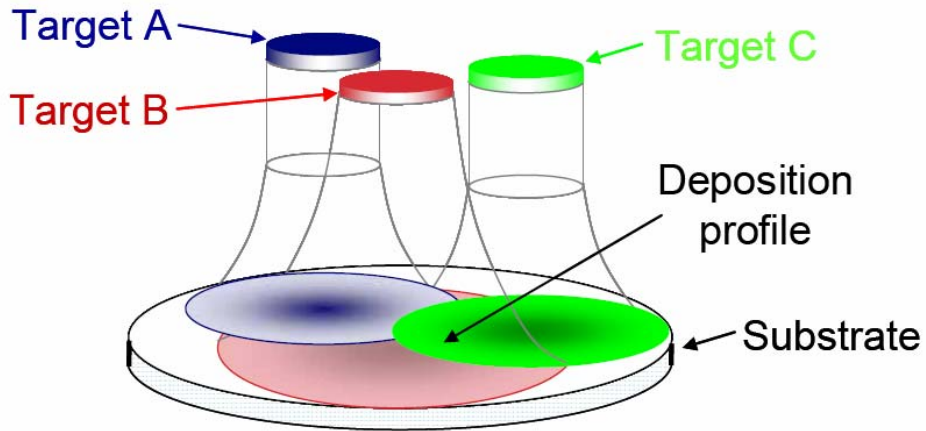


Figure 2.2: A schematic profile of three non-confocal sputtering guns and illustrates the natural composition spread obtained with this system.

is used for *in-situ* anneals. To minimize pump down times between depositions, a load-lock chamber is used to transfer samples in and out of the main chamber.

This chamber is distinctive due to the non-confocal parallel-gun geometry. Ordinarily multi-gun chambers have guns that are focal; ie. focus at the same point, to provide uniform surface coverage. Here, the non-confocal nature of our chamber allows for a natural composition spread to be deposited without the use of any masking systems. This is schematically represented in Figure 2.2 for co-deposition of up to three different targets (A, B, and C). The geometry of the guns allows for a deposition profile that decreases as one moves away from directly underneath the center of each target, and this gives a natural thickness gradient from each sputtering gun. The region where the profiles overlap results in an atomically mixed composition spread.

Depositions in the chamber typically take 1 to 2 hours to deposit a $0.7 \mu\text{m}$ thick film. When deposition conditions are kept nominally constant, run-to-run

compositional reproducibility is excellent, with only small changes (typically ≤ 1 at%) to the overall composition region mapped. These small changes can be attributed to gun power fluctuations, deposition pressure changes, and increased or decreased sputtering efficiency. The last issue is especially problematic in the case of targets of highly magnetic materials, where the flux lines have difficulty penetrating the target initially and then do so more easily as the thickness is decreased. This leads to a deposition rate that varies with the amount of time the target has been sputtered. Compositional variation across each wafer is measured through wave dispersive spectroscopy (WDS), to correct for run-to-run variations. The WDS was used in the thin-film mode with an accelerating voltage of 15 keV and a current of 5×10^{-8} amps. WDS scans of a single composition spread can take from 3 to 12 hrs depending upon the number of points measured.

The combination of the parallel non-confocal gun arrangement with the adjustable gun/substrate distance allows the mapping of complete or partial ternary phase diagrams. Composition gradients across the substrate can be increased (decreased) by decreasing (increasing) the distance. The advantage of decreasing composition gradients is that a region of interest, once identified, can be screened with a higher compositional resolution. The increased density of points in a region of interest is shown for the case of Ni-Mn-Al in Figure 2.3, where two depositions were used to map the entire ternary (a) and a small part of the ternary (b).

The natural mixing inherent in this non-confocal co-sputtering system is a significant advantage of this sputtering system over other combinatorial synthesis schemes. For instance, in the layer-by-layer precursor technique, the sample must either be heated during deposition or post-annealed to promote diffusion of adjacent layers to form films which are homogeneous through the thickness of the

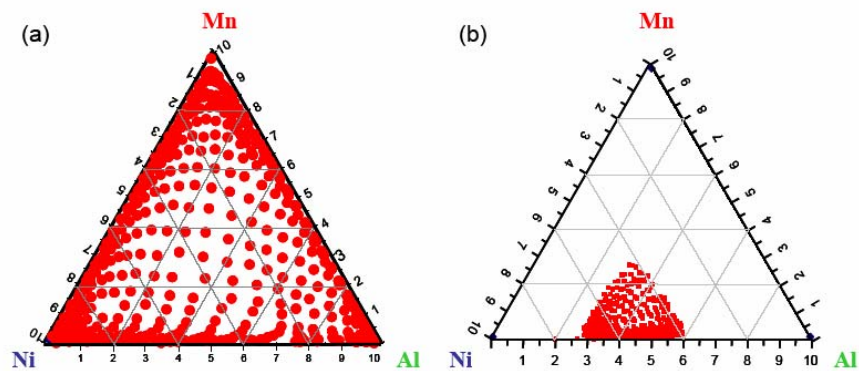


Figure 2.3: The effect of changing the substrate/gun distance on the mapped composition region on the composition-spread wafers. (a) shows a sample done at the normal deposition distance and displays coverage of the entire ternary. (b) shows the effect of moving the sample closer to the guns during deposition without changing the condition. Here, the region of the ternary covered is much lower, although the density of points has also been increased.

film [11]. Since our sputtered samples are atomically mixed as they are deposited, a post-deposition homogenizing anneal is not necessary. However, there are two disadvantages to this technique. The first is that the thickness is frequently not uniform across the wafer so that careful measurements of thickness must be made especially when quantitative magnetic and structural properties are to be obtained. Second, the change in composition does not display a linear variation across the wafer and must therefore be measured for each experiment.

2.1.1 Spread Design

The effective implementation of the combinatorial approach to materials science requires that libraries be deposited in such a way that they can be screened effectively for their properties of interest. In the example of luminescent materials library experiments, where a simple photograph of the chip under UV excitation can be used for initial characterization, sample design is flexible and can work in both a discrete and continuous spread approach. On the other hand, if one is interested in the mechanical properties of a material, for instance martensitic transformations, samples must be designed so that the substrate clamping of the film is minimized. Or, if one is probing the magnetic properties of the composition spread, through measuring field emanating from the in-plane magnetized samples, the film must be discrete so that the magnetic field lines can form closed paths. This allows measurements of local magnetic moment via techniques like scanning SQUID microscopy. In our experiments, we have primarily made use of two spread designs, a discrete composition spread and a unimorph cantilever spread.

The discrete composition spreads, which were used for scanning-SQUID microscopy and magneto-optical Kerr effect studies, were deposited using a physical-

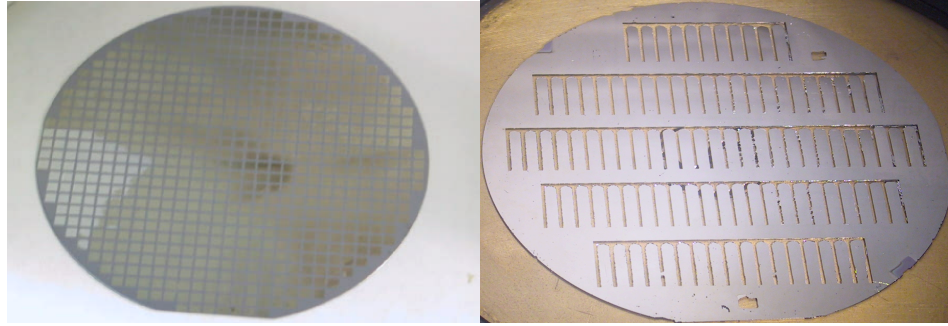


Figure 2.4: Pictures of two types of composition-spread samples used in this thesis. (a) shows a discretized composition-spread made with a physical mask. (b) shows a cantilever library composed of 101 individual MEMS cantilevers.

masking technique. A silicon wafer was micromachined to have 535, 1.75 mm \times 1.75 mm, square holes and was placed firmly on top of a blank silicon wafer prior to deposition to be used as a physical mask. This has the effect of discretizing the composition spread into individual squares when the film is deposited over it (Figure 2.4).

Extrapolation of bulk properties from structural properties measured via thin-film techniques can be difficult to do quantitatively. For instance, in “normal” non-high-throughput thin-film studies, where the thin-film sample is deposited epitaxially on a very thick substrate, a large epitaxial strain can develop at the interface of the substrate and can significantly alter the intrinsic properties of the material. For mechanical properties, the presence of a very thick substrate constrains the mechanical actuation of the material. However, as the thickness of the film approaches that of the substrate, thick films can exhibit bulk-like properties. Previous studies on thermo-elastic shape memory alloys and ferromagnetic shape memory alloys have validated the extrapolation of martensitic properties

taken from thin-film samples using unimorph cantilever libraries to bulk properties [19, 17].

To this end unimorph cantilever spread samples were used to map the magnetostrictive properties of the thin-film samples. The cantilever libraries used here (Figure 2.4) were obtained by depositing directly onto an array of micro-electromechanical (MEMs) cantilevers. The cantilever arrays were formed via a bulk micro-machining technique through wet etching of Si/SiO₂ substrates and contain 101 cantilevers. A detailed description of the process of Si etching can be found in [37]. The individual cantilevers are approximately 8.5 mm long, 2 mm wide, and 60-75 μm thick. The advantage of using cantilevers is that the film is no longer completely constrained by the substrate, and thus variations in mechanical and structural properties can be probed. The movement of bimorph cantilevers due to structural changes is well documented and has been used as the basis for measurements of the thermal actuation of martensite[38], magnetic field actuation of magnetostrictives[39, 40], electrostrictives[41] and hydrogen adsorption/desorption in hydrogen storage materials[42].

2.1.2 High-Vacuum Annealing Furnace

In most combinatorial metallic thin-film experiments requiring heat treatments the sample is mounted directly to a substrate heater, contained within a vacuum deposition chamber. This severely hampers the maximal post-anneal cooling rate. The “quickest” cooling rate in this case can be achieved by simply turning the heater off, but this means it will take the sample 2-3 hours to reach room temperature. During this time any kinetically favored decomposition process can occur and prevent the capture of a desired high temperature phase.

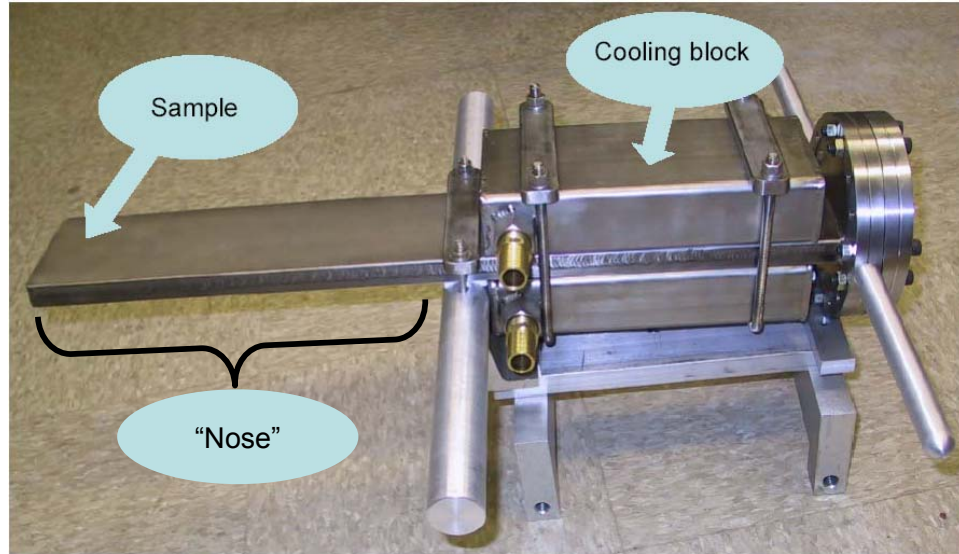


Figure 2.5: High-vacuum quenching furnace for capturing high-temperature phases in thin-film composition spread libraries. The furnace is broken into two parts: a “nose,” which contains the samples and is placed directly into the furnace during anneals, and a cooling block, through which cold water is continuously run to protect the cryo-pump and provide handles for quenches.

In equilibrium experiments, the so-called “furnace cooling” process is often sufficient to net the appropriate equilibrium phase. However, in the study of inter-metallic materials, it is often the non-equilibrium high-temperature phase that is technologically interesting. In fact, studies of the ferromagnetic shape memory alloys Fe_3Pd and Ni-Fe-Al [43, 44], Mn ordering in MnAl [45], and large magnetostriction in $\text{Fe}_{81}\text{Ga}_{19}$ all require heat treatments to be followed by a rapid cooling to room temperature to prevent the formation of detrimental equilibrium phases[46]. This rapid cool is referred to as a “quench.” Bulk studies accomplish this by encapsulation of the sample in a quartz ampoule prior to annealing. After annealing,

the ampoule is shattered in ice water to quench the sample.

To capture high-temperature phases in composition-spread samples on 3" Si wafers, we have developed a high-vacuum quenching chamber, which is shown in Figure 2.5. The quenching chamber is a mobile high-vacuum system that can be placed directly inside a modified high temperature furnace. A schematic of the chamber is shown in Figure 2.6. Samples are placed directly inside the "nose" of the chamber prior to annealing. The chamber is connected to a cryopump and has a base pressure of 10^{-8} Torr. Cooling water is constantly run through the handle grips of the chamber to ensure the handles and the rest of the vacuum equipment remain at room temperature during annealing. The cryopump remains open to the chamber during heat treatments so that even during anneals at 1273 K, the pressure never exceeds 10^{-5} Torr. The gas inlet can be used to vent the chamber post quench or to backfill the chamber with an inert gas (He) to prevent evaporation of high-vapor-pressure materials. After annealing, the chamber is quickly pulled from the furnace and the "nose" end is immersed in ice water, quenching the sample to room temperature in 2-3 seconds. The sample is in constant contact with the bottom side of the chamber during the quench, and therefore, it quenches as quickly as the chamber wall does.

2.2 Rapid Screening Tools

2.2.1 Phase Identification

Structural information was obtained through the use of X-ray diffraction (XRD). XRD gives structural information of the thin-film libraries based on the constructive interference of x-rays with a periodic lattice. The Bragg condition for con-

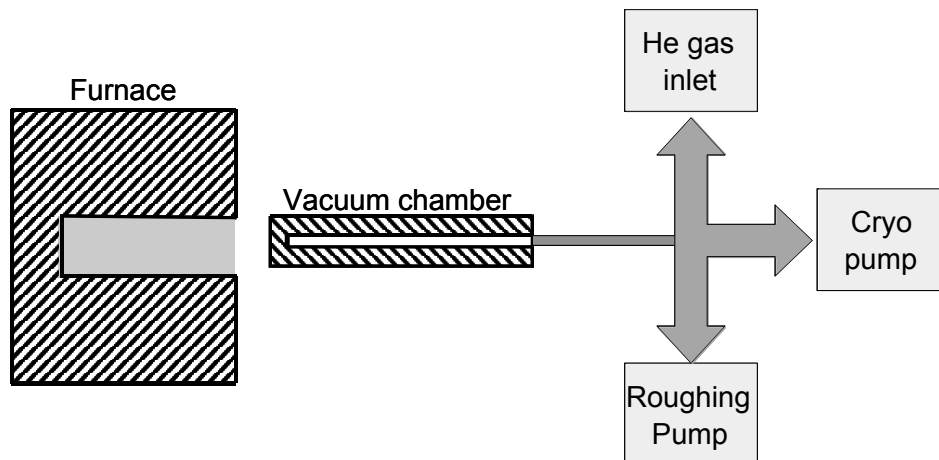


Figure 2.6: A schematic representation of the annealing/quenching furnace system.

structive interference is

$$n\lambda = 2d \sin \theta. \quad (2.1)$$

Here, θ is the angle of incidence of the beam, λ is the beams wavelength, d is the spacing between two planes, and n is an integer. From XRD patterns taken at different sample orientations, it is possible to know the atomic arrangement of atoms. Figure 2.7 shows a scanning X-ray microdiffractometer, D8 Discover with GADDS by Bruker-AXS, equipped with a 2-D detector (diameter 11.5 cm) and an xyz stage that allows for the structural screening of the out-of-plane lattice constant of combinatorial spreads across an entire 3" wafer.

Figure 2.8 illustrates the diffraction geometry of a 2-D area detector. With a point detector only the diffracted beam in the detector plane (xy plane) can be measured. All information along the z axis is lost. The 2-D detector, however, allows for the measurement of photons in a moderate range of z . This means that information about χ is gathered during measurement, and one can gain an

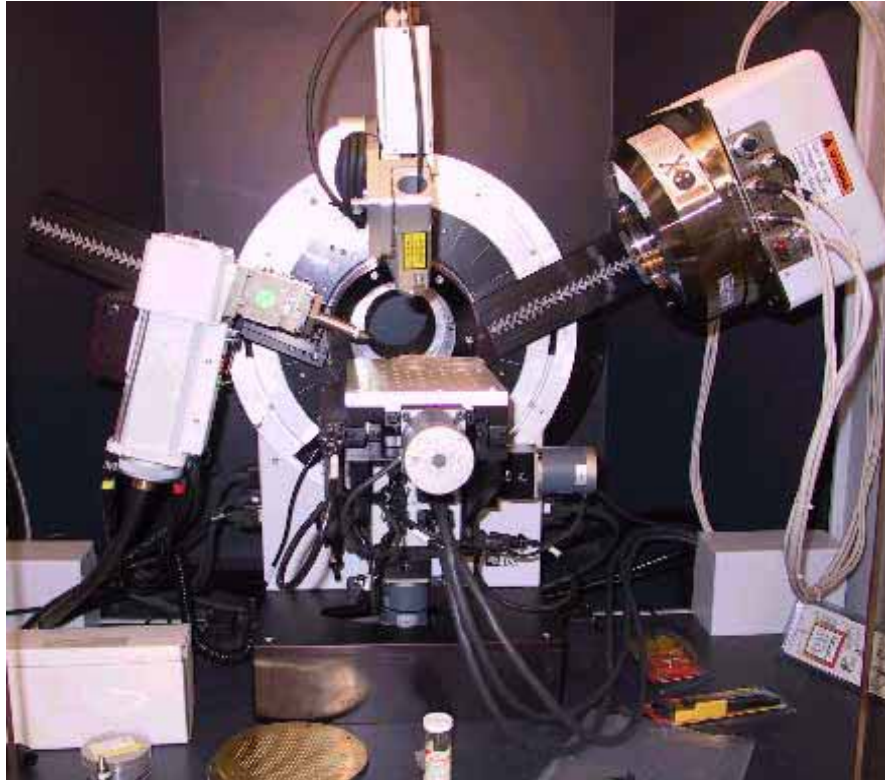


Figure 2.7: Scanning X-ray microdiffractometer used for phase identification in composition spread samples. (D8 Discover with GADDS by Bruker-AXS)

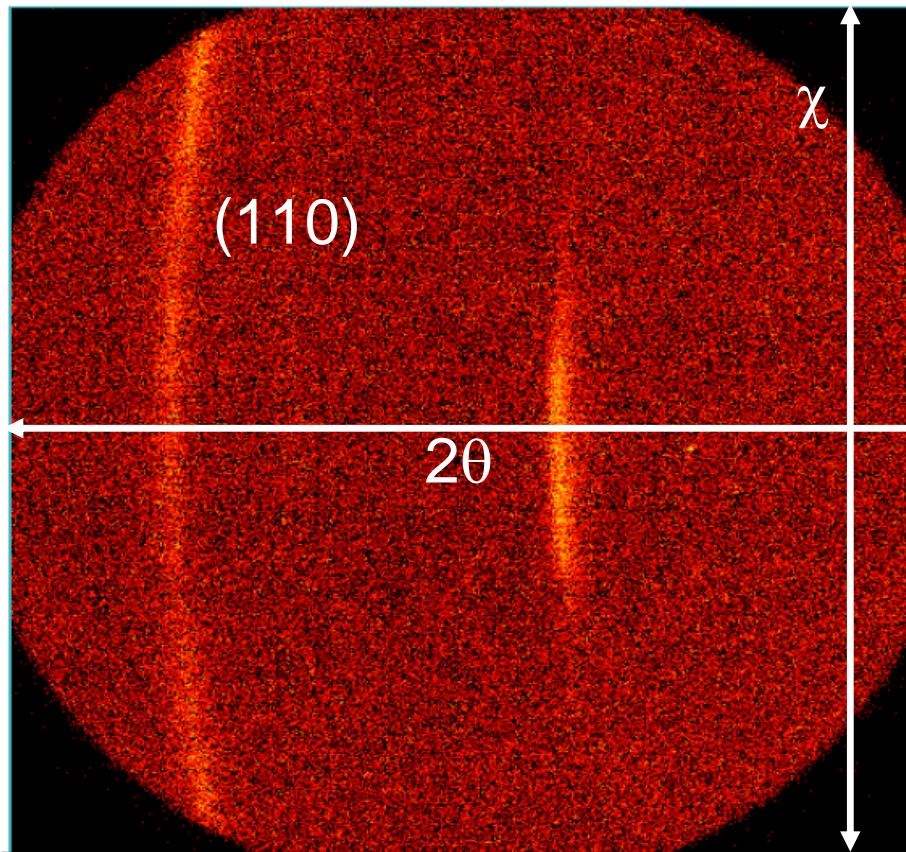


Figure 2.8: A schematic of 2-D X-ray detector illustrating how partial information about χ is obtained.

idea about the degree of texturing in a sample. The range of the 2θ scans is determined by sample height but is typically in the range of $30^\circ \leq \theta \leq 75^\circ$. By integrating with respect to χ it is possible to obtain intensity versus $2-\theta$ curves for easier phase identification. The Bruker tool used has a minimum spot size of $50 \mu\text{m}$. In scanning of our composition spread samples a $300 \mu\text{m}$ beam size was used. Automation programs allow for X-ray spectra to be taken for a large number of points on a wafer in an efficient manner. Subsequent work can be

done to characterize the phases observed in diffraction patterns either manually or through the use of sophisticated data informatics techniques.

2.2.2 Magnetic Characterization

Screening for magnetic properties was carried out through a combination of scanning SQUID microscopy and the scanning magneto-optical Kerr effect (MOKE) measurement setup. The two systems give complementary information and allow for a thorough understanding of the magnetic properties of materials on a combinatorial library. The remnant magnetization of a sample is obtained using scanning SQUID microscopy while MOKE reveals information about the coercivity, the saturation field, and ratio of the remnant magnetization to the saturation magnetization.

2.2.3 Scanning SQUID microscopy

Scanning SQUID microscopes have found application in a variety of topics such as bio-magnetism, defect detection in semiconductor devices, geophysics and scanning microscopy[47]. A scanning SQUID microscope, which are near-field magnetic flux detectors, was used to obtain the remnant magnetization as a function of position (and as a consequence as a function of composition) in our combinatorial libraries [48].

A scanning SQUID microscope (Figure 2.9) is composed of several parts: a SQUID sensor, a micro-positioning stage, a cryogenically cooled dewar, a computer to control the position of the stage and record the SQUID voltage, and an electronic device to keep the SQUID in a flux-locked loop. The SQUID sensor used is a superconducting $\text{YBa}_2\text{Cu}_3\text{O}_{7-x}$ loop interrupted by two resistively and



Figure 2.9: A picture of the Neocera Magma C20 room temperature scanning SQUID microscope used in this thesis.

capacitively shunted Josephson junctions. When the SQUID is current-biased, the voltage across the junction is a periodic function of the applied flux, making a SQUID a flux-to-voltage transducer. In order to circumvent the periodic nature of the voltage, a flux-lock feedback loop is used. The magnetic flux distribution of a combinatorial sample is then obtained via raster scanning the library wafer underneath the SQUID while the response of the SQUID is recorded as a function of position.

In principle, the spatial resolution of a scanning SQUID microscope is only limited by the area of the SQUID loop, usually $1.2 \times 10^{-10} \text{m}^2$, but this requires the

entire system (SQUID sensor, sample, and scanning stage) to be kept at cryogenic temperatures.

In order to measure the magnetic properties of samples at ambient conditions a room-temperature scanning SQUID microscope was used. Here, the cryogenically cooled SQUID sensor is separated from the room temperature sample by a sapphire window (typically $25\mu\text{m}$ thick), effectively limiting the spatial resolution to the SQUID-sample distance (no better than $20\mu\text{m}$). The field sensitivity of this SQUID microscope is $17 \times 10^{-12}\text{T/Hz}^{1/2}$ [8]. Due to the high sensitivity of the scanning SQUID and the large magnetization of our samples, in all of our scans the SQUID-sample distance was maintained at $300\mu\text{m}$ to avoid flux jumps. The machine used in this thesis was a commercially available Neocera Magma C20 SQUID microscope. It is a z-SQUID system, sensitive to the out-of-plane magnetic properties of the samples. Prior to measurement, an electromagnet was used to magnetize the samples in-plane. The magnetic-field distribution so obtained can be used to quantitatively calculate the remnant magnetization of any sample through the use of an inversion algorithm[49]. This technique allows the rapid and accurate mapping of the magnetic properties of composition-spreads.

2.2.4 MOKE

A high-throughput MOKE system was employed to measure the magnetic hysteresis loops of composition-spread samples. The principle behind MOKE is as follows: when polarized light is incident upon a magnetic material, the polarization of the reflected light will rotate with respect to the incident beam. The rotation is caused by the interaction of the light with the sample's internal magnetic field. Either the Kerr rotation (longitudinal or polar geometry) or the Kerr intensity (transverse

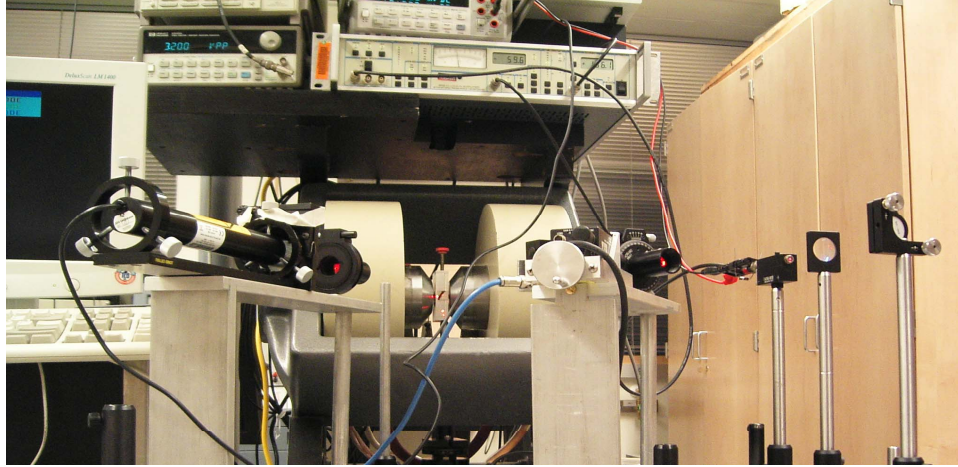


Figure 2.10: The MOKE system used in this thesis.

geometry) may be measured. In this thesis, all discussion will focus on the change in Kerr rotation as a function of applied magnetic field.

It is possible to calculate the magnetization of a sample directly from the Kerr intensity. This is very difficult, however, in the context of a combinatorial study, as this change depends on several materials constants whose compositional dependence is unknown. A more practical way to transform Kerr hysteresis loops into magnetization hysteresis loops is to first measure the remnant magnetization of the sample using a scanning SQUID microscope. Then, since the Kerr rotation is proportional to the magnetization modulo some field independent material constants, the conversion factor for Kerr intensity to magnetization can be obtained by comparing the remnant Kerr intensity to the remnant magnetization.

The MOKE system used in this study, shown in Figure 2.10, was set up in a longitudinal geometry, with the incident beam and the applied field in the plane of the sample. A 635-nm power-stabilized diode laser (20 mW), attenuated down to 2 mW/mm² to avoid local heating, is used as the light source. A condensing

lens is used to focus the spot down to a diameter of less than 1 mm, allowing individual measurements of squares in the gridded libraries (Figure 2.4 (a)). A photoelastic modulator operating at 50 kHz and lock-in detection are used to measure the changes in polarization, yielding a sensitivity of about 5 μ radians. The penetration depth of the light is estimated to be about 150 nm, much less than the typical film thickness. The magnetic field is applied by an electromagnet with a bipolar field range of 2 Tesla. An *xyz* stage, located at the bottom of the sample stage, is used to scan the spread samples. An automated program was designed to scan through the data and evaluate the saturation field (H_s) and coercive field (H_c) for each curve.

2.3 High-Throughput Magnetostriction Measurement

To monitor the deflection, due to magnetostriction, of the cantilever unimorph composition-spreads, a laser positioning system was employed that monitors the movement of a laser reflected from the cantilever as a function of applied magnetic field for each cantilever. The principle behind this measurement technique relies on the elastic coupling of the film and the substrate. When a magnetic field is applied to the unimorph, the magnetostrictive material strains, this is transferred as a stress to the side of the substrate with the film. The resulting strain in the substrate is antisymmetric through the thickness of the substrate and causes the tip of the cantilever to deflect. If the magnetic field causes the crystal to shrink in the direction of the magnetization, the magnetostrictive constant (λ) is considered to be negative and the unimorph will in the positive z direction. For the case

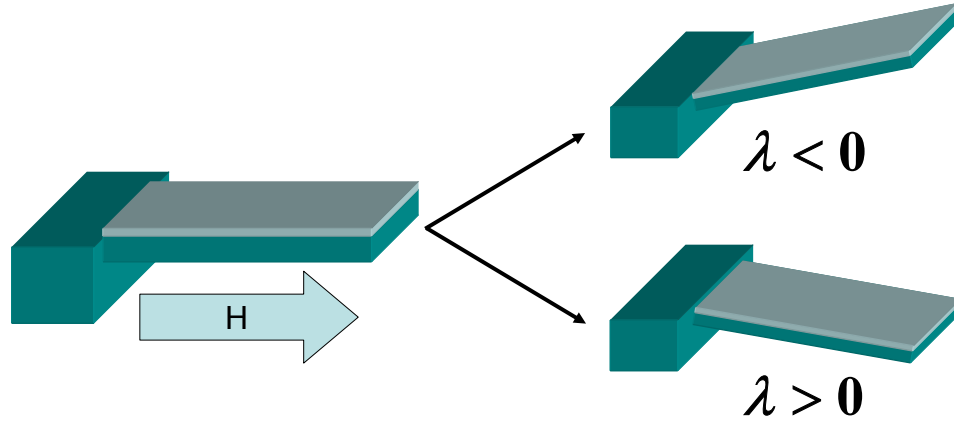


Figure 2.11: A schematic representation of the effect of the sign of magnetostriction on the deflection of a cantilever. For negative (positive) magnetostrictions the tip of the cantilever moves up (down).

of an expansion in the direction of magnetization, the magnetostrictive constant is considered to be positive and the unimorph will in the negative z direction. The dependence of the deflection of a unimorph on the sign of magnetostriction is shown in Figure 2.11. The magnitude and direction of the deflection can then be used to calculate the magnetostriction.

A schematic representation of the measurement system is presented in Figure 2.12. During measurements, the sample is placed on an xyz stage placed between the pole faces of an electromagnet. The electromagnet used has a field range of ± 2 T. The cantilevers are oriented so that during measurements the magnetic field was applied along their long axis. A 635 nm power-stabilized diode laser (20 mW) is used as the light source. A condensing lens is used to focus the spot size down to a diameter of less than 1 mm, allowing individual measurements of each cantilever. The reflected light is collected with a position sensitive detector

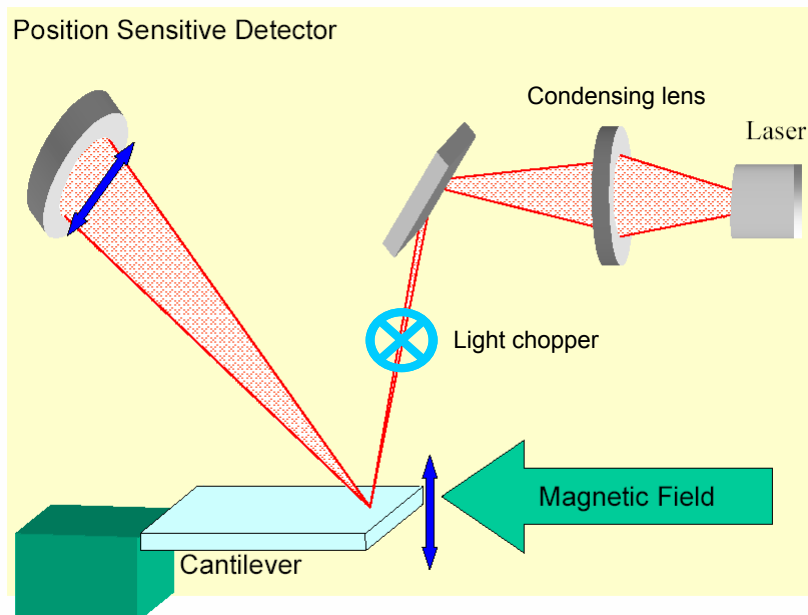


Figure 2.12: A schematic of the measurement system for magnetostriction.

(PSD). A light chopper operating at 500 Hz is used and allows for lock-in detection of the PSD output. This allowed for sensitivities down to surface strains of 6 ppm. An entire unimorph composition-spread sample containing 101 individual cantilevers can be measured in less than a day.

In measuring the magnetostriction of the cantilever unimorphs there are two possible sources of deflection: magnetic torque or magnetostriction. The torque effect is caused by mutual misalignment of the magnetic field and the magnetization of a cantilever. This can cause the unimorph to deflect although even when there is little or no magnetostriction present. The effect can be distinguished from true magnetostriction by the increase in the magnitude of deflection observed with increased cantilever/field angles. The torque effect does not saturate at high fields,

as the torque is proportional to the product of magnetization and magnetic field, and changes sign when the cantilever/field angle changes sign, as illustrated in Figure 2.13. Due to the linear relationship between torque and the magnetic field, the torque effect is primarily a high field effect. Therefore, at low fields the deflection observed is primarily due to magnetostriction. For small cantilever/field angles, the torque effect can be considered negligible compared to the deflection arising from magnetostriction.

To this end the electromagnet was placed on a rotation table and to the measurement of each cantilever by changing the field/cantilever angle until the torque was minimized. The process of torque minimization is shown in Figure 2.14 for a single cantilever. In order to determine if a significant torque effect is present during a single measurement on a cantilever a line is drawn through the “wings” of magnetostriction curve in such a way as to average out the fluctuating background noise. If the slope of the line is suitably small the torque effect is considered to be negligible, and the magnetostrictive deflection can be extracted. The saturation field for magnetostriction is defined as the field at which the “wing” of the curve become straight and level. Usually the saturation field for magnetostriction is achieved at the saturation magnetic field, this will be discussed in Chapter 3.

The raw position sensitive detector’s (PSD) output is converted to deflection via the relationship $D = \frac{C*\delta\theta*L}{A}*V$, where $\delta\theta$ is the change in the angle between the cantilever and the laser, D is the displacement of the cantilever, L is the position along the cantilever at which the measurement is being made, A is the distance between the PSD and the cantilever, V is the voltage output from the PSD, and C is a calibration constant. A value for calibration constant C (the change in

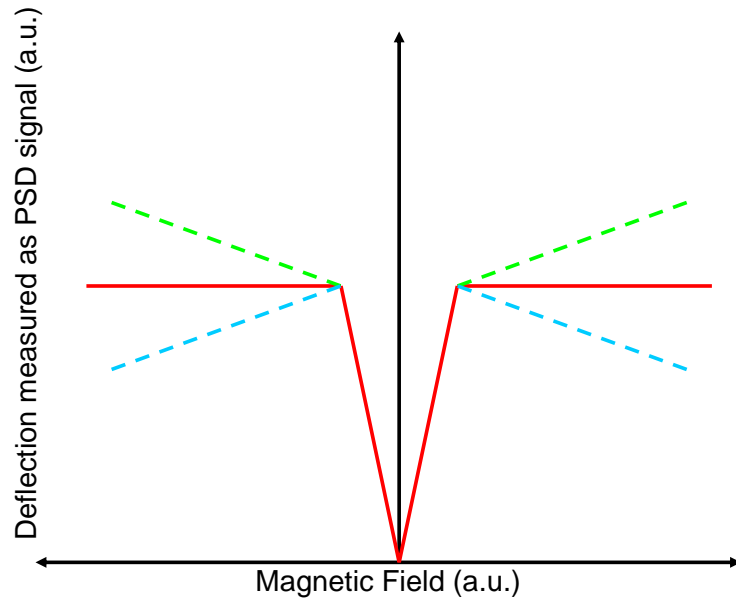


Figure 2.13: A schematic illustrating the effect of torque on the measurement of magnetostriction. The true magnetostriction is represented by the solid red curve. The dashed green and blue curves illustrate the effect of the torque on the magnetostriction curves at high fields for negative and positive cantilever/field angles, respectively.

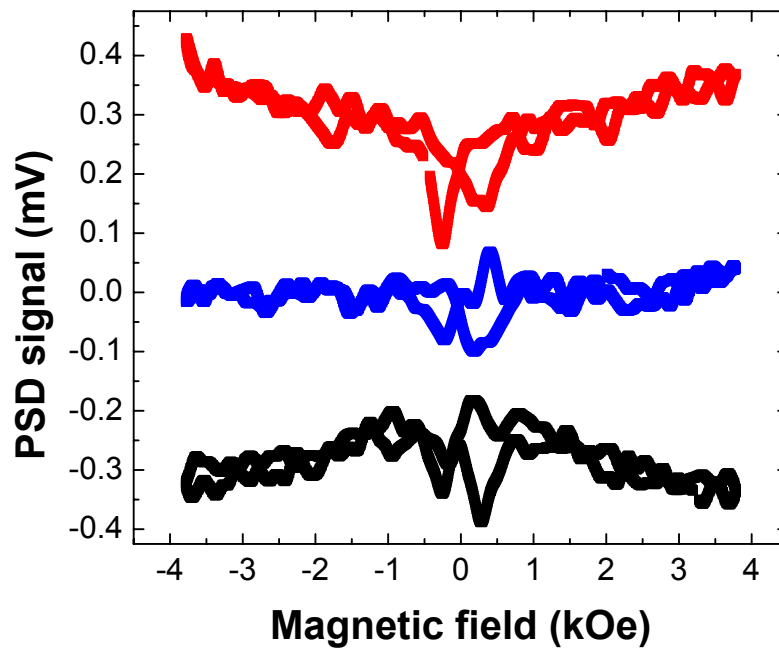


Figure 2.14: Experimental data showing the minimization of the torque effect, curves have been offset for clarity.

voltage/displacement on the PSD) is taken for each cantilever.

The proper conversion of cantilever deflection to magnetostriction is somewhat controversial. There are, in fact, two generally accepted competing theories on how to do this. The first theory was put forward by Klokholm *et al.* who proposed a method in 1976 that states when $L \geq 4w$, where L is the length of the cantilever and w its width, deflections in the plane of the cantilever perpendicular to the cantilever length are negligible[50, 51]. The resulting conversion relies on the Poisson's ratio (ν_s) of the substrate by the factor $(1 - \nu_s)$, as seen in the following formula for the effective magnetostrictive constant λ_{eff} .

$$\lambda_{meas} = \frac{2 * (D_{\parallel} - D_{\perp}) * E_s * (1 + \nu_f) * t_s^2}{9 * E_f * L^2 * (1 - \nu_s) * t_f} \quad (2.2)$$

Here, D_{\parallel} is displacement, due to magnetostriction, of the cantilever with the magnetic field parallel to its long axis, and D_{\perp} is the cantilever deflection with the field applied perpendicular to the long axis, here the two fields are applied in the plane of the cantilever. The two displacements are opposite in sign, because a crystal expands (contracts) in the direction of the magnetization and contracts (expands) in the orthogonal directions, and the difference of these two displacements is the total displacement of the cantilever. L is the position along the length of the cantilever at which the measurement of deflection was made, E_s is substrate's Young's modulus, t_f and t_s are the thicknesses of the film and the substrate, and ν_f is the Poisson's ratio of the film. These constants are shown in Figure 2.15.

In 1996, because of the failure of Klokholm's formula to provide accurate values of magnetostriction in standard thin-film samples, du Tremolet de Lacheisserie presented an alternative derivation that took into account the perpendicular deflection [39, 52]. The formula derived by Lacheisserie was quite similar to that

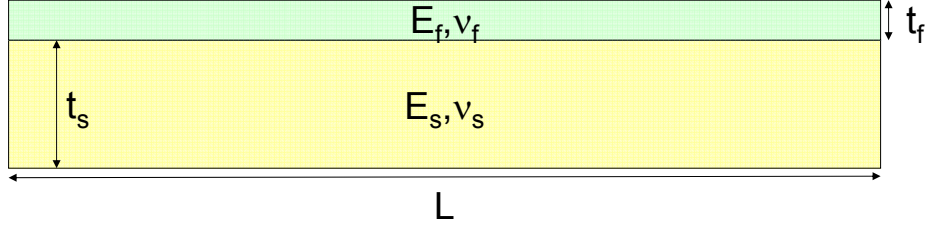


Figure 2.15: A schematic representation of the cantilever unimorph and the constants that are required in Lacheisserie’s approximation for obtaining magnetostriction. Here L is the length of the cantilever, E_s and E_f are the Young’s moduli of the substrate and the film, ν_s and ν_f are their Poisson’s ratios, and t_s and t_f are their thicknesses.

of Klokholm, except that Lacheisserie’s has a factor of $(1 + \nu_s)$. In the latter approach, the raw deflection of the cantilever is converted to a magnetoelastic coupling constant (b) through the the following formula

$$b = \frac{(D_{\parallel} - D_{\perp}) * E_s * t_s^2}{3 * L^2 * (1 + \nu_s) * t_f} \quad (2.3)$$

To calculate the “effective” magnetostriction from the magnetoelastic coupling constant one must then take the ratio of the magnetelastic coupling (b) with the shear coefficient of the film (c). In the case of a single crystal the shear coefficient

is twice the Lam constant, and the formula for magnetostriction becomes

$$\lambda_{meas} = \frac{2 * (D_{\parallel} - D_{\perp}) * E_s * (1 + \nu_f) * t_s^2}{9 * E_f * L^2 * (1 + \nu_s) * t_f} \quad (2.4)$$

Since most work done recently on cantilever unimorphs has verified the formulation of Lacheisserie as being more accurate for calculating magnetostriction, this method will also be used in this thesis. All the measurements in this thesis were performed on Si/SiO₂ substrates. Therefore the Young's modulus and Poisson's ratio of the substrate are known. Unfortunately, the ratio of $\frac{E_f}{1+\nu_f}$ is difficult to measure reliably for thin-film samples. In prior work on thin-film cantilevers, an effective modulus of 50 GPa was used for Fe-based thin-films materials[53, 54]. To allow for easy comparison between the results presented here and previous work the same value will be used. Finally, in the current measurement system, the magnetic field can only be applied along the long axis of the cantilever, so it will be assumed that D_{\perp} is zero with the understanding that the values of magnetostriction obtained will be lower bounds of the true value. Thus, a lower bound to the value for λ_{meas} can be calculated from the measured displacement.

Chapter 3

Magnetostriction in Fe-Ga Binary Alloy Thin Films

In this chapter, results for combinatorial studies on the magnetostriction of binary Fe-Ga are presented. The chapter begins with an introduction of previous work on Fe-Ga in bulk and thin film experiments. The second section presents the results of microstructural studies on the thin-film composition-spread samples utilizing XRD and TEM. The final section is devoted to measurements of magnetostriction on thin-film unimorph cantilever libraries of binary Fe-Ga.

3.1 Introduction to Fe-Ga

Although the room-temperature magnetostriction of pure Fe is an unremarkable 50 ppm, Fe alloys have been shown to demonstrate appreciably larger magnetostriction. For instance, it has been known since the work of Hall in the 1950s that the addition of 20 at% Al to bcc α -Fe causes a factor of 3 increase in its λ_{100} value [55, 28, 56]. The addition of 7 at% Be to Fe increases the magnetostriction by a

factor of two [57]. In the late 1970's the group at the Naval Ordnance Laboratory discovered that Terfenol-D ($\text{Fe}_{1.9}\text{Te}_{.3}\text{Dy}_{.7}$) exhibits a magnetostriction of up to 1000 ppm, an increase of a factor of 20 above pure Fe[30]. Despite the high magnetostriction present in Terfenol-D, this particular material is difficult to use in applications because it is quite brittle which prevents it from operating under tensile loads.

In 2000 Guruswamy *et al.* found that the addition of Ga to Fe could result in an increase of the magnetostriction up to 110 ppm in (110) textured alloys [58]. The choice of Ga was based on the large magnetostriction exhibited by Fe when it is alloyed with Al and Be. It was postulated that magnetostriction can be increased in Fe by alloying in elements with either empty or filled d shell orbitals, and Ga has a filled d shell. Subsequent studies have demonstrated that the dependence of the magnetostriction on Ga content, resembles that of Fe-Al with two maxima as a function of composition and a strong dependence on heat treatments [59, 2]. The trend of magnetostriction as a function of composition is illustrated in Figure 3.1. In particular, the two maxima have about the same value of magnetostriction ($\lambda_{100} = 270$ ppm) and occur at 20 at% and 28 at% Ga content.

Elastic constant measurements of Fe-Ga have revealed that the presence of the higher Ga content peak is associated with a decrease in the shear modulus C' , which may indicate the approach to a martensitic transformation [60, 2]. The positioning of the first peak in composition correlates roughly with the appearance of an ordered phase in the Fe-Ga phase diagram, as shown in Figure 3.2. This low Ga content peak is strongly dependent upon the heat treatment of the sample, with quenched samples showing higher magnetostriction than furnace-cooled samples. The presence of this peak has been postulated to be caused by a peak in

the magnetoelastic coupling brought on by the establishment of an ordered DO_3 phase[61], although the peak in magnetostriction occurs slightly before the equilibrium phase diagram shows DO_3 to be stable. The actual effect of the ordering, whether it is beneficial or deleterious to the magnetostriction, has not been firmly established. Figure 3.3 shows a comparison of the magnetostriction data obtained by Clark *et al.* and the known equilibrium phase diagram of Fe-Ga. Notice that the first peak in magnetostriction occurs near the boundary between α -Fe and the DO_3 phase.

An alternative explanation for the presence of the first peak in magnetostriction is the presence of a non-coarsening nano scale precipitate of the DO_3 phase(called a K-state)[62]. The nano-phase would originate from the competition between the thermodynamically stable bcc phase and an underlying fcc phase. Due to the stress from the surrounding α -Fe the DO_3 would be distorted into either an L1_2 or some modulated structure. The high magnetostriction would therefore be the result of reversible switching between tetragonal phases, reminiscent of the MFIS discussed in Chapter 1. It is possible that the value of magnetostriction reported to date in bulk Fe-Ga is only a lower bound. In fact, there have been reports of melt-spun alloys of Fe-Ga near the DO_3 boundary exhibiting magnetostrictions of 2000 ppm [63].

One of the more promising applications for Fe-Ga is in MEMs application, but to date there has been little work on nano-scaled Fe-Ga. McGary *etal.* have demonstrated the formation of Fe-Ga nanowire arrays using electrochemical deposition [64]. Successful epitaxial fabrication of $\text{Fe}_{81}\text{Ga}_{19}$ on Cu buffered Si was reported by Weston [65, 66]. Dunlap *et al.* used a combinatorial sputtering system to form

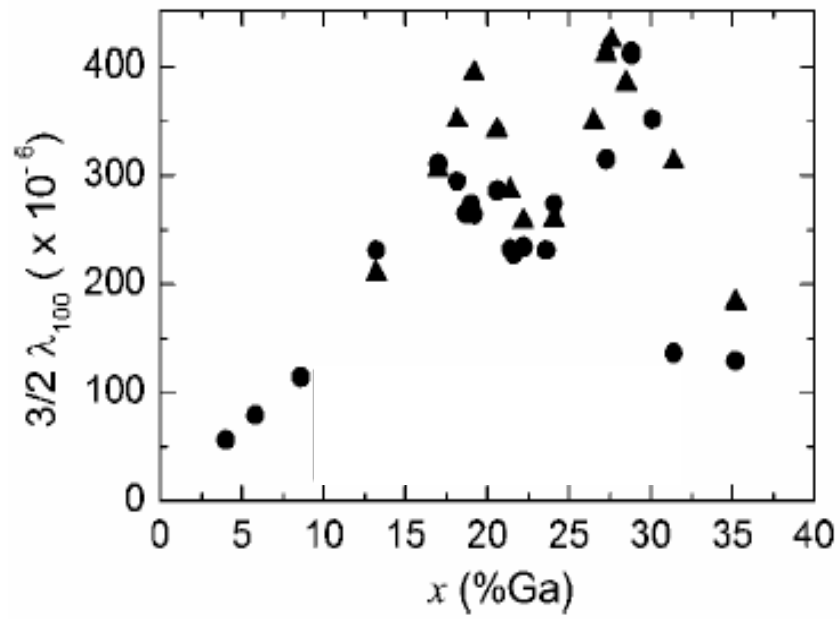


Figure 3.1: Compositional dependence of magnetostriction in Fe-Ga. Taken from [2]. The black circles are furnace-cooled samples and the triangles are from quenched samples.

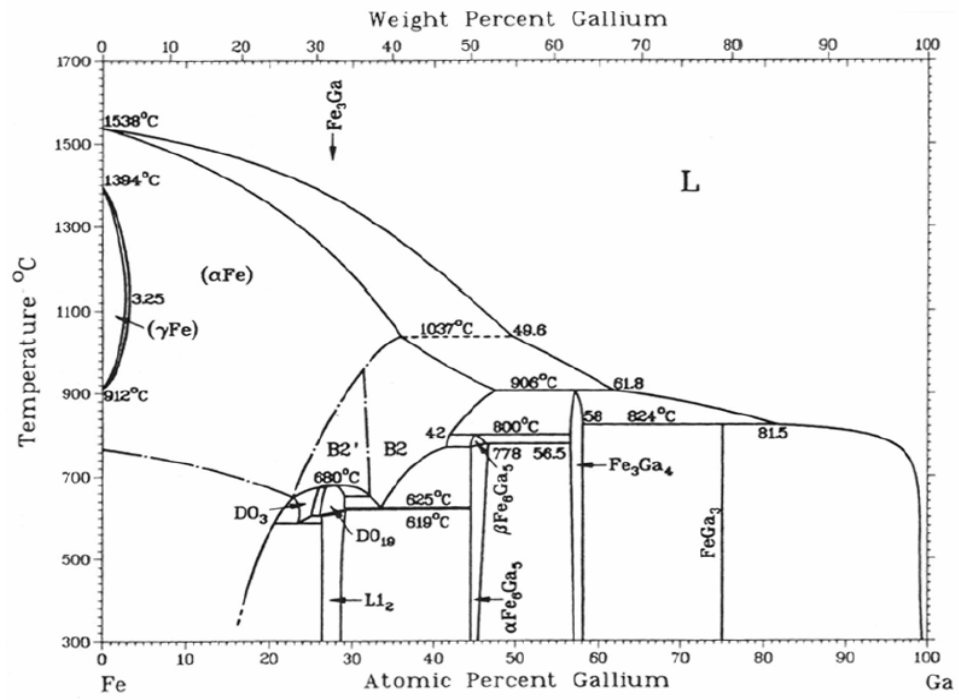


Figure 3.2: The binary phase diagram for Fe-Ga from. Taken from [3]

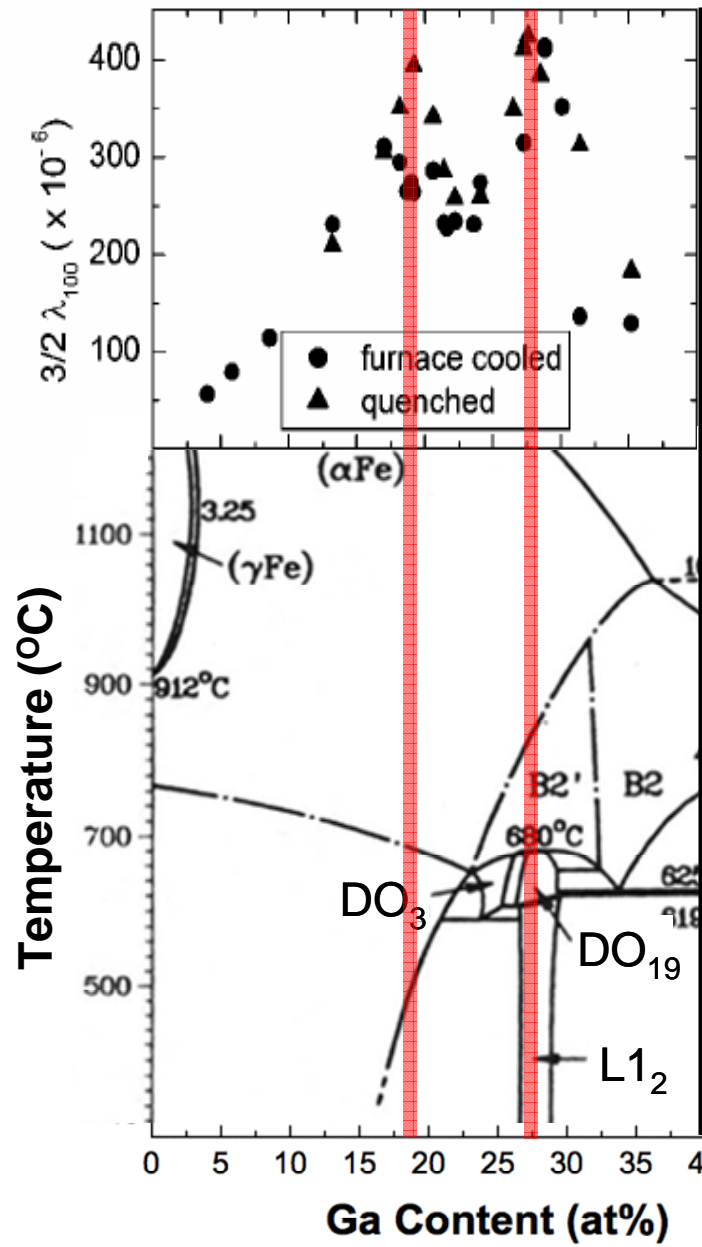


Figure 3.3: A comparison of the magnetostriction data (plotted in $3/2 \lambda_{100}$) and the binary phase diagram. Notice that the first peak in magnetostriction occurs before the actual onset of the appearance of the DO₃ phase.

Fe-Ga composition-spread samples for Mossbauer studies and showed the Ga clustering starts at relatively low Ga concentrations [67]. In addition to these works, a few groups have previously reported measurements of thin-film magnetostriction in Fe-Ga. A group at Tokai University has reported the thin-film values of magnetostriction for sputtered Fe-Ga [68]. The films were prepared with Ga compositions in the range from 2 at% Ga to 21 at% Ga, exhibited magnetostrictions as high as 180 ppm, or about 2/3 of the values reported in bulk. Stadler *et al.* have reported values of magnetostriction as a function of composition over a large range of compositions [69]. However the values reported were 1/3 of the bulk values, and the peaks in magnetostriction were shifted to lower Ga contents.

3.2 Binary Fe-Ga Thin-Film Preparation

The samples were prepared in our UHV sputtering chamber. The base pressure was 5×10^{-8} Torr, and the samples were deposited at a pressure of 4.6×10^{-3} Torr of Argon. The targets used for this investigation were elemental Fe and intermetallic Fe_2Ga_3 , both with at least 99.95% purity. The Fe_2Ga_3 intermetallic targets were provided by Larry Jones at Ames Lab. In each experiment the Fe and Fe_2Ga_3 targets were DC sputtered at 70 and 40 Watts, respectively. The nominal target-substrate distance was 12.5 cm, and the depositions were conducted for 1.5 hours, yielding a total film thickness of 0.6 μm .

During depositions using sputtering the elements in the plasma plume have energies ranging from 1 to 10 eV. Upon incidence with the substrate surface the time scale for the loss of this energy is of the order of 10^{-12} sec. The quenching rate is therefore 10^{16} K/sec, which is orders of magnitude larger than what can be achieved when quenching from melts[70]. The extremely high quenching rate can

capture high temperature phases without the need for subsequent anneals. However, care must be taken to do careful structural studies of as-deposited samples to ensure the correct crystal structure was obtained. In the present study the as-deposited films were found to have the desired bcc crystal structure. Therefore the substrate temperature was maintained at room temperature during deposition and no post-deposition heat treatments were used in this study.

In this study only cantilever samples were made and characterized. The cantilever libraries were oriented with the targets on opposite sides of the rows of cantilevers to allow a binary composition gradient of Fe and Ga to be formed along the rows of cantilevers. A picture of a typical cantilever library is shown in Figure 2.4. All discussions of properties will be limited to the top two rows of the spread.

Magnetization vs. applied magnetic field curves were taken for representative cantilevers to ensure the films have good magnetic properties. Figure 3.4 shows one such curve for a 500 nm $\text{Fe}_{90}\text{Ga}_{10}$ film where the saturation field is about 1.2 kOe and the coercivity is less than 200 Oe. This value of saturation field is consistent with the saturation field of magnetostriction seen in the thin-film samples. The saturation magnetization is about 1400 emu/cc and compares well with bulk work[34].

3.3 Microstructure of Fe-Ga Spreads

Structural characterization of the Fe-Ga binary composition spreads was undertaken using a combination of XRD and transmission electron microscopy (TEM). XRD studies were done as an initial structural screening technique to ensure the

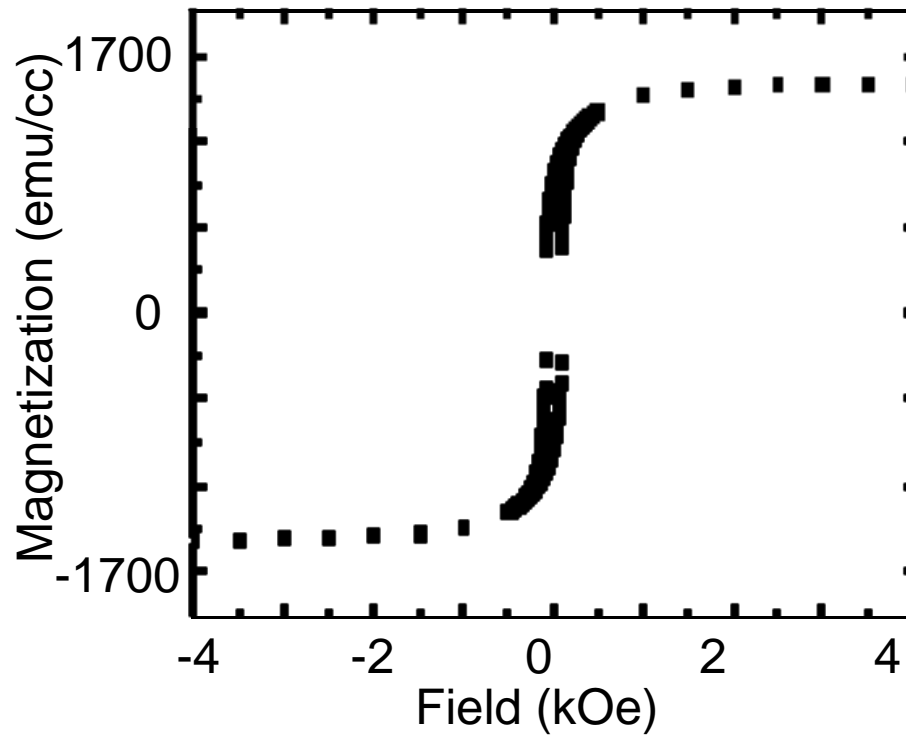


Figure 3.4: Magnetization vs. applied magnetic field curve for a representative 500 nm $\text{Fe}_{90}\text{Ga}_{10}$ thin-film cantilever. The saturation field is found to be about 1.2 kOe, and the coercivity is less than 200 Oe. The saturation magnetization observed is 1400 emu/cc.

proper phase had been captured during depositions and also to approximate the region of solid solution. Subsequent TEM studies were undertaken to check the system for the grain size of the primary phase, nano-scaled precipitation of secondary phases, and the presence of ordered phases.

Figure 3.5 shows the summary of an XRD study across a row of cantilevers. Here the Ga composition varies from 2.48 at% to 49 at% across the row. A weak (110) bcc-Fe type reflection is seen throughout the composition region mapped in this study and is located at around 44° , indicating the appropriate phase was obtained. This corresponds to a cubic lattice parameter of .24nm. The intensity distribution in χ in raw 2-dimensional diffraction images indicated a (110) planar texturing. An example 2θ vs χ scan is shown in Figure 3.6. It shows the planar texturing of the sample with the broad ring at a 2θ of 45° (note that in the raw images angle goes from high (left) to low (right)). The change in angle of the bcc-Fe peak is roughly linear throughout the region mapped. The linear region shown in Figure 3.5 is marked with a black line, and as a first order approximation the region of linear change in the bcc-Fe peak is taken to be the region of solid solution.

Selected area diffraction patterns (SADP) taken via TEM (Figure 3.7) confirm that the samples have the planar-textured (110) orientation. No large-scale precipitation of secondary phases was observed throughout the composition region studied. The presence of ordering along the (100) direction of the bcc-type structure would manifest itself as the appearance of a “forbidden” (100) peak in the diffraction pattern. The presence of the (100) rings was seen in all of the selected area diffraction patterns (SADP) taken, even for Ga content as low as 13.2 at %,

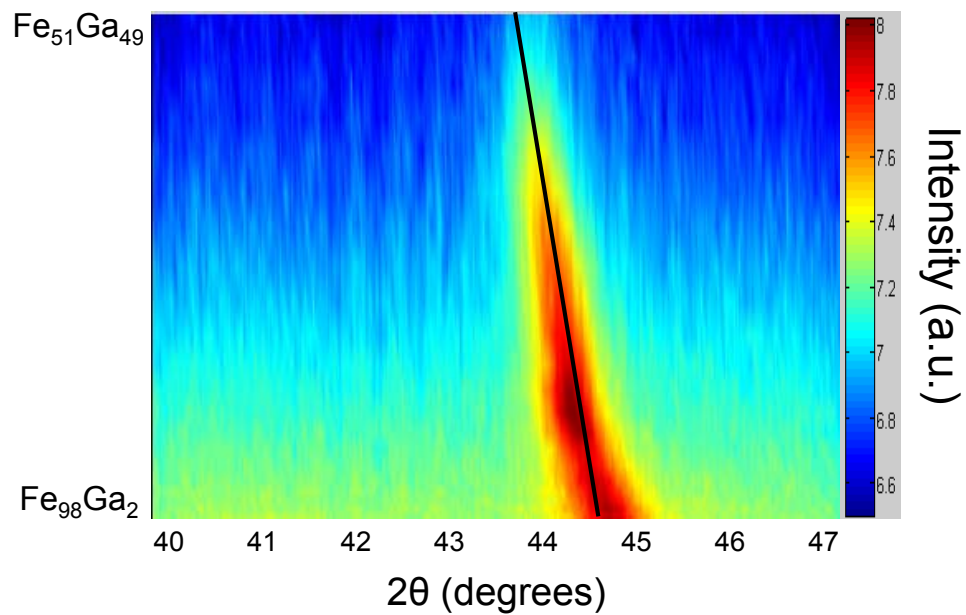


Figure 3.5: The XRD peak position of bcc-Fe peak ((110) reflection) as a function of Ga composition. The black line is a linear fit to the shift of the peak, and indicates the “solid-solution” region of the spread film. The quality of the fit (R^2) value for the line is 0.9314.

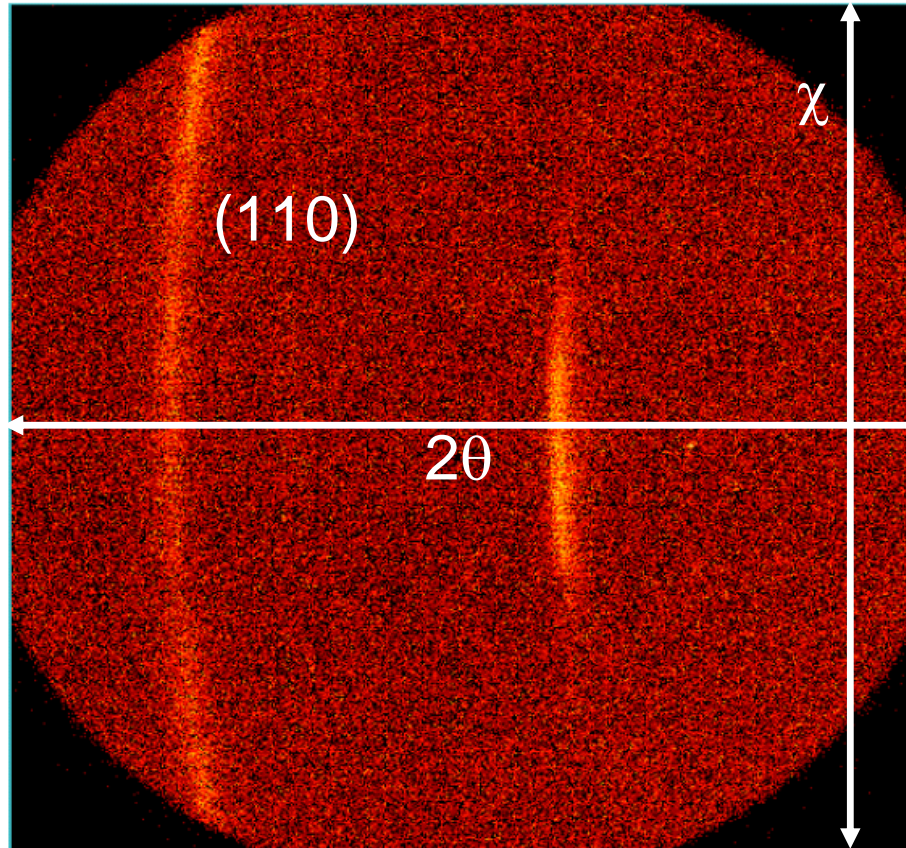


Figure 3.6: A representative raw 2θ vs. χ image from the 2-dimensional XRD detector showing evidence of the planar texturing of the thin-film samples. Here, the left most peak is the (110) reflection.

where neither the equilibrium phase diagram nor the metastable phase diagram indicate the DO_3 phase can exist. It is possible, however, that the K-state region extends to lower compositions than the phase diagrams indicate and the formation of the DO_3 phase may be possible even at such low Ga contents. An alternative explanation for the presence of the (100) peak is surface amorphization of the samples during milling. Further TEM studies are being undertaken to determine the true cause of the (100) peak.

Plan-view TEM images of the sample reveal grain sizes of about 20-30 nm, as seen in Figure 3.8. Cross section studies (Figure 3.9) show that the films have formed columns that extend out of the plane of the substrate. The source of the columns is most likely due to an initial growth of the grain at the film/ SiO_2 interface, which grows rapidly into a widening column during deposition. Faceted growth of the samples is manifested in the roughness of the film surface after deposition. The columns are inclined with respect to the surface of the substrate, which is most likely related to the incident angle of the deposited material.

3.4 Magnetostriction in Fe-Ga Composition

Spreads

Measurements of the magnetostrictive response of the cantilevers in the libraries was performed using the system described in Chapter 2. The light chopper was set at a frequency of 300 Hz, and the DC magnetic field was ramped at 20 mHz over a field range of ± 0.2 T. The data were taken over 5 magnetic-field cycles to help account for PSD drift and scatter. The data were then averaged and

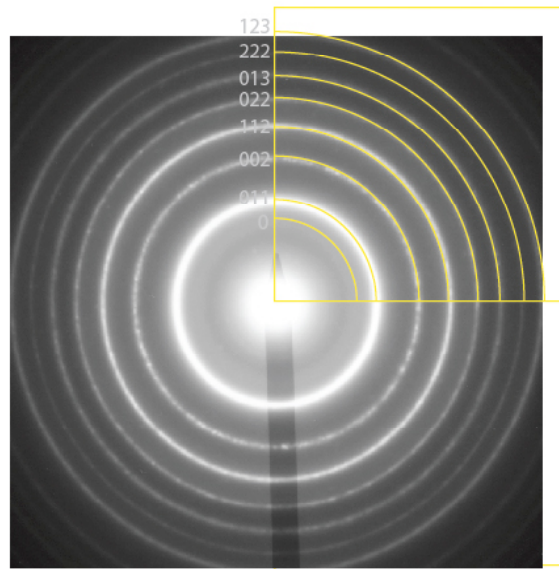


Figure 3.7: Selected area diffraction pattern of the $\text{Fe}_{65}\text{Ga}_{35}$ thin-film sample. The planar texturing(110) is evidenced by the obtained ring patterns. Courtesy of Leonid Bendersky.

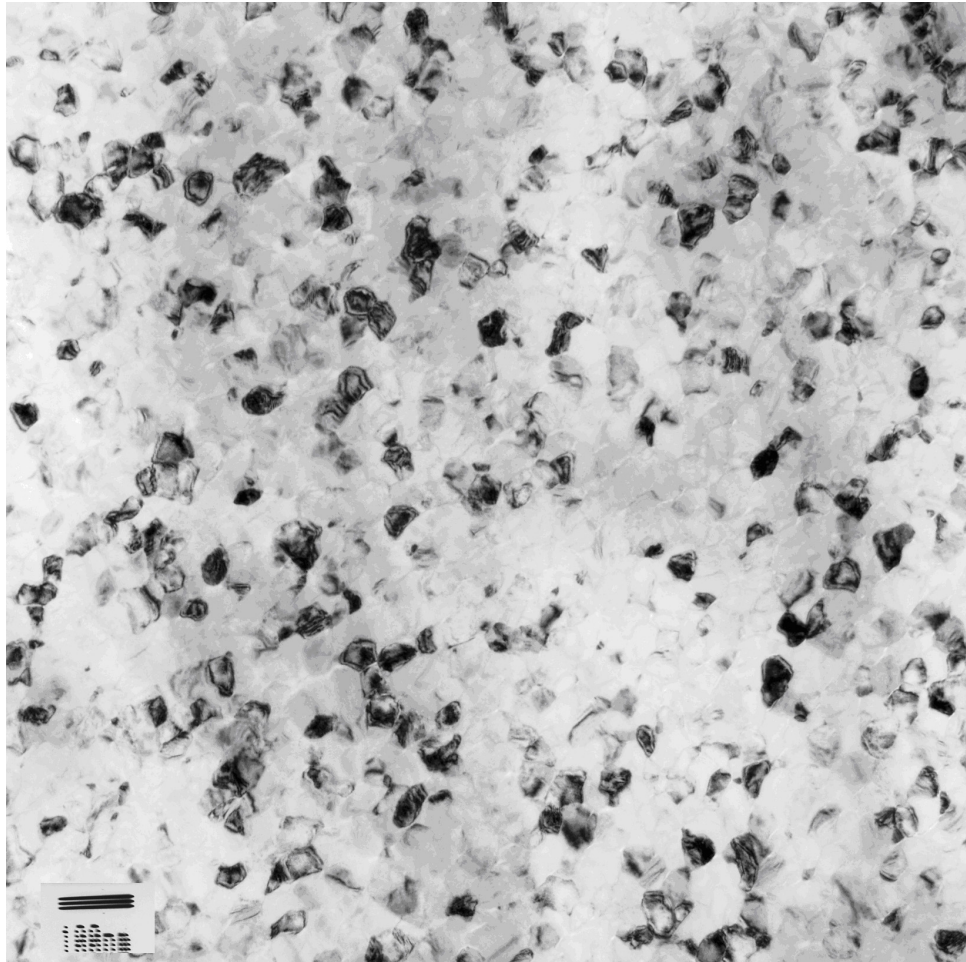


Figure 3.8: A bright-field plan-view TEM image of an Fe₆₅Ga₃₅ thin-film sample taken normal to the film surface. The grain size is 20-30 nm. The contrast is due to different crystalline orientations. Courtesy of Leonid Bendersky.

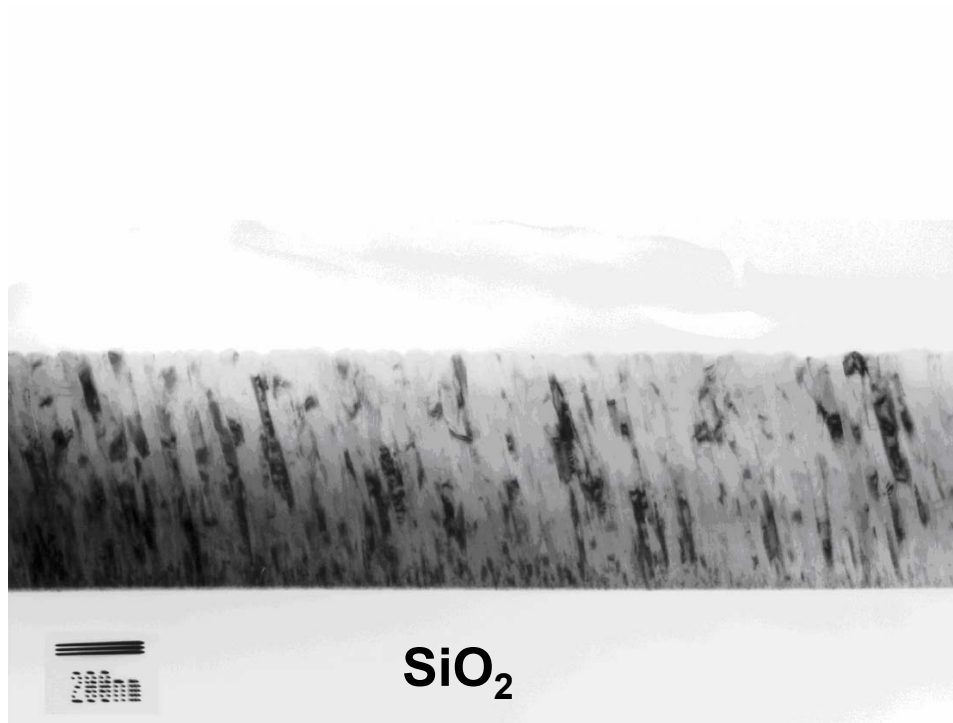


Figure 3.9: Bright-field cross-section image of an $\text{Fe}_{65}\text{Ga}_{35}$ thin-film sample from a composition spread. A columnar structure is observed grown at angle with respect to the substrate. Image courtesy of Leonid Bendersky.

smoothed to give reliable values for striction. The first two cantilever rows of the binary spread were measured, which led to two sets of magnetostriction data over the same composition region without introducing calculation errors brought about by thickness inhomogeneity. The thicknesses of the film and cantilever were measured for every third cantilever using cross-sectional scanning electron microscope (SEM). Linear interpolation was used to estimate the thicknesses for the remaining cantilevers.

Since no masking systems were employed to guarantee constant composition on each cantilever, and since each cantilever has finite dimensions 2 mm wide and 8 mm long, it is important to determine how much the composition changes across each cantilever. To quantify the variation in composition across each cantilever a series of WDS studies were undertaken where the base of each cantilever was measured three times; once at the center of the base and one at either edge of the base. The center point was taken to be the composition primarily responsible for the deflection of the cantilever. The two edge points were used to calculate how much the composition of the base deviates from the center. The measurement scheme for quantifying the compositional error in the cantilever libraries is illustrated in Figure 3.10. It was found that the compositional error across the base of each cantilever was no more than 1.5 at%. Measurements along the length of the cantilever were also taken, and found to be the same as the variation in the width direction. It should be noted that the accuracy of the composition in these graphs is only limited by the composition gradient across the cantilever. Measurements of elements using properly calibrated WDS is better than .01 at %.

Figure 3.13 shows the results of the magnetostriction measurement from two rows of the Fe-Ga binary spread wafer. The values of magnetostriction were calcu-

lated using the Lachiesserie method discussed in Chapters 2. Here, the value of the effective magnetostriction is seen to reach a peak of 56 ppm. To more effectively compare the trend and value of the magnetostriction observed in the thin-film spread sample with bulk data, the two are plotted together in Figure 3.14. Here, for clarity, the data from the first row only are plotted with bulk data for samples quenched from high temperature[2]. Since λ_{100} is known to be the dominant magnetostriction constant, bulk data for $3/2 \lambda_{100}$ is compared to λ_{eff} obtained from our thin film data. The two high-Ga-content maxima are present in the thin-film samples, although at slightly higher Ga content than those reported in bulk studies (19 at% vs. 21at% and 28 at% vs 31 at%). The general trend of the magnetostriction, however, is consistent confirming that measurements of λ_{eff} in textured Fe-Ga thin-films are appropriate for mapping trends in magnetostriction.

The shift in the peak in composition could be due to a number of reasons. From the derivation of λ_{eff} we know that λ_{111} is also contributing to the observed behavior. Since it is known that the value of λ_{111} undergoes an abrupt change in sign around 21 at% Ga to a positive value, this is likely affecting the observed value of λ_{eff} [4]. In addition, the compositional gradient present in each cantilever, typically 1 at% from top to bottom, and residual stresses in the film from deposition can lead to a deviation in magnetostriction behavior from bulk behavior.

The effect of λ_{111} on the mapping of the compositional trend of the effective magnetostriction (λ_{eff}) must be carefully considered, as it could affect the overall value of magnetostriction measured here, as well as its compositional dependence (*i.e.* the positions of the peaks). The published compositional dependence of $3/2\lambda_{111}$ on Ga content in bulk is shown in Figure 3.11. What is observed is that it is small (30 ppm), negative, and roughly constant for low Ga contents.

At about 19 at % Ga λ_{111} changes sign and increases value to roughly 40 ppm. The compositional dependence of λ_{111} is roughly linear with a small slope for the remaining points taken.

Although the values of λ_{111} are quite small compared to λ_{100} , the (110) texturing prefactors differ by a factor of 4, and this could mean that λ_{111} might have substantial contribution to the λ_{eff} for the composition region of interest in our samples. To see the additive effect of the contributions of λ_{100} and λ_{111} in the composition range 15 at% Ga to 33 at% Ga, we look at the ratio of contributions of λ_{100} and λ_{111} (with appropriate prefactors) as a function of Ga content for the published bulk data (Figure 3.12). What this shows is first that in the region of large λ_{100} , λ_{eff} should be predominantly determined by the λ_{100} term. That the ratio of the two contributions approaches 1 at higher Ga contents is a possible source of error in identifying the position of the peaks in magnetostriction in Fe-Ga using our method. Although the number of points taken for values of λ_{111} are sparse in the bulk study, studying the ratio of the relative contributions indicates that in the region of composition near $\text{Fe}_{81}\text{Ga}_{19}$ the value of λ_{eff} mostly comes from the λ_{100} term. But, it is difficult to definitively extract a value for λ_{100} from our present study.

It should be noted, however, that the values calculated for λ_{eff} using the available bulk values for λ_{111} and λ_{100} and the planar-texturing model discussed in Chapter 1 are consistent with the values of λ_{eff} measured here. Thus, we have demonstrated quantitative measurements of magnetostriction with the current thin-film combinatorial measurement technique.

A third maximum in magnetostriction, which has not been previously reported,

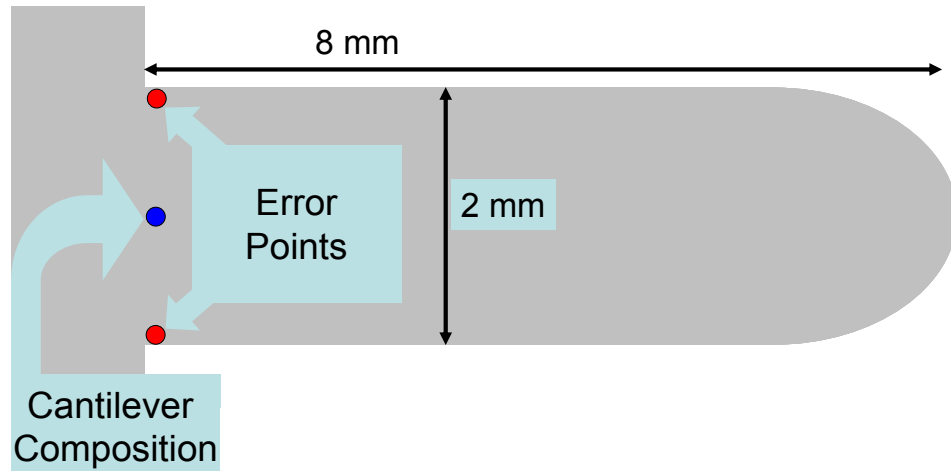


Figure 3.10: A schematic of how the compositional error across a single cantilever was measured. A point, taken to be the composition primarily responsible for deflection, was taken at the center of the base of the cantilever. Two points at either edge of the base of the cantilever were used to identify the compositional inhomogeneity of the cantilever. Measurements were also taken along the length of the cantilever.

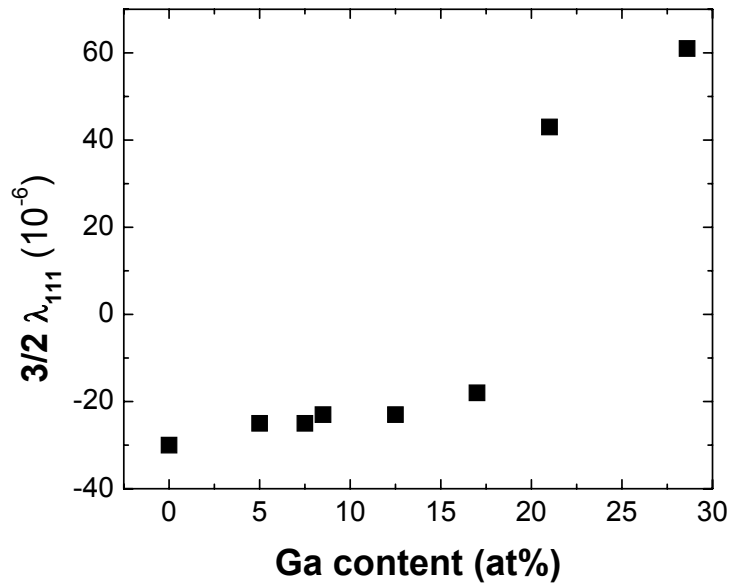


Figure 3.11: The compositional dependence of $3/2 \lambda_{111}$. It is seen that λ_{111} is small and negative for low Ga contents and then abruptly changes sign at 19 at % Ga. Taken from [4].

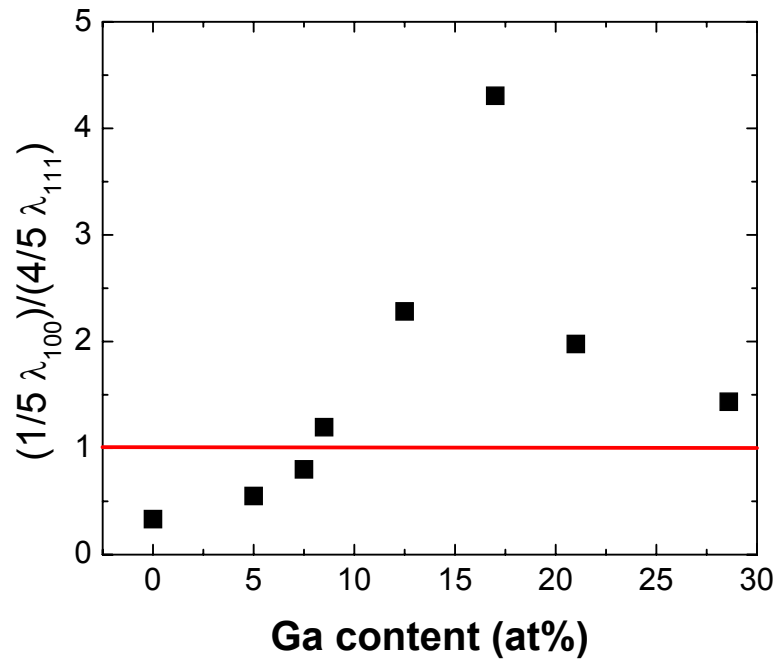


Figure 3.12: The compositional dependence of the ratio of $4 \lambda_{100}/5 \lambda_{111}$. The red line marks where the ratio is 1. In the high Ga content region the contribution to λ_{eff} of λ_{100} is greater than or equal to that of λ_{111} . Data taken from [4].

is observed to occur at around 4 at% of Ga. The value of magnetostriction at this local maximum is 19 ppm, approximately 1/3 of the value seen at the other two maximas. It has been reported that the magnetocrystalline anisotropy and magnetic moment of Fe atoms in Fe-Ga alloys peak at about 5 at% Ga content, and it is believed that this is related to the observation of a third peak in magnetostriction[34, 71].

Figure 3.15 shows a comparison of the trend in magnetostriction of our thin-film samples with the binary Fe-Ga phase diagram. It is seen that there is a strong correlation between the onset of the maxima in magnetostriction and changes in phase. The low Ga content peak is seen to occur near the phase boundary between (fcc) γ -Fe and (bcc) α -Fe. The next peak in magnetostriction occurs at the transfer from pure α -Fe to the mixed α -Fe/DO₃ region. The final peak in magnetostriction is present at the high Ga edge of the DO₁₉ phase. The appearance of the maxima in magnetostriction near phase boundaries in Fe-Ga, particularly the DO₃ phase boundary, is well established. That a third peak in magnetostriction is seen to occur near the γ -Fe α -Fe phase boundary can be taken as a possible indication that the enhancement of magnetostriction is closely tied to competition of bcc and fcc phases.

3.5 Conclusion

Measurements of the magnetostriction of binary Fe-Ga composition-spread samples have reproduced the expected bulk trends. Both major maxima are observed as a function of composition, although at slightly shifted compositions from bulk stud-

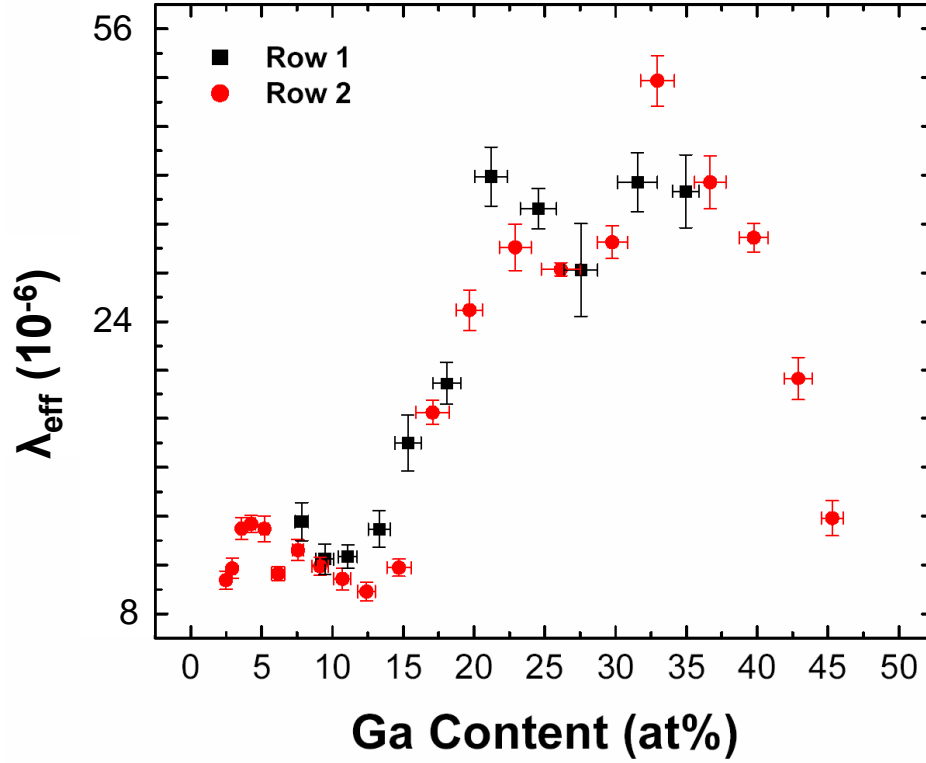


Figure 3.13: Compositional dependence of magnetostriction from two rows of a Fe-Ga thin-film cantilever unimorph composition-spread sample. Here, the rows represent the top two rows from the cantilever library. The black squares are from the first row and the red circles are from the second row. Three maxima are noted at 4, 21, and 31 at% Ga. $\lambda_{eff} = \frac{1}{5}\lambda_{100} + \frac{4}{5}\lambda_{111}$

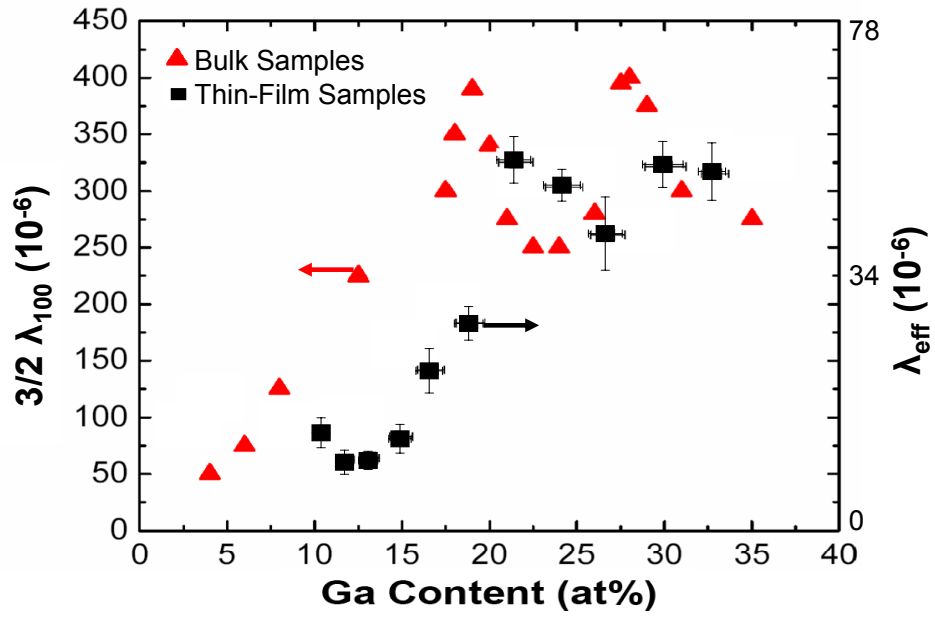


Figure 3.14: Comparison of the trend in magnetostriction as a function of composition between bulk studies (red triangles) and λ_{eff} measured from the present thin-film study (black squares). The bulk data were taken from [2]. $\lambda_{eff} = \frac{1}{5}\lambda_{100} + \frac{4}{5}\lambda_{111}$

ies. The shift in the peak composition has been attributed to the combination of the presence of compositional inhomogeneity along the length of single cantilevers, residual deposition stresses, as well as the sudden change in sign of λ_{111} at 21 at% Ga contents seen in bulk studies. A third minor maximum in magnetostriction is observed at about 4 % Ga and could be related to the peak in magnetocrystalline anisotropy and the magnetic moment of Fe in Fe-Ga. Comparison of the trend in magnetostriction with the Fe-Ga binary phase diagram shows strong agreement between the maxima in magnetostriction and phase changes, possibly giving further experimental weight to the theory of Khachatryan [62].

It is possible that the values of magnetostriction could be affected by the stress introduced during deposition of the thin-films. The most likely source of this stress would be a combination of the inefficient dissipation of heat through the substrate, due to its relatively low thermal conductivity, and the disparity between the thermal expansion coefficients of the film and the substrate. During long depositions, it is not uncommon for the heater stage to warm 5 K, although accurate measurements of the temperature change in the cantilevers is not possible. This could result in a gradient in the residual stress in the cantilevers caused by the different energies used for each target and the natural gradient of the plasma plume. Magnetostriction can be sensitive to tensile stresses, and there is the possibility that this stress gradient could shift the perceived peak in magnetostriction a few at% from the its “true” position in composition, by altering the unmagnetized domain configuration between cantilevers. In the present study the values and trend of magnetostriction are quite close to what is reported in bulk and indicate that residual stress from deposition is not a large source of error in peak position.

On the other hand, a possible benefit of this residual stress is to negate the

need for the use of perpendicular fields to gain the full value of the magnetostrictive constant. A moderate compressive stress along the length of the cantilever should be sufficient to force the domain structure to be almost completely comprised of 180° domains running perpendicular to the length of the cantilever. Upon the application of a magnetic field parallel to the length of the cantilever, magnetization will take place solely through rotation of the magnetic moments and the full magnetostriction will be obtained.

Chapter 4

The Effect of Ternary Additions to Fe-Ga on Magnetostriction

4.1 Introduction

In this chapter the effect of ternary additions on magnetostriction in the Fe-Ga system is addressed. First in I describe the reasoning behind introducing ternary additions to Fe-Ga, and comment briefly on previous bulk studies. I then proceed to discuss the effects of adding Pd and Al on the magnetostriction in Fe-Ga. Alterations to the trend in magnetostriction as a function of alloying, and the magnitude of magnetostriction are also addressed.

4.2 Motivation

Although $\text{Fe}_{1-x}\text{Ga}_x$ exhibits large magnetostriction (for $0.15 \leq x \leq 0.30$) the presence of Ga makes it unattractive for applications, because the large addition of Ga to Fe causes embrittlement of the alloy. It is therefore of interest to find a

ternary addition to Fe-Ga that can increase its workability. It is also a requirement that ternary alloying should preserve, or possibly enhance, the magnetostriction.

There have been several bulk studies undertaken to address this issue. It has been found that Sn, Al, and C are promising additives [72, 46, 6, 5]. But these efforts were primarily focused on ternary additions in the region of $\text{Fe}_{81}\text{Ga}_{19}$ and thus did not address the effect of ternary additions to the composition with the minimal value of C' . In addition, such bulk studies are often limited to a few points in composition space that may not coincide with promising compositions. In individual composition studies, one also faces run-to-run variations.

Here we have focused on the effect of the ternary additions of Pd and Al on the magnetostriction of Fe-Ga. Pd was chosen, despite its low solid-solubility in bcc Fe, due to its ability to decrease C' in solid solution with fcc Fe [31]. It was expected that the natural quenching provided by sputtering would allow us to circumvent the low-solubility by artificially freezing Pd into the lattice. Thus it may be possible to observe the effect of elements that lower C' although they are structurally disparate. Al was chosen because it has a large solubility in bcc Fe and forms the magnetostrictive material Alfenol [56].

4.3 Sample Preparation and Structural Characterization

The composition-spread samples were prepared in our UHV sputtering chamber. The base pressure was 5×10^{-8} Torr, and the samples were deposited at a pressure of 4.6×10^{-3} Torr in argon. The targets used for this investigation were elemental Fe, Al, Pd and intermetallic Fe_2Ga_3 , all with at least 99.95% purity. In each

experiment the Fe and Fe₂Ga₃ targets were DC sputtered at 70 and 40 Watts, respectively. The third element (Pd or Al) were sputtered with either RF or DC power supplies with powers ranging from 5 to 40 Watts. The nominal target-substrate distance was 12.5 cm, and the depositions were conducted for 1.5 hours yielding a total film thickness of 0.6 μm . No post-deposition heat treatments were used in this study.

In this study only cantilever samples were made and characterized. The cantilever libraries were oriented with the Fe and Fe₂Ga₃ targets on opposite sides of the rows of cantilevers to allow a binary composition gradient of Fe and Ga to be formed along the rows of cantilevers. Meanwhile the third element provided a composition gradient perpendicular to the rows. This arrangement provided samples where each row had a roughly constant concentration of the ternary element.

TEM and XRD results on the as-sputtered libraries indicated that all samples were (110) out-of-plane textured and nano-crystalline with an average grain size of 25 nm. They also confirmed a planar texturing of the films.

It is useful to approximate solid-solution in these ternary systems using the XRD data. To do this a 3-D analogue to the rule of mixtures used in Chapter 3 is necessary. In Chapter 3 a linear fit was used to fit a continuously changing lattice constant accompanying changing composition as an approximation to the rule of mixtures in binary Fe-Ga. In order to expand this approach to ternaries we must first determine the best way to plot the ternary composition information along with the XRD data. In the case of a binary system, complete X-ray spectra can be plotted together in a straightforward way using the three coordinate axes as composition, XRD peak position (2θ), and intensity. It is often convenient to use a color bar to emphasize the change in one dimension as was done for the case

of intensity in Figure 3.5. This way a 3-dimensional plot can be reproduced in 2 dimensions. A top down view of the composition-peak position plane allows the fitting of a line to the change in peak position as a function of composition.

In order to extend this scheme to a ternary system an extra dimension is needed. In the case of ternary mappings/plotting schemes, an entire plane has to be devoted to composition, leaving only the third axis to account for either peak position or intensity. In approximating solid solution a volumetric plot of composition and peak position is constructed, as shown in Figure 4.1 for the case of an X-ray diffraction intensity plot for a Ni-Mn-Al ternary composition spread. In this graph the X-ray peak position for each phase is plotted versus composition. The xy plane is used to plot the ternary diagram and the z axis is used to plot angle. Each dot represents a peak at that particular composition. This graph was constructed using a data visualization program based on Matlab, called XRDsuite. XRDsuite is freeware written by our group to facilitate data visualization in combinatorial experiments[73]. A major feature of the program is that it generates 3-D plots, which are freely rotatable, allowing one to view the images from various perspectives to gain a better understanding of the effect of composition on crystal structure.

For Fe-Ga-Al and Fe-Ga-Pd ternaries, the solid solution region was approximated using the rule of mixtures to extrapolate the change in the lattice parameter. The composition and XRD data were plotted in the volumetric plot described above using XRDsuite and a special add-on feature was implemented in the software to allow the fitting of a plane to diffraction peaks in the 3-D volumetric spectra plots. The plane was fit to the change in angle of the (110) Fe peak as a function of composition. A schematic of this is shown in Figure 4.2(a) for the case

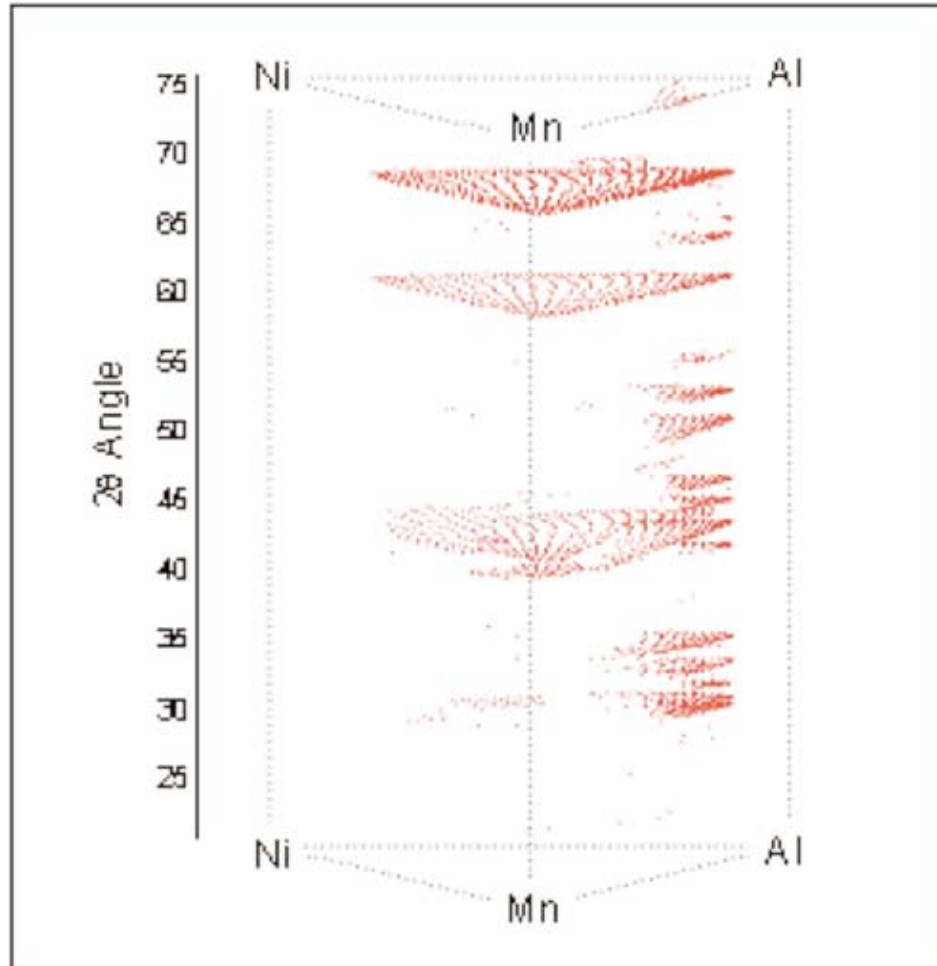


Figure 4.1: Volumetric plot of the compositional dependence of XRD peaks in the Ni-Mn-Al system. Ternary composition is mapped in the xy plane, and the 2θ angles. All major diffraction peaks are plotted as dots in the three dimensional space.

of Fe-Pd-Ga. Here, the plane used to approximate solid solution is shown intersecting the volumetric plot. Figure 4.2(b) shows the specific case of the α -Fe peak, where the figure has been rotated so that the fitting plane is projected as a line in the plane of the page. By plotting the volumetric in this manner it is possible to see how well the plane fits the change in the peak position as a function of composition. A more accurate measure of the fit can be obtained by taking the square of difference between the measured angle and the plane (called the residual) then plotting that on a ternary, as done here in Figure 4.3. The edge of solid-solution region was estimated to be where the residual exceeds a certain threshold value. This values was taken to be where the color code denotes the residual changes from dark blue to light blue in Figure 4.3. From this we find that the composition range showing solid solution α -Fe in our sputtered thin-film samples covers from pure Fe to 30 at% addition of either element. The significance of this is that through sputtering the bcc α -Fe has been stabilized in Fe-Pd sputtered thin-film samples possibly due to the addition of Ga. As the presence of α -Fe is a precursor for the presence of large magnetostriction, there exists the possibility of observing large magnetostriction over a large region of the phase diagram.

4.4 Magnetostriction of the Fe-Pd-Ga Ternary System

The first ternary system investigated was Pd-substituted Fe-Ga, where Pd was chosen because of its ability to soften C' . The magnetostriction was determined via the measurement system described in Chapter 2, and the calculation of λ_{100}

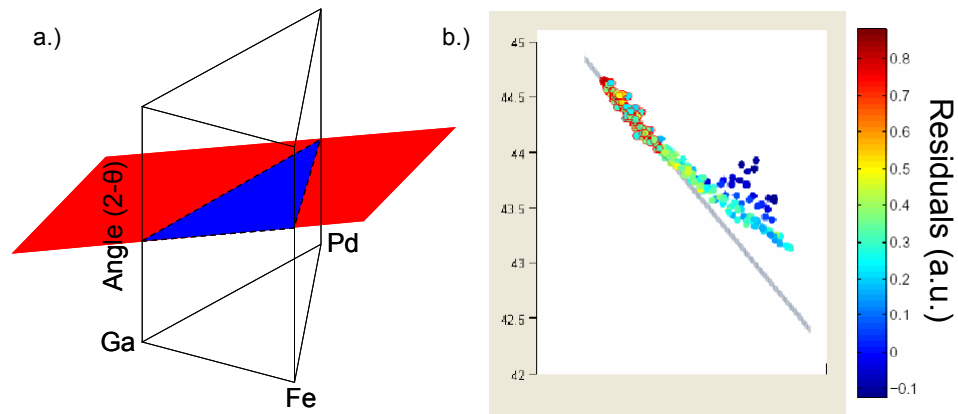


Figure 4.2: A schematic of the volumetric plot of the plane used to fit solid solution is shown in (a), where the region of the planes intersection with the plot is marked in blue. (b) shows the actual data where the ternary phase diagram has been projected to lie in the plane going into the paper and the y axis is the peak position of the α -Fe peak. The color bar is the residual between the plane fit and the measured peak positions and is used to approximate the solid solution region.

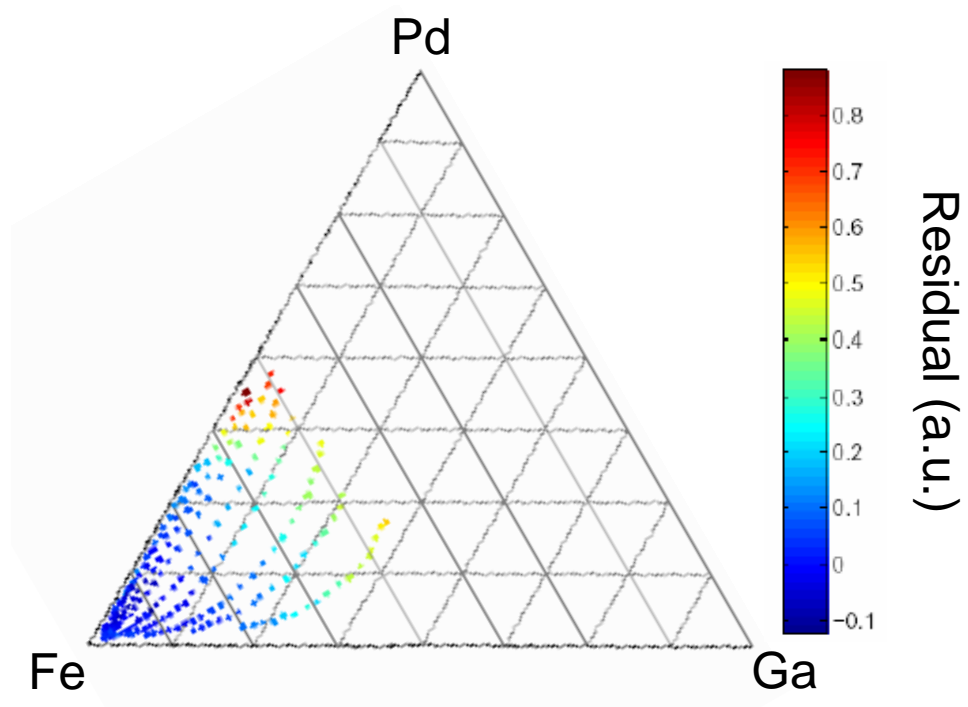


Figure 4.3: The variation of the residual between the measured angle and the approximated angle as a function of composition. The region of dark blue is taken to be the region of solid solution.

was done via the same technique described in Chapter 3. The light chopper was set a frequency of 400 Hz, and the DC magnetic field was ramped at 20 mHz over a field range of ± 0.3 T. The thickness of the films and cantilevers were measured by cross-sectional SEM for every third cantilever. A linear average was used to extrapolate the thicknesses for the remaining cantilevers.

The variation of magnetostriction obtained from the Fe-Pd-Ga composition-spread is shown in Figure 4.4, each of the five lines represent an individual row in the cantilever library. From the figure one can see that sizable magnetostriction is basically present only along the Fe-Ga binary edge of the phase diagram. The general region exhibiting magnetostriction seen here corresponds well with bulk Fe-Ga. The magnetostriction with 1 at% and 3 at% Pd both demonstrate a maximum value of λ_{eff} of 28 ppm. This is less than 1/2 of the value obtained in thin-film binary studies and underscores the fact that even small Pd can detrimentally affect the magnetostriction. For Pd alloying of more than 10 at%, magnetostriction effectively completely vanishes.

To properly understand the effect of Pd on the magnetostriction, a comparison of pseudo-binary Fe-Ga-Pd, where the Pd content is fixed and the Fe-Ga ratio has been allowed to change, with binary Fe-Ga is necessary. Figure 4.5 compares the trend of magnetostriction vs. Ga content for our thin-film binaries and a region of our Fe-Ga-Pd ternaries, where the Pd content has been set at 3.3at%. It is observed that the trend in magnetostriction has been significantly altered with the addition of only a small amount of Pd to Fe-Ga. A clear peak in magnetostriction is still observable for Ga contents of about 30 at%. In addition, there is another peak in magnetostriction at 10 at% Ga content whose origin is unknown at the moment. It could be that the Pd has helped to stabilize the γ -Fe phase, as it does at high-

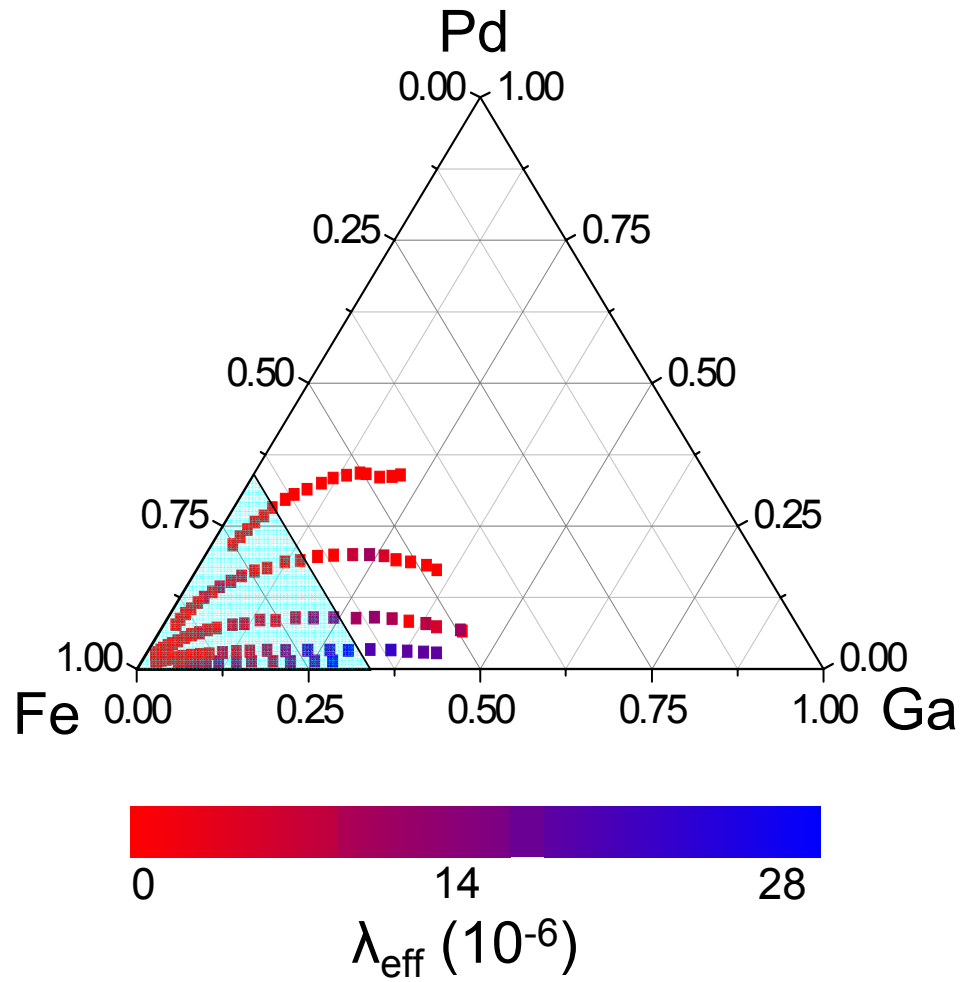


Figure 4.4: Variation of magnetostriction across the Fe-Pd-Ga ternary measured from the Fe-Ga-Pd cantilever library. The approximate area of solid solution region has been marked with the lightly shaded triangle. Each strip of data corresponds to a row in the cantilever spread, with a maximum of 5 rows per spread. The region along the Fe-Ga binary edge is the only region showing appreciable striction and correlates well with what is seen in bulk studies. $\lambda_{eff} = \frac{1}{5}\lambda_{100} + \frac{4}{5}\lambda_{111}$

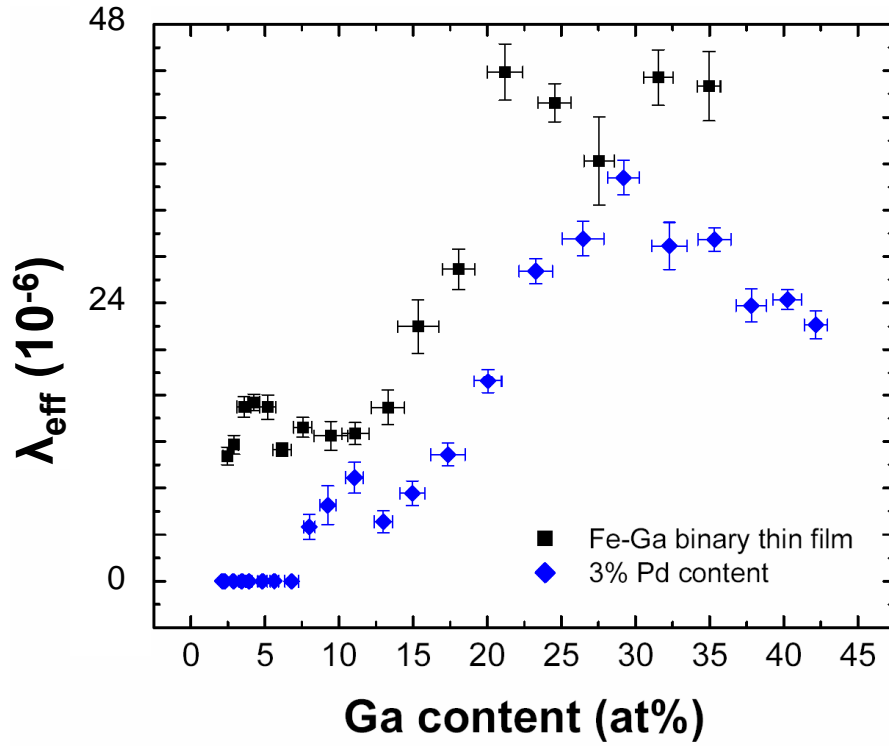


Figure 4.5: A comparison of the trend of magnetostriction as a function of Ga content of thin-film combinatorial samples of Fe-Pd-Ga with the trend of λ_{eff} observed in thin-film Fe-Ga. It is seen that the trend in magnetostriction is greatly changed by the addition of small amounts of Pd. $\lambda_{eff} = \frac{1}{5}\lambda_{100} + \frac{4}{5}\lambda_{111}$

temperatures in Fe-Pd binaries, to higher Ga contents. Further microstructural studies will be needed to confirm this. As a comparison the thin-film ternary Fe-Pd-Ga magnetostriction data is also plotted with bulk data in Figure 4.6.

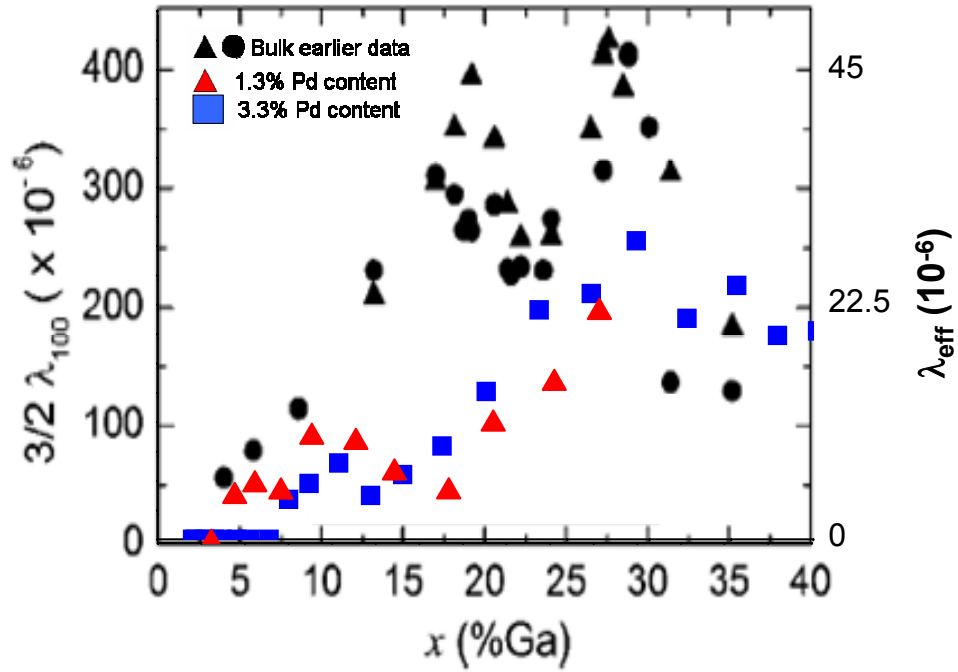


Figure 4.6: A comparison of the trend of magnetostriction as a function of Ga content of thin-film combinatorial samples of Fe-Pd-Ga with binary bulk Fe-Ga data from [2]. $\lambda_{eff} = \frac{1}{5}\lambda_{100} + \frac{4}{5}\lambda_{111}$

4.5 Fe-Ga-Al

The compositional dependence of magnetostriction in the Fe-Ga-Al phase diagram, measured using the same setup as for Fe-Ga-Pd, is shown in Figure 4.7. Here, a significant region displays appreciable magnetostriction. The bulk trends along the Fe-Ga edge are well reproduced with a clear peak at 30 at% Ga and a shoulder at 20 at% Ga. Also, it is observed that the trend of magnetostriction is similar to that of Fe-Ga if the magnetostriction is plotted vs. Ga+Al content, as seen for a representative row in Figure 4.8. Here the broadness is likely due to the composition gradient of Ga and Al across the cantilever. As Al is added into the system, the shoulder at 20 at% Ga exhibits a monotonic decrease. This contrasts reports for bulk samples with similar Al content [5, 6]. The peak at 30 at% Ga exhibits no significant degradation for Al substitutions up to 10 at%, after which the magnetostriction decreases monotonically. The peak does not follow the relationship $\text{Fe}_{70}\text{Ga}_{30-x}\text{Al}_x$, as the Fe content increases as the Al content increases. Most likely this reflects the fact that Al-Fe has a single maximum in magnetostriction, and the two peaks from Fe-Ga are collapsing into one. In the previous bulk study by Guruswamy *et al* these composition were missed because they kept the Fe content constant as they added Al. The assumption from such a study is that both $\text{Fe}_{70}\text{Ga}_{30}$ and $\text{Fe}_{70}\text{Al}_{30}$ exhibit related peaks in magnetostriction, however Fe-Al only exhibits a peak at 20 at% Al[33]. We have shown that the magnetostriction in $\text{Fe}_{70}\text{Ga}_{30}$ is insensitive to the addition of moderate amounts of Al. This region along with the data taken by Guruswamy *et al* are shown in Figure 4.9. The replacement of Ga with Al while maintaining comparable magnetostriction will help

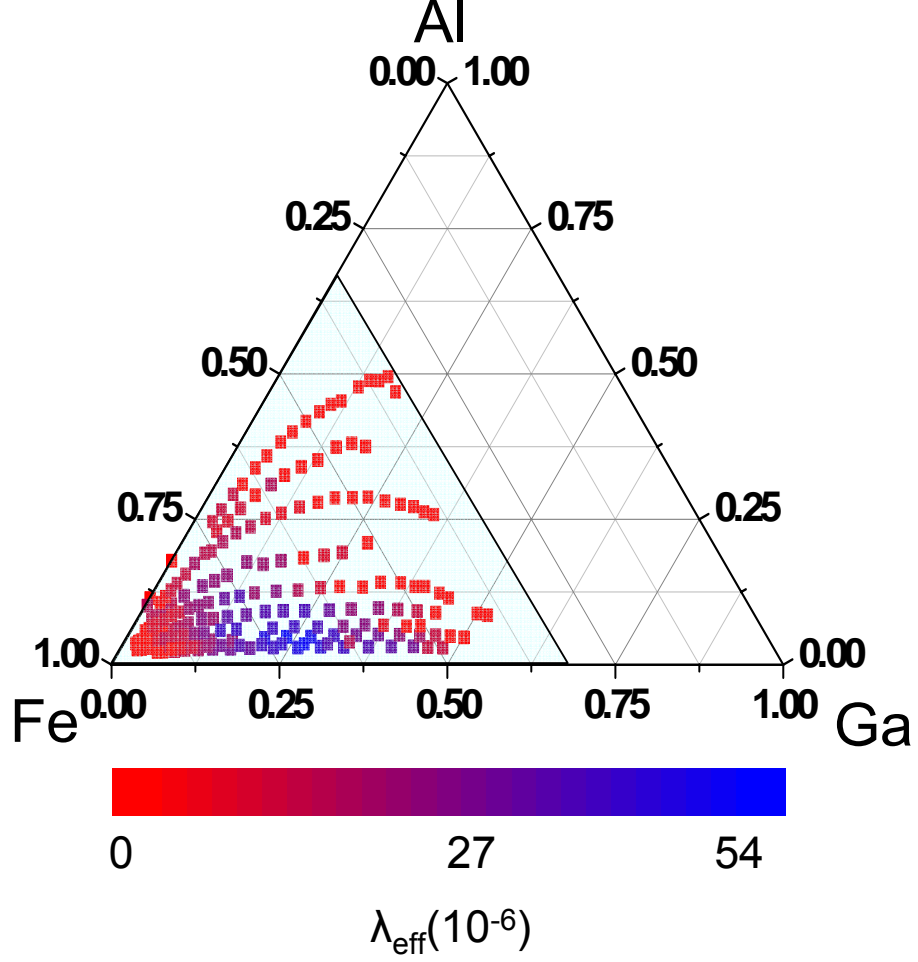


Figure 4.7: The variation of magnetostriction λ_{eff} in the Fe-Ga-Al ternary system measured using the thin-film composition-spread Fe-Ga-Al cantilever library. The area of solid solution has been marked with a colored triangle. Here, there is significant magnetostriction over a large area of compositions spanning from Fe-Ga to Fe-Al. The trend in the data is identical to what is seen in bulk, indicating Al additions do not affect the compositional dependence of magnetostriction in Fe-Ga [2]. A large region near $\text{Fe}_{70}\text{Ga}_{30-x}\text{Al}_x$ for $x \leq 10$ was found to be insensitive to Al additions. $\lambda_{eff} = \frac{1}{5}\lambda_{100} + \frac{4}{5}\lambda_{111}$

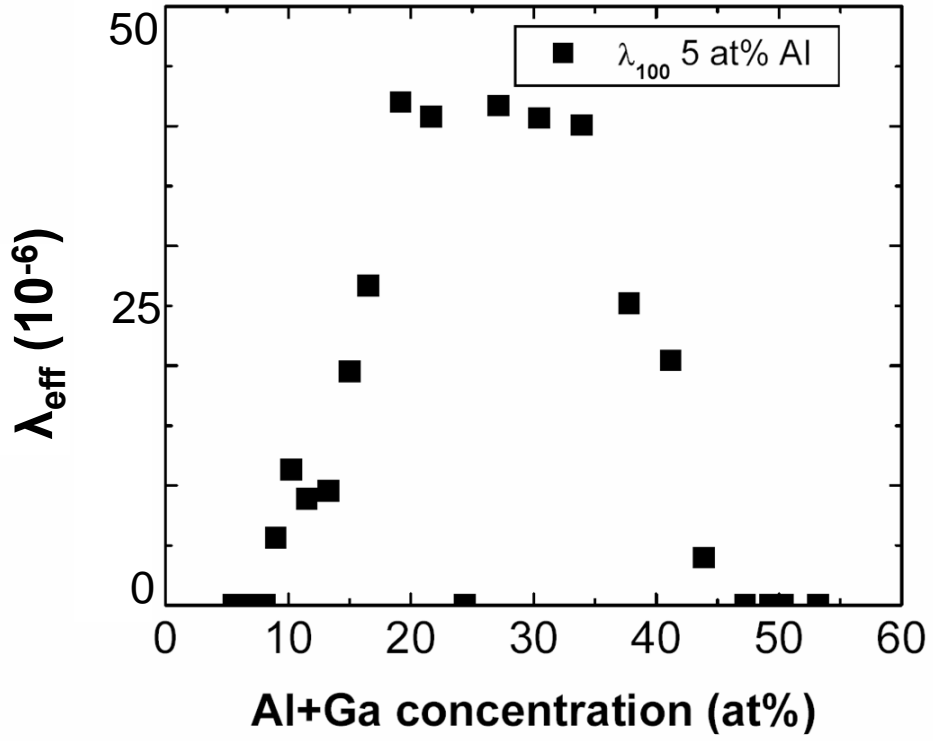


Figure 4.8: The variation of magnetostriction λ_{eff} as a function of the sum of Ga and Al concentrations, shows the same general trend as in pure Fe-Ga. The broadness of the peak is likely due to composition gradients across the cantilever.

$$\lambda_{eff} = \frac{1}{5}\lambda_{100} + \frac{4}{5}\lambda_{111}$$

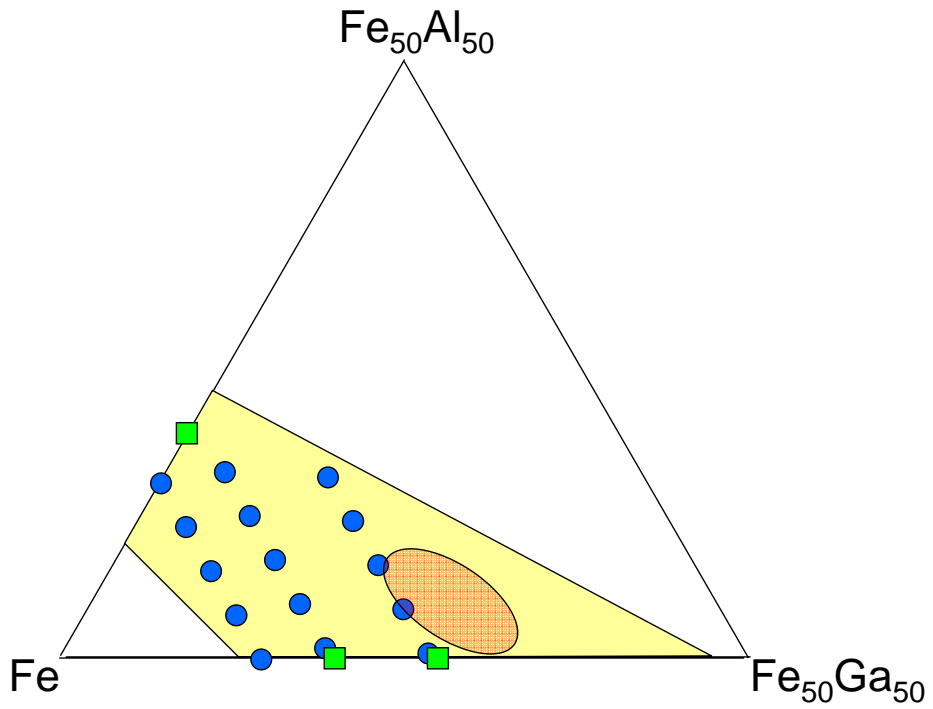


Figure 4.9: Schematic representation of the large magnetostriction region in Fe-Ga-Al. The yellow region is the area of large magnetostriction in the system, the blue circles bulk data taken from [5, 6], the green boxes represent the maxima in magnetostriction found in bulk binary Fe-Ga and Fe-Al, and the orange oval indicates the new region with higher Al insensitivity found in this thesis.

to decrease the price of the alloy and increase its workability.

4.6 Conclusion

The effect of ternary additions of Pd and Al to Fe-Ga has been investigated via combinatorial synthesis and a high-throughput magnetostriction screening technique. It was found that Pd shifts the onset of the formation of the ordered phases to lower Ga contents but did not affect the position of the peak associated with a peak in magneto-elastic coupling. In addition, even 1-3 at% of Pd was found to significantly degrade the magnetostriction of Fe-Ga by a factor of 2, as compared to thin-film studies. On the other hand, the compositional trend of the magnetostriction of Fe-Ga was unaffected by Al. In particular, the magnetostriction in the region of the binary composition $\text{Fe}_{70}\text{Ga}_{30}$ was found to be insensitive to Al additions up to $x = 10$. The ability to reduce Ga content while maintaining a comparable magnetostriction is significant, as it lowers the overall price of the alloy and could help reduce embrittlement. Bulk studies are being undertaken to confirm these results and to investigate the mechanical properties of these new materials.

Chapter 5

Characterization of High-Temperature Phases in Fe-Pd-Ga

5.1 Introduction

This chapter discusses efforts to capture high-temperature phases in thin-film Fe-Ga-Pd alloys using a high-vacuum annealing/quenching furnace. The chapter begins with a brief introduction to the ferromagnetic shape memory alloy (FSMA) $\text{Fe}_{70}\text{Pd}_{30}$ and the motivation for adding Ga. A proof of concept experiment indicating the ability of the annealing/quenching furnace to capture the quenched FSMA phase of binary $\text{Fe}_{70}\text{Pd}_{30}$ is then described. Finally, the effect of the addition of Ga to the magnetic properties of Fe-Pd is discussed.

5.2 Ferromagnetic Shape Memory Alloy Fe₇₀Pd₃₀

It is well known that the Fe-Pd system contains a region of FSMAs for compounds containing about 30 at% Pd. Fe-Pd is known to undergo up to two martensitic phase transitions depending on the composition of the sample[74]. From the high-temperature phase the system can transform from an fcc phase to either a fct phase or bct phase. As the temperature is further lowered there exists the possibility of the fct phase transforming into the bct phase. A final possibility, for compositions much larger than 29.7 at%, is single transition from fcc to fct. A peculiarity of this system is the the fcc to fct transformation, which is highly reversible. Contrarily the fct or fcc to bct transformation is irreversible. The reversible fcc to fct transition occurs right at about 293 K, and the material is ferromagnetic at room temperature

In order to capture the fcc phase, samples must be annealed in solid-solution (generally at 1173 K) and then quenched in ice water to preserve the solid-solution phase. If this is not done properly, the phase diagram (Figure 5.1), shows that the alloy will begin to decompose at 873 K into a mixture of α -Fe and fct equiatomic FePd and will no longer exhibit martensitic transformations. Thus, to successfully produce FSMAs in the Fe-Pd sample, successful quenching of the sample is imperative.

5.3 Binary Fe-Pd

To demonstrate the ability of our high vacuum annealing/quenching furnace to quench an entire 3" composition-spread sample, an experiment was first carried out on a binary Fe-Pd composition-spread sample. There have been several previous

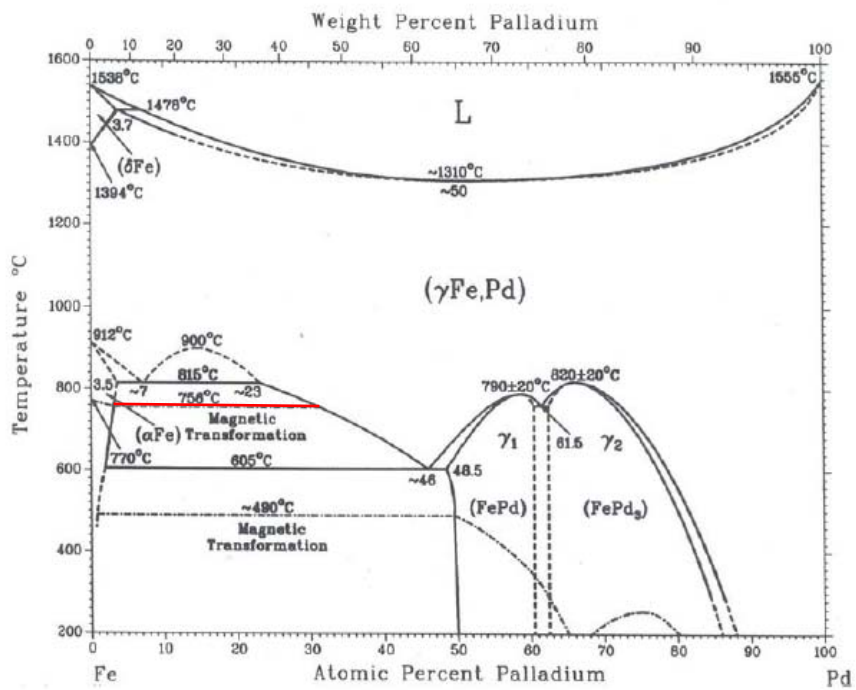


Figure 5.1: Phase diagram of Fe-Pd. From [3]. The red line emphasizes the magnetic region in the high-temperature part of the phase diagram.

reports of synthesizing and quenching single composition thin-film samples of Fe-Pd [75, 76]. However, there have been no reports on quenching entire composition-spread samples.

5.3.1 Sample Preparation

The samples were prepared in our UHV sputtering chamber. The base pressure was 5×10^{-8} Torr, and the samples were deposited at a pressure of 4.6×10^{-3} Torr in argon. Both cantilever libraries and gridded samples were produced, the former to search for the presence of thermally induced structural transitions, the latter for X-ray diffraction studies to confirm the capture of the high-temperature phase. DC power supplies were used for both sets of samples with the Fe and Pd powers being 70 and 30 Watts, respectively. The nominal target-substrate distance was 12.5 cm, and the depositions were conducted for 1.5 hours yielding a total film thickness of $0.6 \mu\text{m}$. Two sets of samples were made to compare the differences between slow-cooled samples and quenched samples.

After deposition the samples were placed into the high-vacuum annealing/quenching furnace for heat treatment. The chamber was evacuated to 2×10^{-8} Torr, and then the samples were annealed for 1 hour at 1173 K. During annealing, the cryopump was open to the furnace chamber, ensuring that the pressure of the system never exceeded 10^{-5} Torr. After annealing, the samples were either allowed to air cool to room temperature or quenched by inserting the entire chamber into a bucket of ice water.

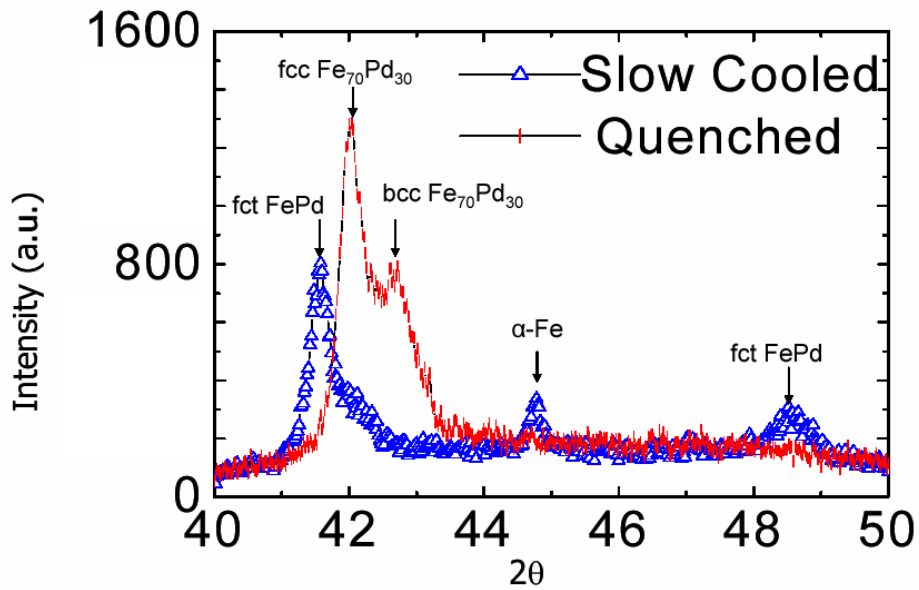


Figure 5.2: A comparison of θ - 2θ XRD scans from the quenched and slow-cooled $\text{Fe}_{70}\text{Pd}_{30}$ samples. Here the presence of phase decomposition to α -Fe and FePd is clearly seen in the slow-cooled sample. The quenched samples retains the high-temperature fcc/bcc phase.

5.3.2 Structural Properties

Figure 5.2 compares the XRD spectra for two samples of nominally $\text{Fe}_{70}\text{Pd}_{30}$, which were either slow-cooled or quenched. From the spectra, it is clear that the slow-cooled sample underwent decomposition into α -Fe and equiatomic fct Fe-Pd. The quenched sample meanwhile clearly maintained its high-temperature fcc/bcc phase as dictated by the composition.

To confirm the presence of thermally induced martensitic transitions, the deflection of the cantilevers in the cantilever library was monitored as a function of temperature[37]. The technique used to screen for martensites relies on the sim-

ple principle that the individual cantilevers behave as concave mirrors. During a transition, stress-induced actuation of a cantilever results in a sudden change in the radius of curvature of the “mirror.” The image reflected from the cantilever is very sensitive to the concavity of the cantilever. By monitoring the change in the image as a function of temperature, we can readily discern composition regions undergoing a transformation. The composition of transforming cantilevers was mapped via WDS. The measurement confirms that for thin-film cantilevers composed of $\text{Fe}_{70}\text{Pd}_{30}$, a martensitic transition is present.

5.4 Ternary Fe-Pd-Ga Composition-Spreads

A true test of the quenching chamber’s ability to capture high-temperature phases is to quench an entire ternary system. In addition, the composition range over which Fe-Pd exhibits martensitic transitions is quite narrow so it is of interest to add a ternary element that could increase the size of this region. As an example system Fe-Pd-Ga was chosen. Both the Fe-Ga and Fe-Pd binary edges of this ternary system exhibit rich phase diagrams and have properties that depend strongly on heat treatments. Due to the difference in structure between Fe-Pd (fcc) and Fe-Ga (bcc) it was anticipated that the two systems would be insoluble in one another and could exhibit a mixed-phase region of FSMA and magnetostrictive materials.

5.4.1 Sample Preparation

The samples were deposited in our UHV sputtering chamber. The base pressure was 5×10^{-8} Torr, and the samples were deposited at a pressure of 4.6×10^{-3} Torr

in argon. Gridded samples were deposited for scanning SQUID microscopy and MOKE studies while cantilever libraries were made to check for magnetostriction and thermally induced structural transitions. The deposition condition of these samples is identical to Fe-Pd-Ga samples described in Chapter 4. The Fe and Fe₂Ga₃ targets were sputtered at 75 and 40 Watts DC, respectively, while Pd was RF sputtered at 5 Watts. The depositions in this study were done with the substrate at room temperature.

After deposition the samples were placed in the quenching furnace for heat treatments. Due to the high vapor pressure of Ga several different annealing conditions were done to minimize Ga loss during annealing. Figure 5.3 shows the region covered by deposition at room temperature as well as the effect of two different post-deposition annealing conditions on the spreads. Both samples were annealed at 1173 K.

In Figure 5.3 (a), it is seen that a large portion of the Fe corner of the phase diagram is obtained with the current deposition condition. Figure 5.3 (b) shows the result of annealing with the cryopump open to the chamber throughout the heat treatment. This sample showed after 1 hour of this type of anneal almost all of the Ga had left the system, in essence leaving a Ga-doped Fe-Pd binary. In an effort to trap more Ga in the system, after pumping down to the base pressure of the chamber, 10^{-8} Torr, the system was backfilled with 1 atm of He prior to annealing. Figure 5.3 (c) shows that with this procedure, much more of the ternary phase diagram was captured.

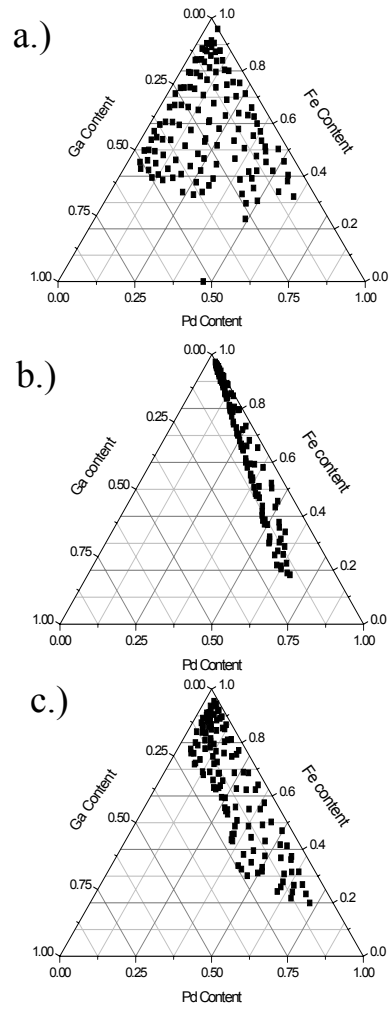


Figure 5.3: The coverage of composition in Fe-Pd-Ga composition spreads as a function of different heat treatments. (a) shows WDS data of an as-deposited sample. (b) and (c) show the effect of annealing at 900°C in vacuum and in 1 atm of He, respectively. By increasing the back-pressure more Ga is trapped.

5.4.2 Magnetic Properties of Fe-Pd-Ga

The magnetic-flux-density mapping of the Fe-Pd-Ga composition-spread wafers was obtained via scanning SQUID microscopy. AFM studies of the surface in the Ga-rich region of the phase diagram show a highly discontinuous film surface, which makes quantitative calculation of magnetization from scanning SQUID microscopy difficult. Therefore this study focused on the changes in magnetic flux density along the Fe-Pd binary edge. Magnetic flux density is proportional to the remnant magnetization of the sample [49].

From Figure 5.4, one can see that the regions containing magnetic materials cover a large portion of the mapped composition. The magnetic region extends from almost pure Fe, which is strongly magnetic, to around $\text{Fe}_{63}\text{Pd}_{37}$, where the phase diagram indicates that magnetism sharply declines.

The saturation-field mapping obtained from MOKE is plotted on the ternary phase diagram in Figure 5.5. The values of the saturation field, for compounds on the binary Fe-Pd line, are comparable to the values of saturation field obtained for pure high-temperature $\text{Fe}_{70}\text{Pd}_{30}$ [77]. In addition, the region that exhibits magnetism matches well with the known magnetic region in the Fe-Pd binary phase diagram at high temperatures.

To illustrate that the magnetic properties observed reflect those of a quenched Fe-Pd binary system, the MOKE results and the binary Fe-Pd phase diagram are plotted together in Figure 5.6. According to the phase diagram, there are two independent magnetic regions, one corresponding to a high-temperature solid-solution of Fe and Pd and a second which is a mixture of α -Fe and FePd. The high-temperature phase remains magnetic until approximately 33 at% Pd, while the low-temperature phase exhibits magnetism extending to 60 at% Pd. From a

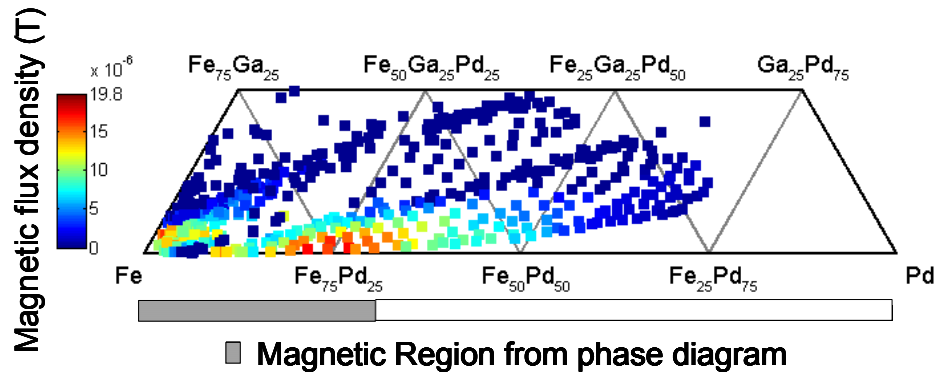


Figure 5.4: A magnetic-flux-density mapping of the ternary phase diagram obtained through scanning SQUID microscopy. Here, the magnetic flux density is related to the remnant magnetization of each sample. The shaded bar beneath the graph indicates the magnetic region of the known high-temperature phase diagram of binary Fe-Pd. (Figure 5.1). There is good correlation between the areas that exhibit high magnetization in the ternary and the known magnetic region of binary Fe-Pd. This spread was annealed at 900° for 1 h. in 1 atm of He and then quenched.

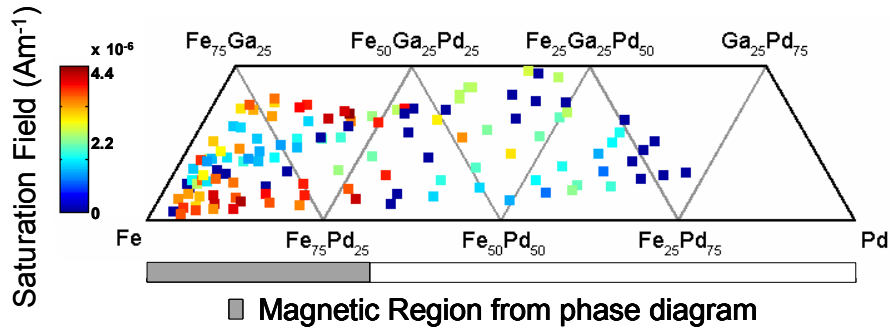


Figure 5.5: A mapping of saturation field plotted on the ternary phase diagram obtained through MOKE measurements. The shaded bar beneath the graph indicates the region of the known high-temperature phase diagram of Fe-Pd that is magnetic. There is good correlation between the areas that exhibit high saturation field in the ternary and the magnetic region of binary Fe-Pd.

comparison of Figure 5.4 and Figure 5.5 with the phase diagram, it is clear that the magnetic regions mapped very closely resemble those of the high-temperature phase. This indicates that we have been able to successfully obtain the quenched high-temperature phases in the composition-spread wafers.

5.5 Conclusion

In summary, an ultra high-vacuum quenching furnace, which allows the trapping of high-temperature phases in ternary composition-spread libraries deposited on 3" Si wafers, has been developed. XRD and thermal actuation studies on binary Fe₇₀Pd₃₀ confirm the ability of the quenching system to capture metastable high-temperature phases. The high-temperature magnetic properties of these systems

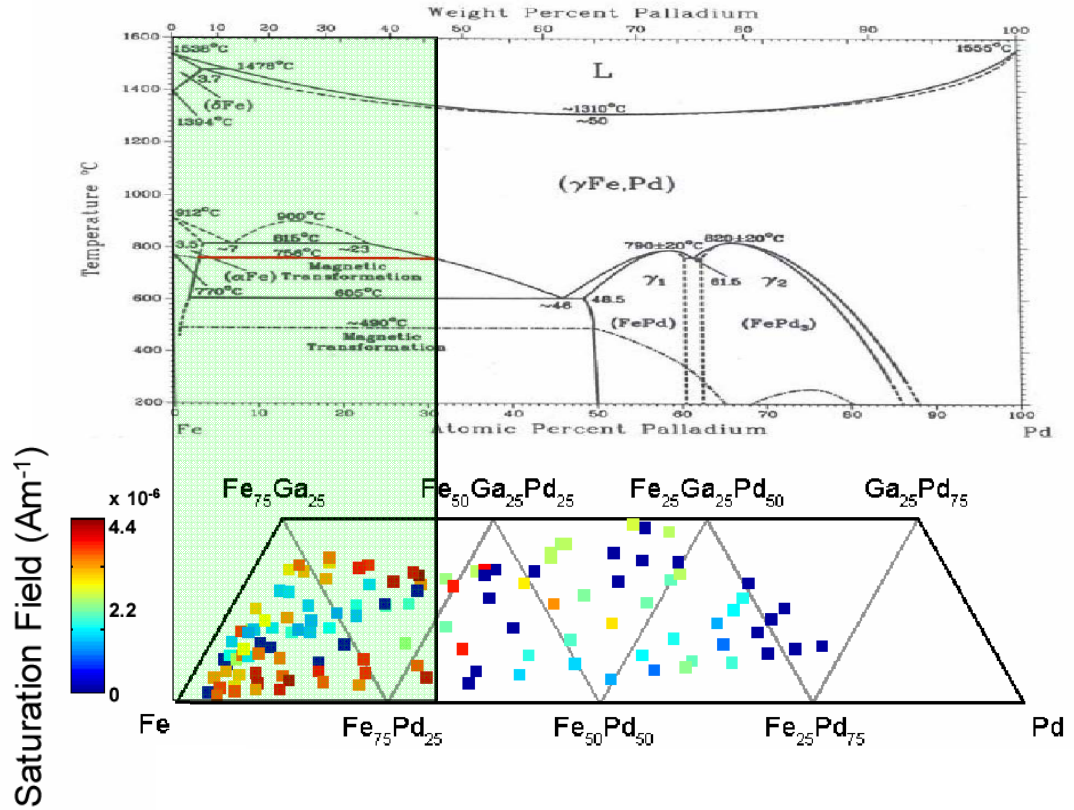


Figure 5.6: A comparison of the high temperature magnetic region from [3] and magnetic region shown by MOKE studies on the quenched Fe-Pd-Ga thin-film samples.

are mapped through a combination of scanning SQUID microscopy and a high-throughput MOKE system. It was observed that both the saturation field and the remnant magnetization along the Fe-Pd binary edge correlates well with magnetic regions of the the known phase diagram. No martensitic transitions were observed in the ternary Fe-Pd-Ga samples. This was most likely due to the discontinuity of the films in the high Ga region, and the tendency for Ga to stabilize Fe in a bcc crystal structure.

Chapter 6

Magnetolectric Scanning Probe Microscope

This chapter presents an application of magnetostrictive materials as components of magnetolectric sensors for the detection of minute magnetic fields. First, a brief overview of the state of the art in magnetic imaging techniques is given, followed by a discussion of magnetolectric laminates, their formation, properties, and benefits. A prototype scanning AC magnetometer incorporating a magnetolectric laminate is then introduced. Results from scans of the in-plane and out-of-plane magnetic field using the microscope are discussed.

6.1 Scanning Magnetic Probe Microscopes

Scanning magnetic-probe microscopes using high-sensitivity magnetometers are vital for applications ranging from nondestructive evaluation of integrated circuits to the investigation of magnetic materials. Common to many scanning magnetic-probe microscopes is the trade-off between spatial resolution, sensitivity, and oper-

ating conditions. Magnetic-force microscopy, for instance, has a spatial resolution as high as 10 nm at room temperature [7, 78]. It measures field gradients instead of actual fields, and its typical reported field sensitivity is 10^{-4} T [7]. Recently, scanning Hall probe microscopes have shown spatial resolutions as high as 50 nm with field sensitivities down to 10^{-8} T at 77 K [7, 79]. SQUIDs are known to be the highest sensitivity magnetometers, capable of detecting single-flux quanta, and they have been incorporated as sensors in scanning microscopes. In Chapter 5 of this thesis, scanning SQUID microscopy has been used to map out magnetic regions in ternary composition-spread samples. For low-temperature scanning SQUID microscopes using Nb-based SQUIDS, the maximal demonstrated field sensitivity is 2×10^{-14} T/Hz $^{\frac{1}{2}}$ [8]. The spatial resolution of this type of scanning SQUID microscope is limited only by the size of the device, but measurements must be carried out at cryogenic temperatures [8]. In room-temperature scanning SQUID microscopes, a sapphire window is placed between the cryogenically cooled SQUID sensor and the room temperature sample. This space between the sample and the sensor limits the maximum obtainable spatial resolution to 20 μ m [8, 7]. The field sensitivity is not strongly affected by the separation and has been shown to be $\sim 10^{-14}$ T/Hz $^{\frac{1}{2}}$ [8]. Tunneling magnetoresistance sensors have also been implemented as sensors for scanning probes and have been demonstrated to have spatial resolutions of 0.1 μ m and field sensitivities of 10^{-9} T. A summary of the current state of the art in scanning magnetometers taken from [7] by S. J. Bending together with results and discussion from this chapter is presented in Figure 6.1.

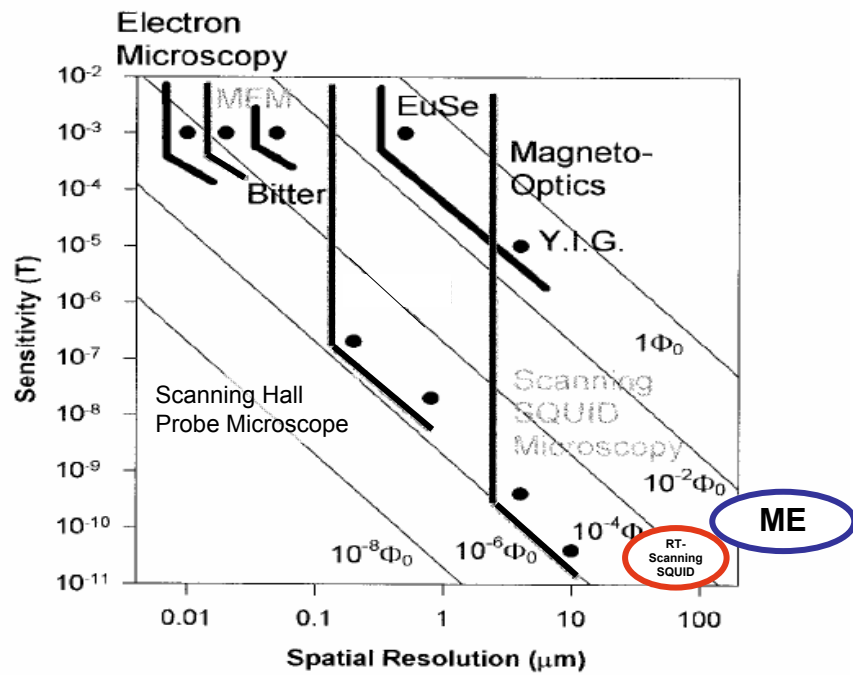


Figure 6.1: A summary of various scanning-probe magnetometers and their typical spatial resolution and sensitivities. The figure was taken from [7]. The characteristics of the prototype magnetoelectric scanning-probe magnetometer and those of a room temperature scanning SQUID microscope have been added to the figure for comparison [8, 9].

6.2 Magnetolectric Laminates

Magnetolectric (ME) materials are materials systems that simultaneously display ferromagnetism and ferroelectricity. One attractive property of ME materials is the ability to sense magnetic fields and report their value in voltage. To do this, the magnetic and ferroelectric responses must be coupled to one another. ME materials can be divided into natural magnetolectrics or multiferroics (BiFeO_3 , BiMnO_3) and artificial magnetolectrics, known as composite magnetolectrics materials. Composite magnetolectrics can be further divided into nano-composites, where the constituent phases are present as nano-phased mixture[22, 80], or laminates, where the ferroic-phases are bulk sheets that have been adhered together[81, 82]. The latter have been the subject of numerous investigations over the past few years due to their ability to detect extremely small magnetic fields[81, 82, 83, 84].

A simple ME laminate structure typically contains two magnetostrictive layers that have been bonded to opposite sides of a piezoelectric layer, as schematically shown in Figure 6.2. To maximize field sensitivity, it is vital that the bonding be carried out in such a way as to ensure the layers are elastically coupled. When a magnetic field is applied to the laminate the strain from the magnetostrictive layers is transferred as a stress to the piezoelectric layer. The resulting strain that this causes in the piezoelectric layer produces a voltage. The highest AC field sensitivity reported to date is $10^{-15} \text{ T/Hz}^{\frac{1}{2}}$ at the mechanical resonance of the sensor (10^5 Hz)[82]. These devices are inexpensive to make and operate at room temperature.

In an effort to maximize sensitivity, typically Terfenol-D or Galfenol are chosen as the magnetostrictive material because of their large magnetostriction. An

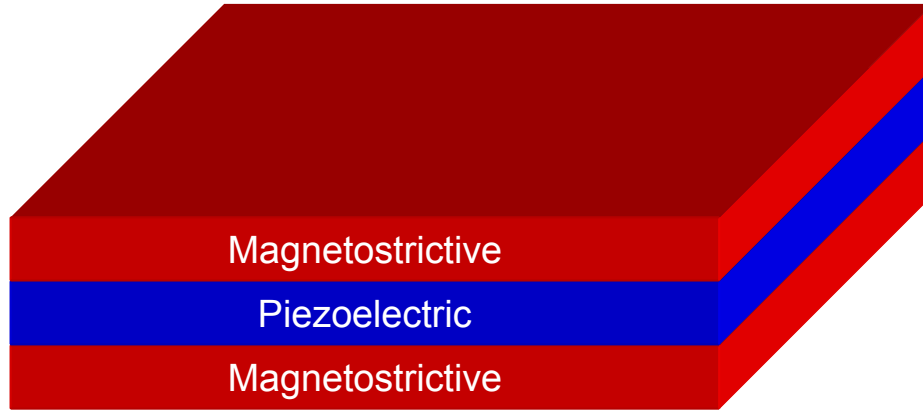


Figure 6.2: A schematic of an ME laminate device structure.

alternative method to maximize sensitivity is to choose a material with a modest magnetostriction but a very large magnetic permeability. This is because the ME response of a laminate is directly related to its magnetic permeability. This can be seen from the following. The strength of the ME coupling is given by the ME coefficient $\alpha^E = \frac{\delta E}{\delta H}$, which expresses the induced electric field E due to a change in magnetic field H . Because the electric field is the transduced piezovoltage, α^E can be rewritten in terms of the magnetostrictive susceptibility:

$$\alpha^E = \frac{\delta E}{\delta H} = \frac{\delta E}{\delta \varepsilon} \frac{\delta \varepsilon}{\delta H} = \frac{\delta E}{\delta \varepsilon} \frac{\delta \lambda}{\delta H} \quad (6.1)$$

where ε is the transduced strain and is equal to the magnetostriction λ assuming ideal coupling between the layers. The magnetostrictive permeability $\frac{\delta \lambda}{\delta H}$ of a material is in turn related to its magnetic permeability χ_M by

$$\frac{\delta \lambda}{\delta H} = \frac{\delta M}{\delta H} \frac{\delta \lambda}{\delta M} = \chi_M \frac{\delta \lambda}{\delta M}. \quad (6.2)$$

This suggests that ME devices incorporating high-permeability magnetic materials can exhibit ME coefficients comparable to those using Terfenol-D by boosting $\frac{\delta \lambda}{\delta H}$ through a large χ_M . An additional benefit of using such materials for ME

devices is the low DC biasing field necessary for optimal performance. ME devices function best as AC-field detectors. To operate the device for AC-field detection, it is necessary to apply a biasing DC field to ensure that the device is operating at the peak of its magnetic permeability and thus its peak ME sensitivity. From an applications perspective it would be beneficial to operate at as small a DC bias as possible and this makes pursuing sensors with large permeabilities very attractive. There has been some limited work done on ME devices incorporating high permeability materials, but there have not been any previous attempts to incorporate them as sensors in scanning magnetic probes[81, 85].

6.2.1 Metglas/PVDF Tri-layer Laminate

Our magnetoelectric sensors were fabricated using commercially available Metglas, a metallic glass, pieces and polyvinylidene fluoride (PVDF) samples. Metglas was chosen as the magnetostrictive material, despite its relatively low magnetostriction of 35 ppm, due to its relative permeability of 400,000 at a field of less than 1 Oe. Terfenol-D has a magnetostriction of 1500 ppm, a factor of 42 higher than Metglas, but its permeability is 10 which is a factor of 40,000 less than that of Metglas. The Metglas was obtained from Metglas, Inc. and was a 23- μm -thick sheet that came in 100-yard rolls. The sheets were field annealed in the rolling direction. The effect of the field anneal is that the field annealed direction has a magnetostriction of 35 ppm while perpendicular to that direction the magnetostriction is less than 1 ppm. The rolls were cut into rectangles of varying dimensions from 10 mm to 1 mm along either direction by electrical discharge machining (EDM), to avoid introducing stresses to the samples. The PVDF was acquired from Measurement Specialties, Inc. The PVDF came in 11.5" x 8" x 100 μm sheets that had been

electrically poled in the thickness direction. We cut the PVDF into 6 mm x 6 mm squares and then bonded it between two pieces of Metglas with a conductive epoxy. In order to minimize the distance between the Metglas and the specimens to be scanned later, care was taken to bond the Metglas on the edge of the PVDF.

Each sensor was calibrated for magnetic field sensitivity with a home-made calibration system. We applied a constant AC bias field to the sensor while a DC field was slowly swept up to 1 kOe, and the ME signal was measured. Both fields were applied along the field annealing direction of the Metglas, while the ME voltage was measured across the thickness of the device. The ME signal was detected using a lock-in amplifier. The response of the sensor was tested for frequency f with $200 \text{ Hz} \leq f \leq 8 \text{ kHz}$ and for AC amplitudes from 20 Oe to 10^{-5} Oe.

In ME measurements, there are two possible sources of contribution to the measured signal, the ME voltage and an inductive signal. The inductive signal arises from the crosstalk between the applied AC magnetic field and the wires used to make electrical connection with the device. Before effective ME measurements can be made, it is necessary to minimize the inductive contribution by using shielded cables. Once the inductive signal has been minimized it can be removed from the ME signal through use of the property that the ME signal and inductive signal are $\pi/2$ out of phase. An important check to ensure the inductive signal has been removed is to measure the ME signal as a function of frequency. The true ME signal should be frequency independent at low frequency, except at the physical resonance of the device, but the inductive signal should depend on frequency as f .

The ME signal measured for this device was found to be independent of frequency in the range studied here thereby indicating that no inductive signal was

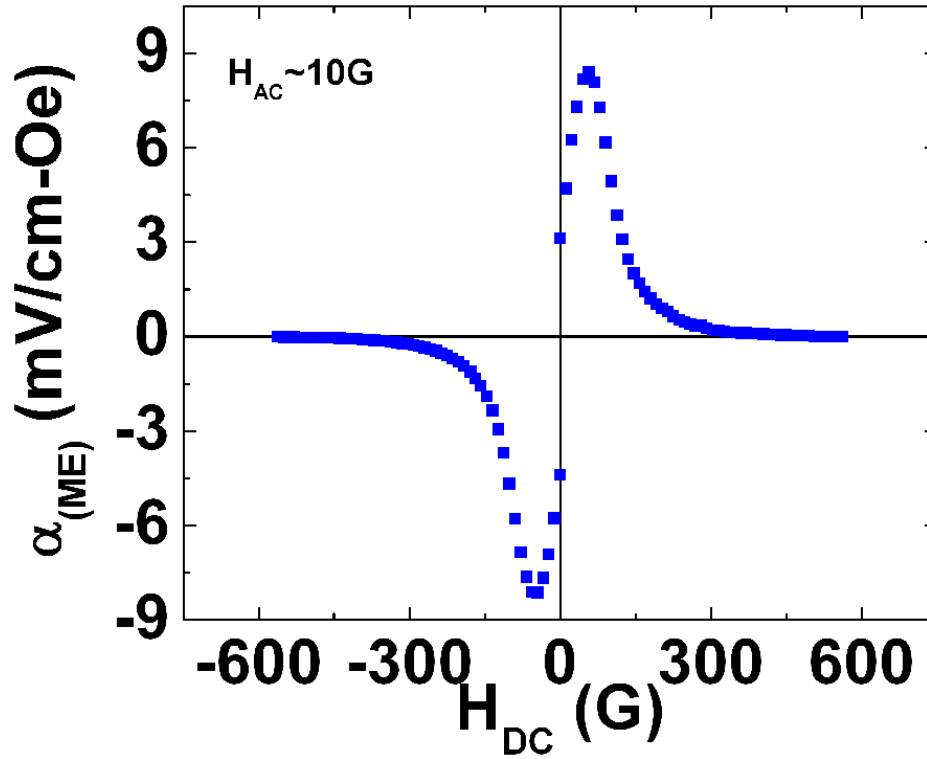


Figure 6.3: The ME signal(α_{ME}) versus applied DC field of a device at a frequency of 259 Hz and an AC field amplitude of 10 Oe. The maximum in ME coupling is found at 70 Oe. The ME coefficient is $8.6 \pm .1$ mV/(cmOe) at that bias.

detected. An ME signal vs. applied DC field curve is shown in Figure 6.3, which was taken at 259 Hz with an AC field of 10 Oe. The peak in the ME signal is seen to be 6 mV at an applied field of 70 Oe. This corresponds to a ME coefficient of 8.6 ± 0.1 mV/(cm Oe).

To quantify the AC field sensitivity the maximum from each ME signal vs. applied DC field curve was taken for each AC field used. The plot in Figure 6.4 shows that the ME response is linear with respect to AC field. The AC sensitivity, taken as the slope of this line, is 467 ± 3 μ V/Oe. This value is used later to

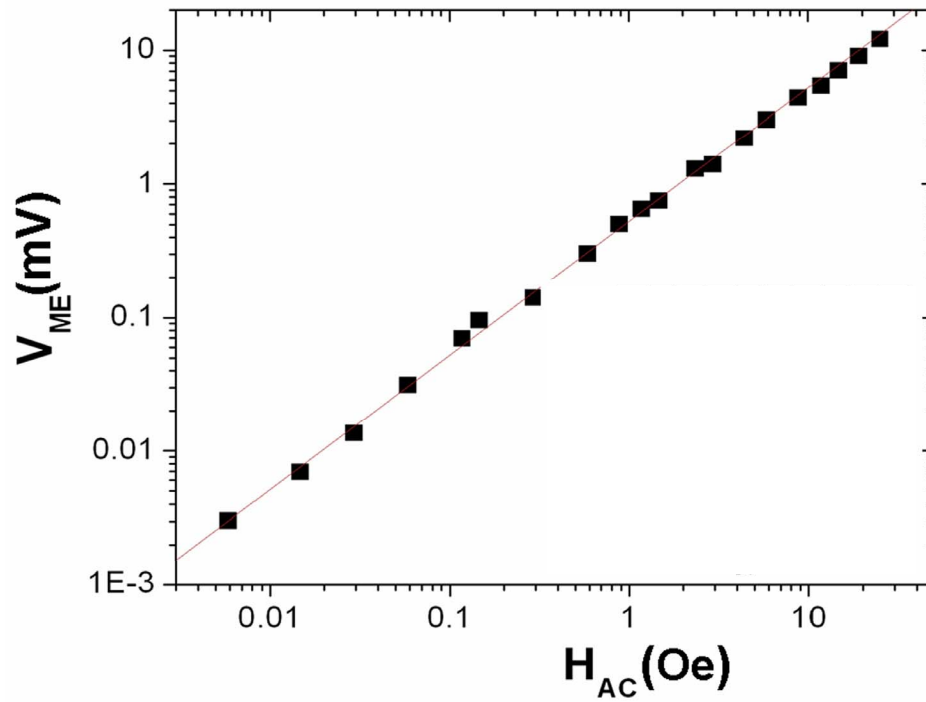


Figure 6.4: The ME signal versus AC field at a frequency of 259 Hz. The AC sensitivity is taken as the slope of this line and is found to be $467 \pm 3 \mu\text{V}/\text{Oe}$.

calculate the field experienced by the sensor as it scans over current-bearing wires.

The effect of the sensor size on the ME signal was investigated for several sensor dimensions. The results of this study show that the ME signal decreases linearly with decreasing sensor area. Since the voltage generated across the PVDF is not expected to be affected by the area of the PVDF, it is proposed that difference seen is related to an inhomogeneity of the bonding across the sample. This would result in a non-homogeneous strain in the PVDF and could affect its sensitivity as the device is scaled down. For this reason all subsequent scans were done with an active device dimension of 2 mm x 4 mm.

6.3 Magnetolectric Microscope

To assess the ability of the ME laminate as a sensor for a scanning probe magnetometer, the ME sensor was mounted on an xyz stage and scanned over AC current-bearing loops. In this setup, a constant DC field bias was applied either by a Helmholtz coil or a NdFeB magnet in the field annealed direction of the Metglas. An AC power supply driven by a function generator was used to generate the AC current in the wire while the current in the ring was monitored by an ammeter. The current bearing ring was fabricated with a $15\text{-}\mu\text{m}$ diameter Cu wire and was mounted on a glass scanning stage to minimize background noise. The scans and data acquisition were automated through the use of a Labview program.

Two sensor/wire geometries were considered and are presented in Figure 6.5. In the first geometry, hereafter referred to as B_x , the field-annealed direction of the Metglas was placed parallel to the plane containing a 1.8 mm diameter current bearing ring. This configuration should be sensitive only to the in-plane components of the magnetic field produced. In the other geometry, hereafter known as B_z , the field-annealed direction of the Metglas was oriented perpendicular to the plane of a 2-mm-diameter current-bearing ring. This orientation should make the device sensitive only to the out-of-plane component of the magnetic field. The DC bias field is applied in the respective field annealed direction for both types of scans.

6.3.1 Scans of B_x

In order to initially test the feasibility of using ME devices as sensors for scanning-probe microscopes, a series of scans were performed measuring the in-plane field

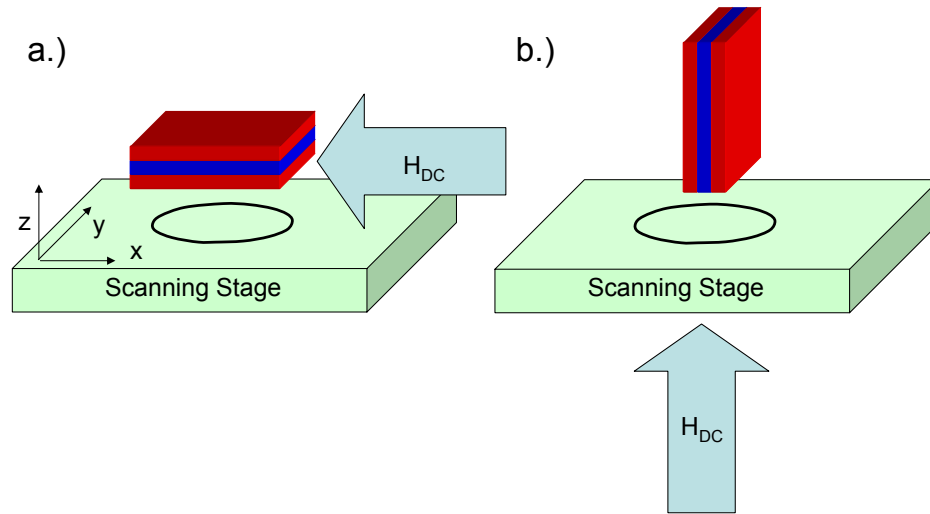


Figure 6.5: Schematics of the two scanning geometries considered here. (a) illustrates a geometry where the field-annealed direction of the Metglas is oriented parallel to the scanning direction. Here the sensor is only sensitive to B_x . (b) illustrates a geometry where the field-annealed direction is oriented perpendicular to the plan of the current-bearing ring and should only be sensitive to B_z .

produced by a current bearing ring. The device dimension in the direction of the scan was 4 mm. During this scan the sensor/ring distance was maintained at $50 \mu\text{m}$, and the ME signal was recorded every $50 \mu\text{m}$. The AC current was fixed at 10 mA at a frequency of 5 kHz. Due to the change in geometry of the measurement system, new sources of inductive signal could appear, and there may also be other spurious sources of signal, which are not understood at this time. To eliminate these signals, which depend strongly on position during scans, two separate scans were done. The first scan used an applied DC field bias of 70 Oe and contained a convolution of ME, inductive, and spurious signals. The second scan used applied DC bias of 400 Oe and contained only the inductive and spurious portions of the signal. The two scans were then subtracted to yield a plot with only the ME signal.

To obtain these scans the sensor was scanned in the x direction through the center of the current bearing ring using the geometry shown in Figure 6.5(a). This type of scan will from now on be referred to as a “line scan.” Figure 6.6 shows a representative line scan through the center of a current bearing ring with a diameter of ≈ 1.8 mm. Here, it is clear that the device size is limiting the spatial resolution, as the length of the device in the scanning direction is comparable to the size of the ring. Rather than sharp changes in field at the ring edges, a continuous change in B_x is observed across the ring position. The line profile is thus distorted due to the presence of the sensor itself. An additional factor in the distortion is the permeability of the Metglas, which will be discussed in more detail in the next section. The position of the ring cross-section relative to the recorded ME signal is shown in the figure by the black lines.

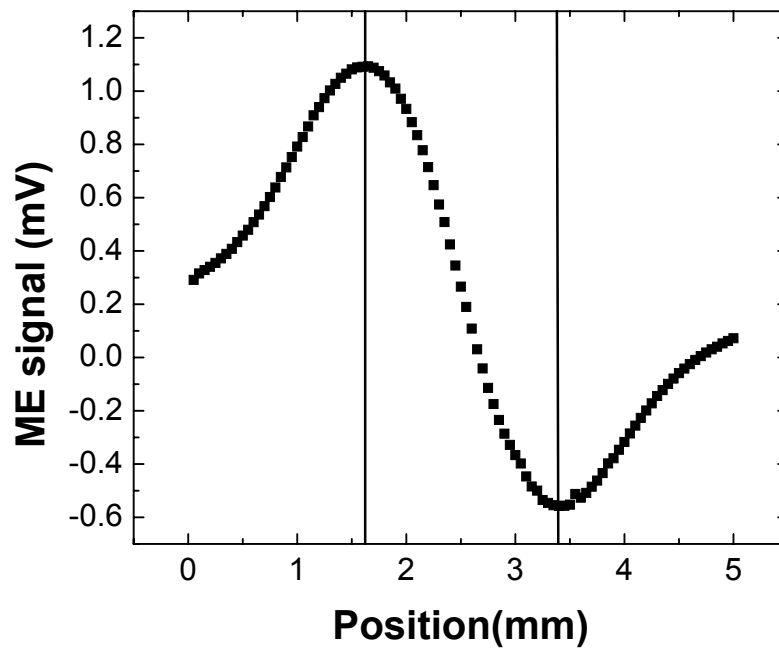


Figure 6.6: A B_x line scan of the in-plane field from a 1.8-mm diameter ring. The position of the wires are denoted by the black lines.

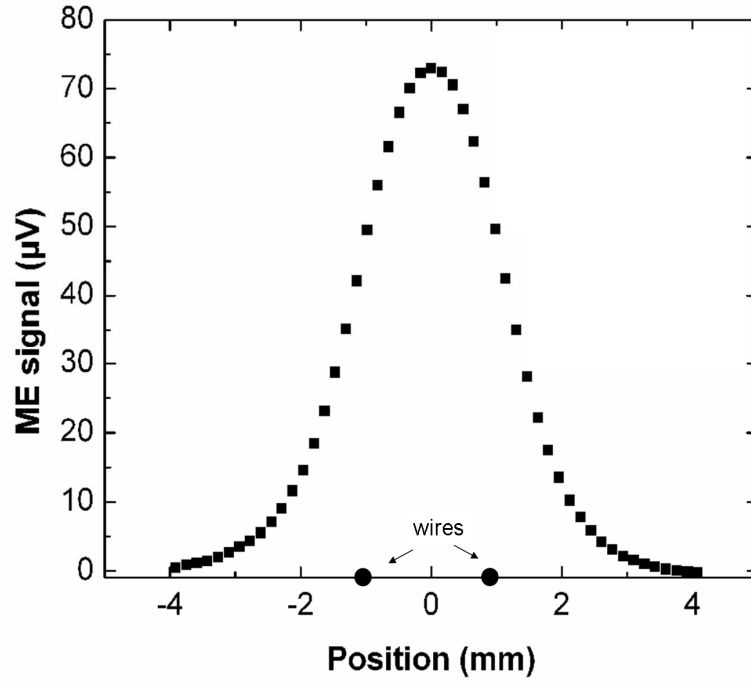


Figure 6.7: A B_z line scan performed over a current bearing ring with an ME sensor. The position of the wires are denoted by the black circles.

6.3.2 Scans of B_z

Scans of B_z were done over a current-bearing ring with a diameter of 2 mm. One such scan is presented in Figure 6.7, where the sensor has been scanned through the center of the ring with the thickness direction perpendicular to the scan direction. During scanning the sensor was maintained at a distance of $50 \mu\text{m}$ from the plane of the ring, while the ME signal was recorded every $150 \mu\text{m}$. The AC current through the ring was fixed at 150 mA, at a frequency of 5 kHz. The DC bias was maintained at 70 Oe during the scan. The position of the ring cross-section relative to the signal is denoted in the figure by the black circles.

Looking closely at the line scan in Figure 6.7, and taking into consideration

the dimensions of our device ($146 \mu\text{m} \times 2 \text{ mm} \times 4 \text{ mm}$) and a scanning height of $50 \mu\text{m}$, the measured magnetic field displays a broadened profile compared to the true B_z field distribution from a ring. The discrepancy results from the fact that (1) in any near-field scanning device the spatial resolution is comparable to the device dimensions, and (2) the magnetic permeability of the Metglas is distorting the magnetic field distribution of the ring over the dimensions of the device.

A finite-element analysis, using the software “femm,” was performed to confirm that the presence of the Metglas alters the field distribution of a current carrying wire and that the extent to which the field redistribution takes place is on the order of the device size [86]. A straight current carrying wire is used instead of a ring, as it simplifies the calculations without significantly changing the interpretation of the field distribution. Therefore, the field redistribution calculated here is analogous to how the field is redistributed as the sensor approaches the ring. The model assumes an infinitely long wire and device (schematically shown in Figure 6.8), and takes a cross-section perpendicular to the wire direction.

To examine the possible effect of the extremely high permeability of the Metglas on B_z , calculations were performed for materials with $\mu = 400,000$ as well as $\mu = 40$. Figure 6.9 (a) and (b) show the results obtained from 2 calculations for a sensor of the same size as our device, positioned $50 \mu\text{m}$ above and $250 \mu\text{m}$ away from a current bearing wire. In Figure 6.9 (a) the calculation has been done with the vertical permeability set to 400,000, similar to that of Metglas, and in Figure 6.9 (b) the calculation uses a vertical permeability of 40, a typical value for ordinary magnetic materials. It can be seen from these Figures that, although there is some difference in the field distribution between the two images, the high value of permeability of the Metglas does not strongly affect the field distribution.

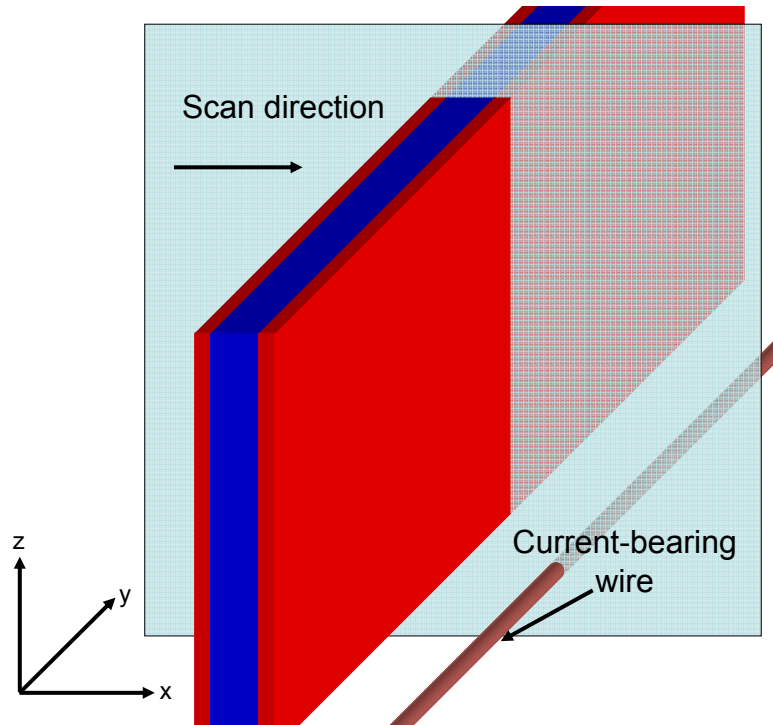


Figure 6.8: A schematic of the approximation used in the finite element calculation for the field distribution. The wire and device are assumed to extend infinitely in the y direction, but have finite dimensions in the x and z directions. The subsequent data will be plotted on the cross-section of the plane and wire illustrated by the plane.

The field inside the device, however, has been greatly altered by the change of the permeability value. This is evidenced by the significantly darker appearance of the active regions of the device and the larger maximal value in the density plot scale bar (Figure 6.9 (a)).

Figure 6.10 (a) and (b) illustrate the identical situation as the previous figure, except the device height has been reduced to $100 \mu\text{m}$ to determine the effect of the device size on the field distribution. Here again, the field distribution of the current bearing wire is altered almost identically for both values of permeability. What is more remarkable, is the the field distribution inside the device is also identical for both cases.

The results of the finite element analysis seem to indicate that what is primarily limiting the spatial resolution is the size of the device. The field redistribution due to the permeability of the Metglas is strongly device-size-dependent and can be minimized with reduced device sizes.

The local field distortion present in near-field scanning magnetic-probe techniques using magnetic sensors is known. For instance, in MFM, the interaction between the magnetic tip and sample surface is known to affect the local field distribution. To accurately and precisely interpret the images, significant post-measurement de-convolution involving detailed knowledge of tip geometry and magnetic properties is required [87, 88]. The active sensing area that needs to be modeled for de-convolution in MFM studies is of the order of the tip dimensions. Similarly, in the present magnetic trilayer device, field redistribution is expected for dimensions comparable to the device size.

One can increase the spatial resolution of the sensor by changing the device

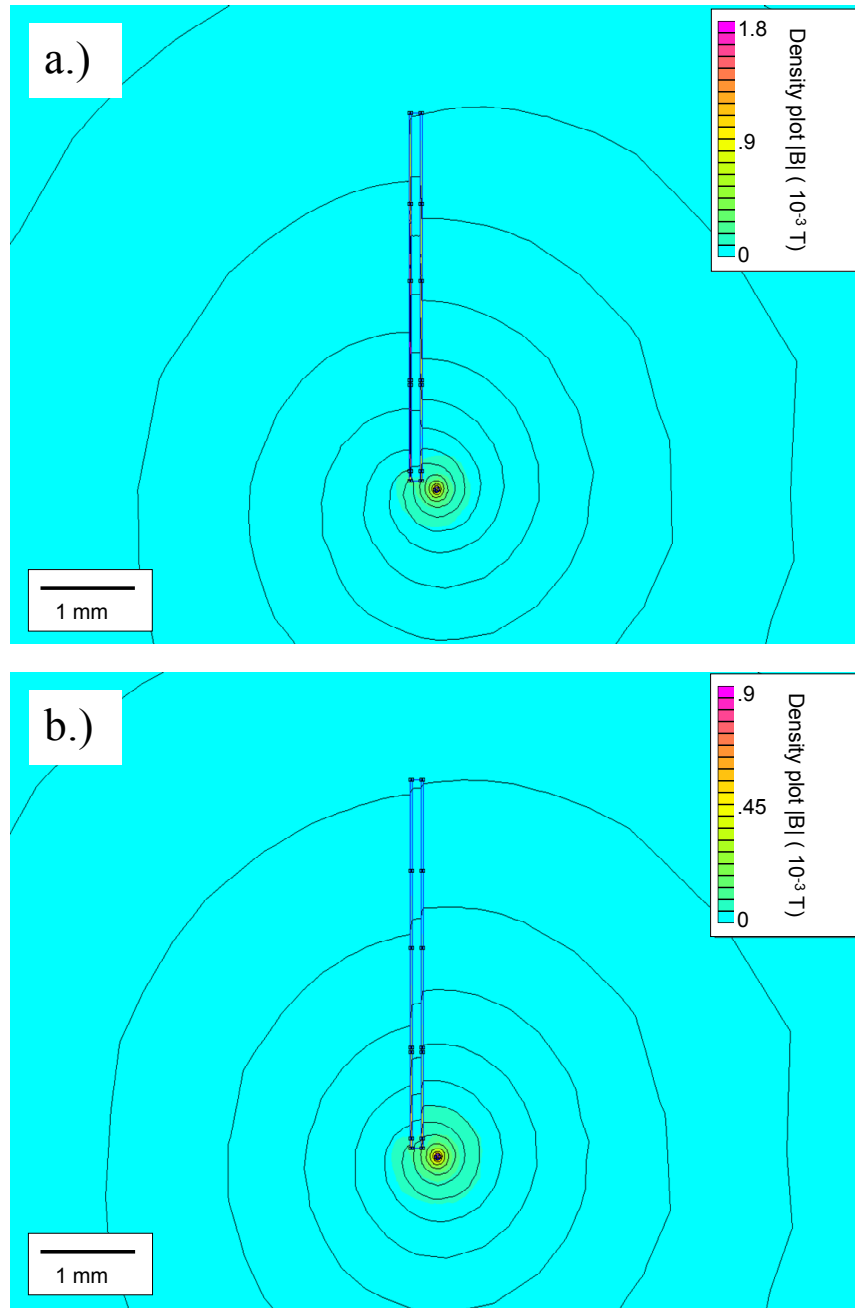


Figure 6.9: Finite-element simulations of the effect of the permeability of a $125 \mu\text{m} \times 4 \text{ mm}$ device on the field distribution of current bearing wire, for the case of a device with a permeability of (a) 400,000 and (b) 40. The field distributions is only slightly changed by the high permeability material.

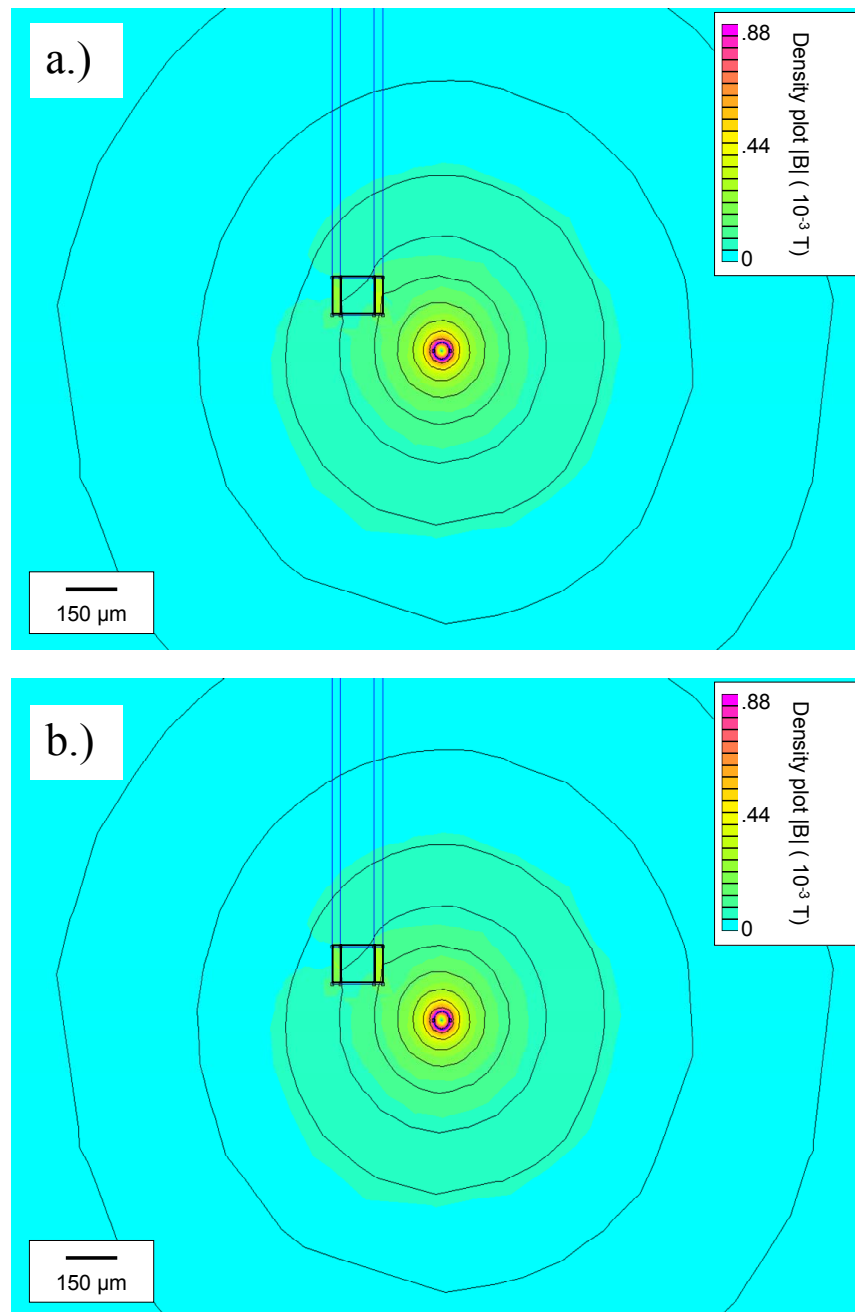


Figure 6.10: Finite-element simulations of the effect of the permeability of a $125 \mu\text{m} \times 100 \mu\text{m}$ device on the field distribution of current bearing wire for the case of a device with a permeability of (a) 400,000 and (b) 40. The field distributions are nearly identical in both cases.

size. This is illustrated in Figure 6.11, where a 2-D scan of the same ring under the same condition as the 1-D scan case is presented. The distortion of the overall shape of the ring “image” to an oval is due to the disparity in the dimensions of the sensor in the plane of the ring, $146\ \mu\text{m}$ through the thickness (x direction) and $2\ \text{mm}$ across the width (y direction), as well as the redistribution of the field lines. Along the thickness direction of the sensor, the length scale over which the signal is detected is comparatively sharper than it is in the other direction and is roughly equal to the ring diameter size. This implies that decreasing the size of the device can contribute to improving the spatial resolution.

To determine the lowest field detectable using the current sensors, a series of line scans were taken, at a constant frequency of $5\ \text{kHz}$, with decreasing AC currents. The results from these scans are shown in Figure 6.12, where the results from the three lowest currents are displayed. It is clear, from this data, that for $150\ \mu\text{A}$ the peak in the signal from the ring is still evident. Before using the AC sensitivity to calculate the field observed by the sensor across the entire sample, it is important to check this value against what is to be expected. At a distance of $1\ \text{mm}$ away from the edge of the ring, according to the Bio-Savart law, the field has only an out-of-plane component. The field experienced by the sensor is calculated to be $1.5 \times 10^{-10}\ \text{T}$. This calculated value is of the same order of magnitude as calculated using the AC sensitivity values obtained earlier ($3 \times 10^{-10}\ \text{T}$), and is considered to be the minimum detectable field with the current sensor. Using the value of the measurement bandwidth of $0.33\ \text{Hz}$, the sensitivity of the present sensor is $\approx 5 \times 10^{-10}\ \text{T}/\text{Hz}^{\frac{1}{2}}$.

We have demonstrated that simple bonded Metglas/PVDF tri-layer devices can

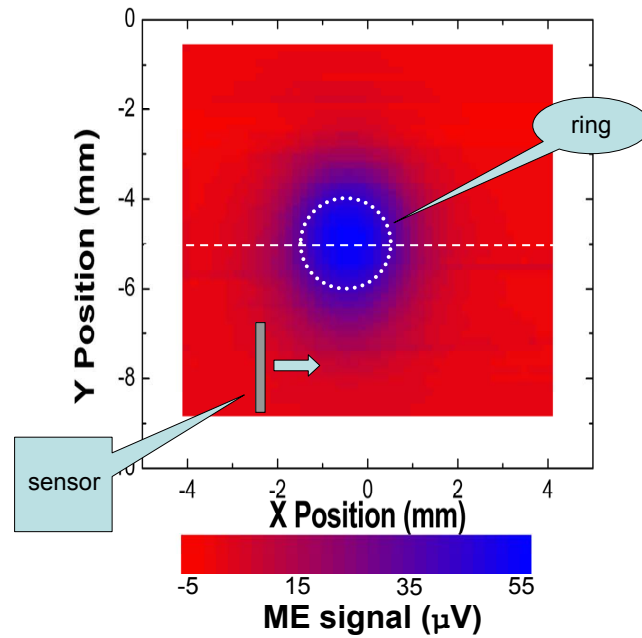


Figure 6.11: The results of a 2-D scan of the current-bearing ring. The scan direction and orientation of the sensor during the scan are schematically illustrated in the lower right hand part of the graph. The ring is represented by the dotted circle, and the dashed line shows the scan path from the previous line scans. Here a clear elongation of the ring is observed in the direction of the sensor's largest dimension.

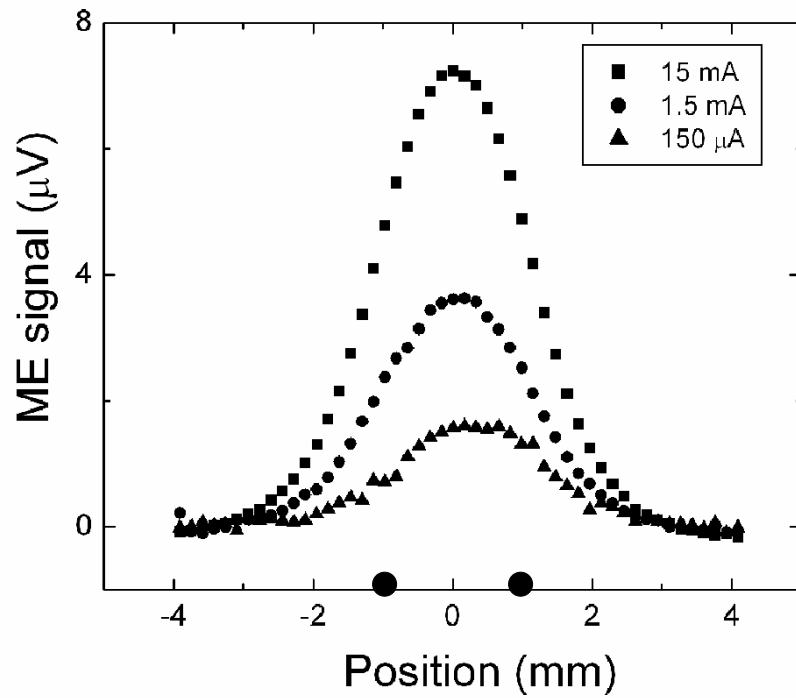


Figure 6.12: A series of scans taken at the following currents: 14.7 mA, 1.47 mA, 0.147 mA. Here the results from 0.147 mA are clearly evident, showing the maximum sensitivity to be 1.5×10^{-10} T. The black circles denote the position of the wires.

be used to make a near-field scanning magnetic field probe with a sensitivity of 10^{-10} T and a spatial resolution roughly determined by the device size. It is of interest from an applications point of view to increase the spatial resolution by orders of magnitude. We have found, however, that our present method of laminate bonding precludes us from pursuing smaller device dimensions as there is inhomogeneity in the bonding of the tri-layer. The length scale of this inhomogeneity is of the order of hundred's of micrometers and precludes reducing the device size down to less than 1 mm. Alternative methods of fabricating devices and in particular bonding techniques are currently being pursued so that we can work towards reducing the device size and hence the spatial resolution of the scanning magnetic probe.

6.4 Conclusion

A simple near-field scanning magnetic field probe has been demonstrated using magnetoelectric laminates formed from tri-layers of Metglas and PVDF. The high permeability of Metglas yields a relatively high AC field sensitivity of $467 \pm 3 \mu\text{V}/\text{Oe}$ at DC field biases of 70 Oe despite its low magnetostriction. Preliminary scans of current bearing rings indicate that the size of the device is the primary limiting factor in determining the spatial resolution of the device. Magnetic fields as low as 3×10^{-10} T have been detected from line scans over a current bearing ring, yielding a sensitivity of $\approx 5 \times 10^{-10} \text{ T}/\text{Hz}^{\frac{1}{2}}$.

Chapter 7

Conclusions and Future Work

7.1 Conclusions

Magnetostriction in the Fe-Ga system is currently at the center of a large amount of research. In order to be used in practical applications there is a need to add ternary elements to the system to increase workability. Finding a ternary, or possibly quaternary, addition that increases workability of Fe-Ga without decreasing its magnetostriction is a formidable challenge using normal bulk-sample fabrication techniques.

One central purpose of this thesis was to put forward a quantitative method for measuring magnetostriction in combinatorial composition-spread samples. Magnetostriction measurements were realized using a known optical approach that had been modified to operate in a high-throughput environment. Measurements of deflection due to magnetostriction were performed on arrays of compositionally distinct MEMs cantilevers.

Initial studies of binary Fe-Ga reveal a trend consistent with what has previously been seen in bulk studies. Two main maxima in magnetostriction are

observed to occur at $\text{Fe}_{78}\text{Ga}_{22}$ and $\text{Fe}_{68}\text{Ga}_{32}$. An additional minor maximum, that was previously unreported, has been observed at 4.5 at% Ga. This correlates with a maximum in magnetocrystalline anisotropy and a maximum in the magnetic moment per Fe atom, also reported in bulk.

Studies on the ternary addition of Pd and Al to Fe-Ga were also presented. It was found that the addition of small amounts of Pd decreased the maximal magnetostriction observed by a factor of 2. In addition the trend in magnetostriction was found to be greatly altered by the addition of small amounts of Pd. The addition of Al was found not to greatly affect the trend of magnetostriction. In fact, the addition of up to 10 at% Al to $\text{Fe}_{70}\text{Ga}_{30-x}\text{Al}_x$ preserved magnetostriction. The addition of substantial amounts of Al to Fe-Ga while maintaining large magnetostriction will increase the workability of the alloy. This will result in less brittle transducers and sensors that could be used in a dynamic environment.

In order to obtain optimal performance of magnetostrictive materials it is frequently necessary to heat treat them at high temperatures and then rapidly quench them. To this end, an ultra-high vacuum annealing/quenching furnace was created. The furnace allows for the high-vacuum annealing/quenching of composition-spread samples deposited onto 3" Si wafers. As a model system the magnetic and structural properties of Fe-Pd and Fe-Pd-Ga were probed. Quenching studies on $\text{Fe}_{70}\text{Pd}_{30}$ reveal the presence of the high temperature fcc/bcc phase as well as thermally actuated martensitic transitions. The magnetic properties of Fe-Pd-Ga along the Fe-Pd binary line, probed via scanning SQUID microscopy and magneto-optical Kerr effect, were found to correlate well with the Fe-Pd high temperature phase diagram.

Finally it has been demonstrated that a simple bonded Metglas/PVDF tri-

layer devices can be used to make a near-field scanning magnetic field probe with a sensitivity of 10^{-10} T and a spatial resolution roughly determined by the device size. It is of interest from an applications point of view to increase the spatial resolution by orders of magnitude. We have found, however, that our present method of laminate bonding precludes us from pursuing smaller device dimensions as there is inhomogeneity in the bonding of the tri-layer. The length scale of this inhomogeneity is of the order of hundreds of micrometers and precludes reducing the device size down to less than 1 mm.

7.2 Future Works

Now that an effective measurement technique for measuring magnetostriction in thin-film samples has been established, it can be applied to the search for new magnetostrictive materials in Fe-Ga ternaries as well as other materials systems. There are three major thrusts to this ongoing research:

7.2.1 Fe-Ga

The stabilization of the DO_3 phase to lower overall Ga contents with the inclusion of Pd is interesting. Although an alloy of Fe-Ga-Pd increases the cost of Fe-Ga, it likely makes it more malleable, particularly since the overall Ga content has been decreased. It is therefore of interest to search for other ternary additions that would have a stabilizing effect on the DO_3 phase, without degrading its magnetostriction.

The third maximum in magnetostriction observed for Ga contents around 4 at% seems to coincide with the boundary between α -Fe (bcc) and γ -Fe (fcc). From an applications perspective, if the value of magnetostriction could be increased, then

the low Ga content of these materials is very interesting. Several studies are currently being pursued to confirm the presence of this maximum and exploit it. Bulk samples in this composition region will be made and tested for various annealing conditions to confirm that the γ -phase can be preserved in bulk experiments via quenching. Thin-film ternary alloys including other γ phase facilitators are under way.

7.2.2 Exploration of Fe-Co and Ternary Systems

It has been known for years that binary Fe-Co exhibits large magnetostriction, and a casual glance at its compositional dependence calls to mind that of Fe-Ga. The Fe-Co phase diagram is also quite similar to that of Fe-Ga, with a mixed region of fcc and bcc around 80 at% Co. Also, alloys of Fe and Co are more interesting than Fe-Ga for applications since they are easy to machine.

Thin-film binary Fe-Co studies will be done to establish that the trend is transferable from bulk to thin-film systems. Afterwards quenching studies will be undertaken to study in detail the change in microstructure and magnetostriction with different annealing conditions.

The addition, fcc promoting ternary elements to Fe-Co offer the potential of increasing the magnetostriction observed. For initial studies, the elements of choice will be Ga and Al, to search for common causes of magnetostriction and possibly larger values of λ_{100} . Afterwards other elements will be considered.

7.2.3 Further Development of Measurement Techniques

Although significant progress has been made in developing a high-throughput characterization technique for magnetostriction in ternary composition-spreads, truly

quantitative calculations of λ_{100} require knowledge of the ratio of $E_f/(1 + \nu_f)$. Earlier in this thesis a value for this ratio of 50 GPa was chosen to facilitate the comparison of the values of magnetostriction with other thin-film and bulk studies. This approach allows the monitoring of trends and, since the value of this ratio in Fe-Ga should not be too different, it approximates the true values of magnetostriction in this system. However, to calculate true values of the magnetostriction, measurements of $E_f/(1 + \nu_f)$ must be made. To this end we are in the process of developing a technique that will measure this ratio by monitoring the shift in resonant frequency of oscillation of the cantilevers pre and post-deposition.

It is also possible to use the magnetic torque effect in the measurement of magnetostriction constructively. By carefully monitoring the angle between the magnetic field and the cantilever, and measuring the linear deflection at high fields, it is possible to directly measure the saturation magnetization of each sample while measuring magnetostriction. This technique can be combined with MOKE, by splitting the incident laser beam, and can give magnetostriction and magnetization vs. magnetic field curves simultaneously.

BIBLIOGRAPHY

- [1] L. Dai. Elasticity and magnetoelasticity of fe-ga solid solutions, May 2002.
- [2] A.E. Clark, K.B. Hathaway, M. Wun-Fogle, T.A. Lograsso, and G. Petculescu. *J. App. Phys.*, 10:10M315–1, 2005.
- [3] T. B. Massalski. *Binary Phase Diagrams*. American Society of Metals, 1987.
- [4] A.E. Clark, K.B. Hathaway, M. Wun-Fogle, J.B. Restorff, T.A. Lograsso, V.M. Keppens, G. Petculescu, and R.A. Taylo. Tampa, FL, Nov. 2003. 47th Annual Conference on Magnetism and Magnetic Materials.
- [5] P. Mungsantisuk, R. P. Corson, and S. Guruswamy. *J. Appl. Phys.*, 98(11):123907–1, 2005.
- [6] N. Srisukhumbowonchai and S. Guruswamy. *J. Appl. Phys.*, 90(11):5680, 2001.
- [7] S.J. Bending. *Advances in Physics*, 48(4):449, 1999.
- [8] Clarke and A. I. Braginski. *The SQUID handbook Vol. II*. Wiley, 1st edition, 2006.
- [9] F. C. Wellstood. *private communication*.
- [10] X.-D. Xiang, X. Sun, Y. Lou, K.-A. Wang, H. Chang, W. G. Wallace, Freedman, S.-W. Chen, and P.G. Schultz. *Sciences*, 268:1738, 1995.
- [11] H. Chang, I. Takeuchi, and X.-D. Xiang. *Applied Physics Letters*, 74:1165, 1999.
- [12] I. Takeuchi, H. Chang, C. Gao, P. G. Schultz, X.-D. Xiang, R.P. Sharma, M. J. Downes, and T. Venkatesan. *Appl. Phys. Lett.*, 73:894, 1998.
- [13] J. Wang, Y. Yoo, C. Gao, I. Takeuchi, X. Sun, H. Chang, X.-D. Xiang, and P. G. Schultz. *Science*, 279:1712, 1998.

- [14] H. Chang, C. Gao, I. Takeuchi, Y. Yoo, J. Wang, P. G. Schultz, X.-D. Xiang, R. P. Sharma, M. Downes, and T. Venkatesan. *App. Phys. Lett.*, 72:2185, 1998.
- [15] S. Sakahara, K. Yajima, R. Belosludoy, S. Takami, M. Kubo, and A. Miyamoto. *Applied Surface Science*, 189:196, 2002.
- [16] J. D. Hewes and L. A. Bendersky. *Applied Surface Science*, 189:196, 2002.
- [17] I. Takeuchi, O. O. Famodu, J. C. Read, M. A. Aronova, K.-S. Chang, C. Craciunescu, S. E. Lofland, M. Wuttig, F. C. Wellstood, L. Knauss, and A. Orozco. *Nature Materials*, 2:180, 2003.
- [18] D. A. Barkhouse, A. Bonakdarpour, M. Fleischauer, T. D. Hatchard, and J. R. Dahn. *J. Magn. and Magn. Mater.*, 261:399, 2003.
- [19] J. Cui, Y. S. Chu, O. O. Famodu, Y. Furuya, J. R. Hattrick-Simpers, R. D. James, A. Ludwig, S. Thienhaus, M. Wuttig, Z. Zhang, and I. Takeuchi. *Nature Materials*, 5:286, 2006.
- [20] J. C. Phillips. *Physics of High- T_c Superconductors*. Academic Press, New York, 1st edition, 1989.
- [21] A. J. Zambano, H. Oguchi, I. Takeuchi, Y. Choi, J. S. Jiang, J. P. Liu, S. E. Lofland, D. Josell, and L. A. Bendersky. *Phys. Rev. B*, 75:144429, 2007.
- [22] M. Murakami, K.-S. Chang, M. A. Aronova, C.-L. Lin and M. H. Yu, J. Hattrick-Simpers, M. Wuttig, I. Takeuchi, C. Gao, B. Hu, S. E. Lofland, L. A. Knauss, and L. A. Bendersky. *App. Phys. Letts.*, 87:112901, 2005.
- [23] S. Fujino, M. Murakami, V. Nagarajan, S.-H. Lim, A. Varatharajan, C. J. Fennie, M. Wuttig, S. G. Salamanca-Riba, and I. Takeuchi. *submitted to Science*.
- [24] H. Y. Hwang and S.-W. Cheong. *Science*, 28:1607, 1997.
- [25] J. Turchinskaya, L. A. Bendersky, A. J. Shapiro, K.-S. Chang, I. Takeuchi, and A. Roytburd. *J. of Materials Research*, 19:449, 2004.
- [26] B. D. Cullity. *Introduction to Magnetic Materials*. Addison-Wesley Publishing Company, 1st edition, 1972.
- [27] A. E. Clark, J. B. Restorff, M. Wun-Fogle, T. A. Lograsso, and D. L. Schlagel. *IEEE Tran. Magn.*, 36:3238, 2000.
- [28] R. C. Hall. *J. Appl. Phys.*, 30(6):816, 1958.

- [29] R. M. Bozorth. *Ferromagnetism*. D. Van Nostrand Company, Inc., 1st edition, 1951.
- [30] E. P. Wohlfarth, editor. *Ferromagnetic Materials (Magnetostrictive Rare Earth-Fe₂ Compounds)*. North Holland Publ. Co., 1980.
- [31] J. Cui, T. W. Shield, and M. Wuttig. *App. Phys. Letts.*, 85(9):1642, 2004.
- [32] A. Sozinov, A. A. Likhachev, N. Lanska, and K. Ullakko. *Appl. Phys. Lett.*, 80:1746, 2002.
- [33] E. du Tremolet de Lacheisserie. *Magnetostriction Theory and Applications of Magnetoelasticity*. CRC Press, 1st edition, 1993.
- [34] S. Rafique. Magnetic anisotropy of $fe_{1-x}ga_x$ alloys, 2003.
- [35] J. J. Hanak. *Journal of Materials Science*, 5:964–971, 1970.
- [36] J. J. Hanak and J. I. Gittleman. *AIP Conference Proceedings*, 10:961–965, 1973.
- [37] O. O. Famodu. PhD thesis, University of Maryland, 2004.
- [38] C. Craciunescu, Y. Kishi, L. Saraf, R. Ramesh, and M. Wuttig. *Proc. of MRS 2002 Symposium*, 2002.
- [39] E. du Tremolet de Lacheisserie and J. C. Peuzin. *J. of Magn. and Magn. Mater.*, 136:189, 1994.
- [40] N. H. Duc, K. Mackay, J. Betz, and D. Givord. *J. Appl. Phys.*, 87(2), 2000.
- [41] X. Yang, L. T. Wood, J. H. Miller, and M. Strikovski. *J. Appl. Phys.*, 92(2):1168, 2002.
- [42] J. Cao, A. Savan, M. Ehmman, and A. Ludwig. A thin film/cantilever-based method for the high-throughput screening of hydrogen storage materials. Boston, MA, USA, 2006. Materials Research Society.
- [43] R. Kainuma, K. Ishida, and T. Nishizawa. *Metallurgical Trans. A*, 23A:1147, 1992.
- [44] H. Kato, Y. Liang, and M. Taya. *Scripta Mat.*, 46:471, 2002.
- [45] R. H. Williams. *IEEE Trans. on Magn.*, 16(5):1059, 1980.
- [46] A. E. Clark, J. B. Restorff, M. Wun-Fogle, T. A. Lograsso, M. Huang, and E. Summers. *J. of App. Phys.*, 101:09C507, 2007.

- [47] J. R. Kirtley and J. P. Wikswo. *Annual Review Materials Science.*, 29:117, 1999.
- [48] F. C. Wellstood, Y. Gim, A. Amar, R. C. Blak, and A. Mathai. *IEEE Trans. on Applied Superconductivity*, 7:313, 1997.
- [49] M. Aronova. PhD thesis, University of Maryland, 2003.
- [50] E. Klokhholm. *IEEE Trans. Magn.*, 12:819, 1976.
- [51] E. Klokhholm and C. V. Jahnes. *J. of Magn. and Magn. Mater.*, 152:226, 1996.
- [52] E. du Tremolet de Lacheisserie and J. C. Peuzin. *J. of Magn. and Magn. Mater.*, 152:231, 1996.
- [53] E. Quandt, A. Ludwig, J. Betz, K. Mackay, and D. Givord. *J. Appl. Phys.*, 81(8):5420, 1997.
- [54] F. Schatz, M. Hirscher, M. Schnell, G. Flik, and H. Kronmuller. *J. Appl. Phys.*, 76:5380, 1994.
- [55] R. C. Hall. *J. Appl. Phys.*, 28:707, 1957.
- [56] R. C. Hall. *J. Appl. Phys.*, 31(6):1037, 1960.
- [57] Etienne du Tremolet de Lacheisserie. *Magnetostriction Theory and Applications of Magnetoelasticity*. CRC Press, 1st edition, 1993.
- [58] S. Guruswamy, N. Srisukhurnbowornchai, A. E. Clark, J. B. Restorff, and M. Wun-Fogle. *Scripta. Mat.*, 43(3):239, 2000.
- [59] A.E. Clark, K.B. Hathaway, M. Wun-Fogle, J.B. Restorff, T.A. Lograsso, V.M. Keppens, G. Petculescu, and R.A. Taylor. *J. App. Phys.*, 10:8621, 2003.
- [60] M. Wuttig, L. Dai, and J. Cullen. *Appl. Phys. Lett.*, 80:1135, 2002.
- [61] A.E. Clark, J.B. Restorff, M. Wun-Fogle, K.B. Hathaway, T.A. Lograsso, M. Huang, and E. Summers. *Submitted for publication as a MMM proceedings*.
- [62] A. G. Khachaturyan and D. Viehland. *personal communication*.
- [63] M. C. Zhang, H. L. Jiang, X. X. Gao, J. Zhu, and S. Z. Zhou. *J. Appl. Phys.*, 99:023903–1, 2006.
- [64] P. D. McGary and B. J. H. Stadler. *J. Appl. Phys.*, 97:10R503, 2005.
- [65] J. L. Weston, A. Butera, T. Lograsso, M. Shamsuzzoha, I. Zana, G. Zangari, and J. Barnard. *IEEE Trans. on Mag.*, 281(5):2832, 2002.

- [66] A. Buter, J. Gomez, J. L. Weston, and J. A. Barnard. *J. App. Phys.*, 98:033901–1, 2005.
- [67] R. A. Dunlap, N. C. Deschamps, R. E. Mar, and S. P. Farrell. *J. of Phys.: Condensed Matter*, 18, 2006.
- [68] M. Takeuchi, Y. Matsumura, and H. Uchida. *Journal of the Japan Institute of Metals*, 68(2):142, 2004.
- [69] B. Stadler. *personal communication*.
- [70] K. Wasa, M. Kitabatake, and H. Adachi. *Thin Film Materials Technology: Sputtering of Compound Materials*. Williams Andrew, 2004.
- [71] S. Rafique, J. R. Cullen, M. Wuttig, and J. Cui. *Appl. Phys. Lett.*, 95(11):6939, 2004.
- [72] J. B. Restorff, M. Wun-Fogle, A. E. Clark, T. A. Lograsso, A. R. Ross, and D. L. Schlagel. *J. Appl. Phys.*, 91(10):8225, 2002.
- [73] I. Takeuchi, C. J. Long, O. O. Famodu, M. Murakami, J. Hattrick-Simpers, G. W. Rubloff, M. Stukowski, and K. Rajan. *Rev. Sci. Inst.*, 76:06223, 2005.
- [74] J. Cui. *Martensitic Phase Transformations and Ferromagnetic Shape Memory Effects in FePd Single Crystal*. PhD thesis, University of Minnesota, 2002.
- [75] Y. Sugimura, I. Cohen-Karni, P. McCluskey, and J. J. Vlassak. *J. Mater. Res.*, 20(9):2279, 2005.
- [76] S. Inoue, T. Namazu, S. Fujita, K. Koterazawa, and K. Inoue. *Mater. Sci. Forum*, 426-432:2213, 2003.
- [77] D. Vokoun, J. C. Shih, T. S. Chin, and C. T. Hu. *Magn. Mag. Mat.*, 281, 2004.
- [78] H. Kuramochi, T. Uzumaki, M. Yasutake, A. Tanaka, and H. Akinage and-cui2004 H. Yokouama. *Nanotechnology*, 16(24), 2005.
- [79] A. Sandhu, A. Okamoto, I. Shibasaki, and A. Oral. *Microelectronic Engineering*, 73-74:524–528, 2004.
- [80] H. Zheng, J. Wang, S. E. Lofland, Z. Ma, L. Mohaddes-Ardabili, T. Zhao, L. Salamanca-Riba, S. R. Shinde, S. B. Ogale, F. Bai, D. Viehland, Y. Jia, D. G. Schlom, M. Wuttig, A. Roytburd, and R. Ramesh. *Science*, 30(303):661, 2004.
- [81] S. Stein, M. Wuttig, D. Viehland, and E. Quandt. *J. Appl. Phys.*, 97:1–1, 2005.

- [82] Z. Xing, S. Dong, J. Li, and D. Viehland. *Appl. Phys. Lett.*, 88:062510, 2006.
- [83] S. Dong, J. Zhai, J. Li, and D. Viehland. *Appl. Phys. Lett.*, 83:4812, 2003.
- [84] S. Dong, J. Zhai, J. Bai, J. Li, and D. Viehland. *Appl. Phys. Lett.*, 87:062502–1, 2005.
- [85] J. Zhai, S. Dong, Z. Xing, J. Li, and D. Viehland. *Appl. Phys. Lett.*, 89:083507–1, 2006.
- [86] D. C. Meeker. *Finite Element Method Magnetics, Version 4.0.1*. <http://femm.foster-miller.net>, Version 4.0.1 (03Dec2006 Build).
- [87] M. R. Sheinfein, J. Unguris, D. T. Pierce, and R. J. Celotta. *J. Appl. Phys.*, 67(9):5932, 1990.
- [88] T. Chang, M. Lagerquist, J.-G. Zhu, and J. H. Judy. *IEEE Trans. on Magn.*, 28(5):3138, 1992.